INTELLIGENT THERAPEUTIC ROBOT: DESIGN, DEVELOPMENT, AND CONTROL

by

Asif Al Zubayer Swapnil

A Thesis Submitted in

Partial Fulfillment of the

Requirements for the Degree of

Master of Science

in Engineering

at

The University of Wisconsin-Milwaukee

December 2020

ABSTRACT

INTELLIGENT THERAPEUTIC ROBOT: DESIGN, DEVELOPMENT, AND CONTROL

by

Asif Al Zubayer Swapnil

The University of Wisconsin-Milwaukee, 2020
Under the Supervision of Professor Mohammad Habibur Rahman

This research contributes to developing an Intelligent Therapeutic Robot (iTbot) designed to provide therapy to patients with upper limb impairment due to stroke, injury, and other trauma. This robot aims to implement robotic rehabilitation based on principles of motor rehabilitation and Neuroplasticity. The iTbot, as developed in this research, can provide end-effector type rehabilitation exercises in various configurations, including motion in the vertical and horizontal plane. It can provide passive, active, and active-assisted rehabilitation therapies to patients with limited upper limb mobility.

The iTbot has been designed with simplicity in mind with a minimum viability approach. With a minimum amount of custom fabricated parts, the design, build, control, and operation of this robot have reduced complications while providing a wide range of therapeutic exercises. iTbot's manually adjustable orientation allows it to offer rehabilitation exercises in either vertical or horizontal workspace with only two degrees of freedom.

To facilitate such a therapeutic robot's operation, which can operate in multiple physical orientations, model-based control strategies including modified Computed Torque Control (mCTC) and newly developed Sliding Mode with intelligent Reaching Law (SMiRL) have been implemented as iTbot's control method. Various experiments mimicking real-world application scenarios have been performed to compare the two controllers' operating performance with the traditional Proportional, Integral, Derivative (PID) control method.

To provide active and active-assistive rehabilitation exercises, iTbot employs a six-axis force-torque sensor as its input along with an adjustable admittance-based control strategy. This allows iTbot to either provide assistive or resistive rehabilitation exercises with the same system, enabling applying multiple principles of robot-aided rehabilitation in a single robot. Furthermore, iTbot can be used as a physical interface to video game and virtual reality-based rehabilitation exercises, enabling implicit and explicit feedback principles of motor rehabilitation.

Keywords: Robot, Rehabilitation, Upper Limb, Wrist, 2 DoFs, Forearm Pronation, Control, Assistive Therapy, Motor Rehabilitation, End-effector type Therapeutic Robot

TABLE OF CONTENTS

LIST OF FIGURES

LIST OF TABLES

ACKNOWLEDGMENTS

First, I would like to pay my gratitude to almighty ALLAH (SWT) for providing me strength, patience and courage needed to complete this thesis. After that I would like to thank my advisor, Dr. Mohammad Rahman for is support and guidance throughout this work. His advice and guidance have made an immeasurable difference in the quality of work completed in this thesis. I would also like to thank my MS committee members, Dr. Nosonovsky and Dr. Brahmi for serving in my committee and providing important guidance and feedback. After that, I would like to thank the lab members at UWM BioRobotics Lab, especially Md Assad Uz Zaman, Tanvir Ahmed, and Md Rasedul Islam for their help and support throughout the whole duration of my thesis work at the lab.

CHAPTER 1

INTRODUCTION

The upper limb is the most essential accessory available for a person to perform the activities of their daily lives. The human upper limbs' capability to perform complex motion and manipulation tasks with a high level of precision and control enables humans to perform most of the functions necessary for living. Unfortunately, many individuals live with full or partial loss or impairment of their upper limbs. Upper limb impairments can range from minor deficiencies in motor control of the arm to complete mobility loss. Various geriatric disorders, stroke, and trauma are the primary reason behind such upper limb impairments.

Stroke is one of the leading causes of upper arm impairments, where 85% of stroke survivors need to live with acute arm impairment [1]. Adding to that statistic, a study conducted by the World Health Organization [2] notes that worldwide stroke affects 15 million people every year; among them, nearly 800,000 people are affected in the United States alone. The number of stroke survivors impacted by its aftermath is projected to increase by 4 million by 2030 in the United States [3]. Apart from stroke, trauma from sports injuries, workplace accidents, and other orthopedic injuries result in the loss of function of the upper limb [4]. Statistically, hand and arm injuries make up $1/3^{rd}$ of workplace injuries [5]. These numbers paint a picture of the sheer number of people who would need to live with hand and arm injuries and impairment in their lifetime. These individuals end up having no other choice than being a burden on their families, communities, and their country.

To improve the quality of their own life and the lives of people around them, these individuals with upper arm impairments need effective recovery methods. Rehabilitation therapy focused on upper arm injuries and impairment is the primary recovery path for these individuals [6]. These rehabilitation therapies involve long repetitive exercises guided by a skilled therapist or clinician. The time commitment required by the therapists and clinicians for these exercises and the shortage of such qualified personnel makes it often impossible to provide the required therapy to individuals who need it most. And even when possible, the cost of receiving such therapy and limited availability results in individuals not receiving the full extent of rehabilitation they need for recovery.

Two modes of rehabilitation therapies are hypothesized to provide a full rehabilitation path for a person with upper arm impairment. The passive rehabilitation therapies provide intensive and repetitive exercises intended to improve motor skills [7]. These exercises help improve the patient's range of motion, promote arm mobility, and reduce muscle contractures. These help to prepare an individual in the path of recovery towards being able to perform active exercises. These types of exercises are traditionally performed with the help of the therapists who provide repeated motion to the patient's arm. Active rehabilitation therapies are exercises where the patient actively performs various tasks [8] with their therapists' feedback [9].

Research work in various branches of robotics has been focusing on providing rehabilitation exercises to individuals with various limb impairments. Quite a lot of progress have been made with wearable robots, e.g., exoskeleton robots [10] [11] [12] [13] as well as some end-effector-type robots [14] [15] [16]. Although these robots can reduce the therapists' and clinicians' burden, they are still unable to provide the full path to recovery to their users. The exoskeleton or end-

effector type robots currently being researched perform well in passive exercises, where they provide repetitive therapy exercises for a long time. Still, they fall short in active exercises to provide guided task-based exercises with feedback to the user. Additionally, these robots that perform decently are overly complicated, and cumbersome, making them exclusive of patients who might need the therapy but cannot use or operate a complicated and cumbersome piece of machinery. Additionally, their costs make them inaccessible to most of the population who needs the therapy most.

Therefore, to contribute in this area, this research aims to develop a simplistic robotic rehabilitation device with minimum viable design to provide a wide range of passive, active, and active assistive rehabilitation exercises.

1.1 Research Goals

The specific aims of this research project are:

Aim 1: To develop a simplistic and minimum viable robotic rehabilitation device.

Aim 2: To enable the developed robotic rehabilitation device to provide various passive, active, and active assistive rehabilitation exercises.

This thesis is organized in chapters as described below.

CHAPTER 2: Literature Review

This chapter gives an overview of various robot-aided rehabilitation research work currently being conducted, including previous developments of exoskeleton and end-effector based rehabilitation robots.

CHAPTER 3: Robot Aided Rehabilitation

A brief overview of the principles of Neuroplasticity, motor rehabilitations, and other ideas the concept of robot-aided rehabilitation is based on is included in this chapter. The end of this chapter briefly discusses the motivation behind the development of an end effector-based rehabilitation robot in this research.

CHAPTER 4: Design of iTbot

Initial design steps in developing the proposed iTbot based on simplicity and versatility are discussed in this chapter. The design constraints and innovations behind the robot's design are presented, along with the specifications, design details, and physical constraints.

CHAPTER 5: Kinematics and Dynamic Modeling

This chapter describes the process of developing kinematic and the dynamic models of the proposed iTbot. The modified Denavit-Hartenberg (DH) notations are used for kinematic modeling. Due to the simplistic nature of the design of the iTbot, geometric solutions for inverse kinematics were used. The dynamic modeling was done using the iterative Newton-Euler formulation.

CHAPTER 6: Control and Simulation

This chapter discusses the different control techniques (such as PID, Computed Torque Control, and newly developed Sliding Mode control with innovative Reaching Law) applied to operate the *iTbot* to follow a reference trajectory during rehabilitative exercises. This chapter includes brief descriptions of the theoretical structure of each of the control algorithms. Then it goes on to

validate the iTbot model developed in Chapter 5 using simulation results and evaluates the performance of the different control techniques for trajectory tracking. In the end, this chapter discusses the use of admittance-based trajectory control to enable active and active-assisted exercises in iTbot.

CHAPTER 7: Experiments and Results

This chapter describes the experimental setup and the procedure of the experiments carried out to evaluate the performance of the iTbot, along with its operation modes and control techniques. Graphical representation of the test results and detailed explanations are included in this chapter, along with specific comments on how each set of the test checks the performance of iTbot in light of the principles of motor robot-aided rehabilitation.

CHAPTER 8: Conclusions and Future Work

In this chapter, the conclusions summarized from the research outcomes are presented, and some possible directions for further research are discussed. The future scopes section highlights the potential of this particular research through further development.

CHAPTER 2

BACKGROUND AND LITERATURE REVIEW

Development in robot-aided rehabilitation devices and procedures, which started back in the 1990s, gained momentum in the current era. With some of the therapeutic robots already commercialized and more research projects on the track of commercialization, a new development in this field requires careful consideration of missing elements of ongoing scientific research. In this chapter, robot-aided upper limb rehabilitation research in recent years has been carefully reviewed. A significant amount of robot-aided upper limb rehabilitation devices focusses on exoskeleton type devices, or joint motion focused therapy. In this review, research from the field of exoskeleton robots is included. Still, as this research focuses on a minimum viable solution to the robot-aided rehabilitation concept, more focus is given on end-effector type rehabilitation robots.

2.1 Exoskeleton type therapeutic robots

Although exoskeleton type therapeutic robots are highly suitable for precise joint-based therapy, only the high-end configurations of these robots can cover the full range of rehabilitation exercises for the whole limb. In the case of exoskeleton robots, if endpoint rehabilitation is required or task-specific and active rehabilitation is needed, the robots need to mimic the anatomical joint-configuration of the human upper limb, needing higher degrees of freedom. Among the few exoskeleton robots, ARMin-II [17], ARMin-III [12], ETS-MARSE [11], Harmony [18] are a few prominent ongoing research that aims to provide a wide range of therapeutic exercise up to the endpoint of the upper limb.

The ARMin series (ARMin, ARMin-II, and ARMin-III) of robotic exoskeleton researched and developed at ETH Zurich by Nef et al., are one of the early research projects in robotic exoskeleton targeting full upper limb rehabilitation exercises. The original ARMin [19] incorporated a 4-DoF configuration to provide rehabilitation therapy for shoulder and elbow joints only and is therefore excluded from our evaluation as an endpoint rehabilitation device. Later revisions (ARMin-II and ARMin-III) uses 7-DoF configurations for whole arm motion and rehabilitation therapy in passive and active modes. A version of ARMin-III is now commercially marketed by Hocoma AG, Switzerland, to be used in hospitals and other clinical settings.

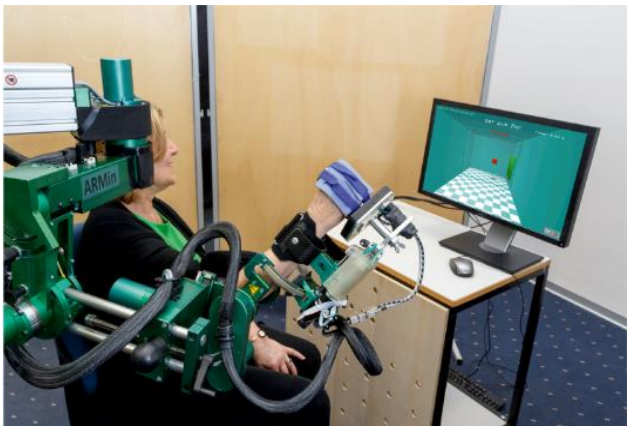

Figure 2.1 ARMin-III robot in use [12]

ETS-MARSE, a 7-DoF upper limb exoskeleton with a novel powered rotational cup for shoulder internal external rotation and forearm pronation supination, is another exoskeleton type robot that can provide endpoint therapy to the whole upper limb. It is currently being actively developed and is able to provide passive and active rehabilitation therapies.

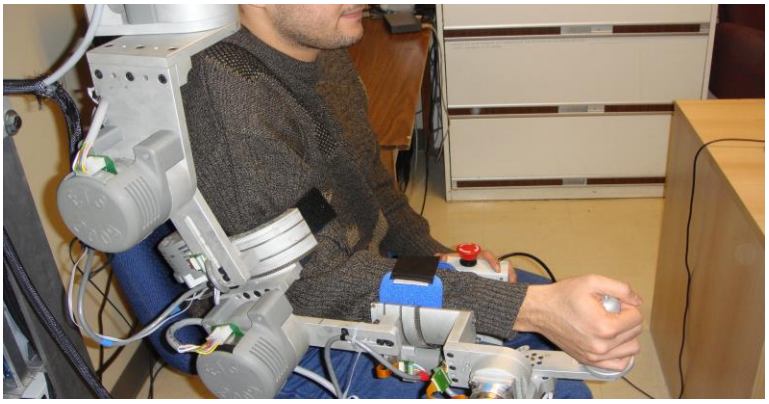

Figure 2.2 ETS MARSE robot in use [11]

Harmony, developed by Kim and Deshpande [18], is another recent

development in exoskeleton robots that can provide full arm/endpoint rehabilitation exercises. It incorporates multiple four-bar linkage mechanisms to provide joint motions, is able to conform to the human shoulder center of rotation shifts in both abduction-adduction and vertical flexion-extension movement.

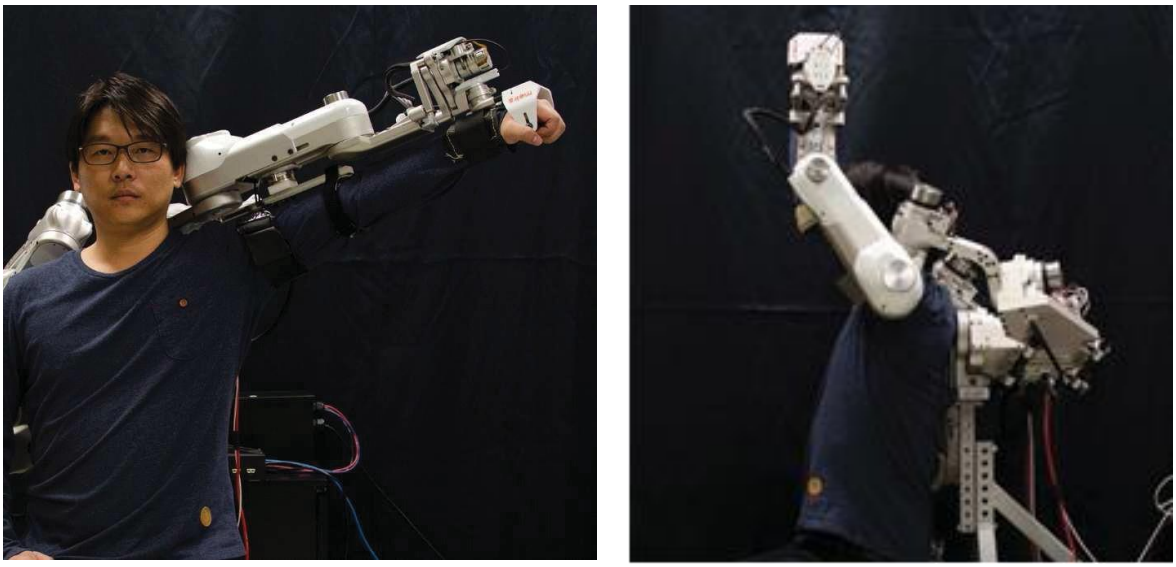

Figure 2.3 Subject wearing Harmony bimanual robot [18]

Several other exoskeleton type robots in various states of research and development are also capable of providing endpoint rehabilitation to their users. *Table 2.1* compares a selection of these existing exoskeleton type therapeutic robots that can provide therapies from the shoulder up to forearm/wrist motion of a patient. Exoskeleton robots focused only on delivering joint-based therapy to the shoulder and elbow are excluded from this list as they cannot provide endpoint therapy to the whole upper limb.

Table 2.1 Comparison of some exoskeleton type therapeutic robots

Device's Name/ Researchers	**Degrees of Freedom**	**Therapeutic Regimes**	**Modes of therapy**
ULEL [20]	3	Shoulder Elbow Wrist	Passive
Sharma & Ordonez, 2016 [21]	3	Shoulder Elbow Forearm	Passive
ExoRob [22]	4	Elbow Forearm Wrist Wrist	Passive
RUPERT [23] [24]	4	Shoulder Elbow Forearm Wrist	Active Passive
Garrido et al., 2016 [25]	4	Shoulder Elbow Forearm Wrist Wrist	Active Passive
Li et al., 2017 [26]	4	Shoulder Elbow Forearm	Passive
MAHI Exo II [27] [28]	4	Elbow Forearm Wrist Wrist Unconstrained	Active Passive
6-REXOS [29]	4	Elbow Forearm Wrist Wrist	Passive
L-EXOS [30]	5	Shoulder Elbow Forearm	Active Passive
MULOS [31]	5	Shoulder Elbow Forearm	Active Passive
MARSE-5 [32]	5	Shoulder Elbow	Active Passive

Device's Name/ Researchers	Degrees of Freedom	Therapeutic Regimes	Modes of therapy
		Forearm	
MGA [33]	5	Shoulder Elbow Forearm	Active Passive
T-WREX [34]	5	Shoulder Elbow Finger Grasp	Active Passive
RUPERT IV [35]	5	Shoulder Elbow Forearm Wrist	Active Passive
MAHI [36]	5	Elbow Forearm Wrist Wrist Unconstrained endpoint	Active Passive
Mushage et al., 2017 [37]	5	Shoulder Elbow Wrist	Active Passive
Kang and Wang, 2015 [38]	5	Shoulder Elbow Forearm Wrist	Passive
ARAMIS [39]	6	Shoulder Elbow Forearm wrist	Active Passive
ARMin-III [12] [17] [40]	6	Shoulder Elbow Forearm wrist	Active Passive
Chen et al., 2015 [41]	6	Shoulder Elbow Forearm Wrist Wrist	Passive
CABexo [42]	6	Shoulder Elbow Forearm Wrist	Passive

Device's Name/ Researchers	Degrees of Freedom	Therapeutic Regimes	Modes of therapy
		Wrist	
CADEN-7 [43]	7	Shoulder Elbow Forearm Wrist Wrist	Active Passive
MARSE-7 [10]	7	Shoulder Elbow Forearm Wrist Wrist	Active Passive
SRE [44]	7	Shoulder Elbow Forearm Wrist Wrist	Active Passive
SUEFUL-7 [45]	7	Shoulder Elbow Forearm Wrist Wrist	Active Passive
Rehab-Arm [46]	7	Shoulder Elbow Forearm Wrist Wrist	Active
CAREX-7 [47]	7	Shoulder Elbow Forearm Wrist Wrist	Passive, Active
Kim and Kim, 2017 [48]	7	Shoulder Elbow Forearm Wrist Wrist	Passive, Active

The above list of exoskeleton type therapeutic robots highlights the fact that; to provide endpoint-based therapy to the upper limb with an exoskeleton robot at least 5 degrees of freedom (4 degrees

of freedom with fixed shoulder setup) is required. Therefore, we can conclude exoskeleton robots not suitable for a minimum viable approach.

2.2 End-effector type therapeutic robots

End-effector-type therapeutic robots take a different approach to provide endpoint exercises to the human upper limb. These robots typically hold on to or attached either to the user's hand or forearm. Hence, instead of controlling the human limb's individual joint motion (such as either shoulder or elbow joint), an end-effector type robot can provide simultaneous movement to the upper limb's multiple joints. During a therapeutic session with an end-effector type robot, the user's hand follows the robot's end-effector position, while the user can orient their anatomical arm joints as suitable. Even though end-effector type robots are not ideal for individual joint therapy, these types of robots can provide less complicated, i.e., minimum viable solution to many kinds of motor rehabilitation therapies.

Figure 2.4 InMotion WRIST [14]

One of the early end-effector type rehabilitation devices developed was MIT-MANUS [49] which later evolved into InMotion Arm™ focused on providing rehabilitation exercises for shoulder and

elbow. It was later developed into InMotion Wrist [14], capable of providing rehabilitation exercises for hand and wrist.

Another approach for such an end-effector-type rehabilitation robot is using commercially available or industrial robotic manipulator to manipulate users' hands/forearm to provide rehabilitation therapy. One such example is the MAAT (Multimodal interfaces to improve therApeutic outcomes in robot-Assisted rehabiliTation) [50] where a 7-DoF Kuka LWR III robotic arm was used.

Figure 2.5 BFIAMT [51]

Finally, a simplistic approach focused on endpoint rehabilitation uses a planer robot where one or two end-effectors traverse on a planer surface with two active degrees of freedom. Two such examples are BFIAMT developed by Chang et al. [51] and H-man [52] [53] [54]. While capable

of providing effective endpoint-based therapy to the whole upper limb, these devices are usually constrained to the horizontal plane of motion.

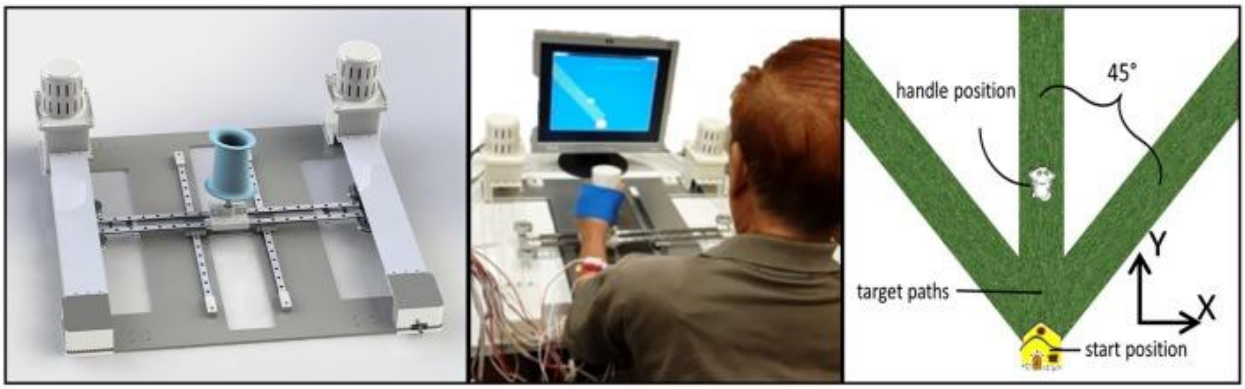

Figure 2.6 H-man [52] [53] [54]

Table 2.2 lists some existing research on these end-effector type therapeutic robots and provides some comparison parameters.

Table 2.2 Comparison of some end-effector type therapeutic robots

Device's Name/ Researchers	**Degrees of Freedom**	**Therapeutic Regimes**	**Modes of therapy**
Bi-Manu-Track [16]	1	Forearm Wrist	Passive, Active and resist
Colombo et al., 2007 [55]	1	Wrist	Active
Hu et al., 2009 [56]	1	Wrist F/E	Active
Freeman et al., 2009 [57]	2	Planar movement of the forearm	Active
BFIAMT [51]	2	Axial movement of forearm	Active Passive
H-man [52] [53] [54]	2	Planar movement of forearm	Active Passive

Device's Name/ Researchers	Degrees of Freedom	Therapeutic Regimes	Modes of therapy
ARM Guide [58]	3	Axial, elevation, and yaw of the forearm	Active Passive resist
NeReBot [59] [60]	3	Spatial movement of shoulder and elbow	Active Passive
InMotion WRIST [14]	3	Forearm Wrist Wrist	Active Passive resist
Takaiwa and Noritsugu, 2009 [61] [62]	3	Forearm Wrist Wrist	Active
MIME [15] [63] [64]	6	Shoulder Elbow Unconstrained endpoint	Active Passive resist
Gentle/S [65] [66]	6	Shoulder Elbow Forearm Unconstrained endpoint	Active Passive Resist
MAAT [50]	7	Shoulder Elbow Forearm Unconstrained endpoint	Active Passive
Umemura et al., 2009 [67]	7	Shoulder Elbow Forearm Wrist Wrist	Active
REHAROB [68]	12	Shoulder Elbow Unconstrained endpoint	Active

From the above lists, it is evident that research focus on the end-effector type therapeutic robots has been lagging behind the exoskeleton type robots. However, the research done by Freeman et al., 2009 [57], BFIAMT [51], and H-man [52], and InMotion WRIST [69] are of particular interest. These robots use only two degrees of freedom to provide planar movement of the forearm of the user. However, even with a limited number of degrees of freedom, they are not optimized for

minimum viable design. Additionally, they are usually fixed in a specific orientation and unable to provide more options for various exercises, e.g., horizontal or vertical motion and ambidextrous use.

Therefore, in this research, we are proposing a new 2 DoFs robot focused on operating at multiple manually selectable orientations to implement a broader range of robot-aided rehabilitation therapies in a minimum viable design.

CHAPTER 3

ROBOT AIDED REHABILITATION

This chapter discussed different types of rehabilitation. After that, it briefly discusses the principles of Neuroplasticity, principles of neurorehabilitation, and principles of motor rehabilitation. This chapter ends with remarks on robot-aided rehabilitation and how this research incorporated motor rehabilitation using passive, active, and active-assisted robot-rehabilitation.

3.1 Rehabilitation

The term 'rehabilitation' is defined by the World Health Organization [70] as *"a set of interventions designed to optimize functioning and reduce disability in individuals with health conditions in interaction with their environment."*

3.2 Different types of rehabilitation

The two major different types of rehabilitation we can consider are Sensory Rehabilitation and Motor Rehabilitation. When rehabilitation focuses on restoring our five traditional senses' functions, it is called Sensory Rehabilitation. These senses being touch, sight, hearing, smell, and taste. This type of rehabilitation relies on methods to augment the senses or sensory substitution systems.

On the other hand, motor rehabilitation aims to overcome the limitations of an individual's mobility to improve the quality of life. The aim of motor rehabilitation is to re-establish or improve a patient's functional health and everyday skills. These improvements can include regaining previously learned movements and lost skills due to pathology, sensory, motor, or cognitive impairment.

3.3 Neuroplasticity

The brain's ability to modify, change, and adapt both function and structure throughout life and in response to experience is referred to as Neuroplasticity [71]. It is a generic term that can describe various processes that can cause the brain to learn and adapt over time. Two general types of Neuroplasticity are; functional plasticity, where the brain can move functions from a damaged area of the brain to another undamaged area, and structural plasticity, where the brain changes its physical structure as a result of learning.

Kleim and Jones outline ten principles to describe Neuroplasticity. These principles, as adapted from the source material [72], are mentioned below.

a. ***Use it or lose it****: Failure to drive specific brain functions can lead to loss of abilities.*
b. ***Use it and improve it****: Training that drives a specific brain function can lead to improving abilities.*
c. ***Specificity****: The nature of the training experience dictates the nature of the change in the brain (plasticity).*
d. ***Repetition matters****: Change (plasticity) requires sufficient repetition.*
e. ***Intensity matters****: Change (plasticity) requires intensive training.*
f. ***Time matters****: Different forms of change (plasticity) in the brain happen at different times during training/recovery.*
g. ***Salience matters****: The training experience must be meaningful to the person to cause change (plasticity).*
h. ***Age matters****: Training-induced change (plasticity) occurs more readily in younger brains.*

i. ***Transference****: Change in function as a result of one training experience can even lead to learning other similar skills.*

j. ***Interference****: Brain changes (plasticity) that result in bad habits can interfere with learning good habits.*

3.4 Principles of motor rehabilitation

Based on multiple articles published on post-stroke rehabilitation, Maier et al. [73] identified 15 principles of neurorehabilitation based on motor learning and neuroplasticity mechanisms.

a. Massed practice/repetitive practice.

In simple terms, the principle of massed practice or repeated practice focuses on training a skill continuously with little or no rest periods in between [74]. The use of an impaired limb in a constant fashion in repeated practice can speed up performance and recovery [75] and can lead to faster acquisition of lost motor function [76].

b. Spaced practice

The spaced practice principle includes that the training sessions and repetitions should be designed with sufficient rest periods between them. Research has suggested that having such a rest period results in better end result of the therapy [77] and better retention of the learning [78].

c. Dosage/duration

In the principles of motor rehabilitation, Dosage can be simply considered as the number of hours spent in therapy [79]. It can also be considered as the frequency of the training session combined with the duration of the session. A higher level of dosage or therapy hours can result in a higher speed of recovery [80].

d. Task-specific practice

This principle postulates that the training or practice conditions result in development of the skills focused on those particular conditions [81]. For example, if training exercises are designed to simulate a person's daily activities like eating or opening doors, it will result in better performance of that person during those specific tasks in real life. Thus, focusing on performing activities of daily living (ADLs) during therapy will result in meaningful improvement of ADLs performed by patients independently.

e. Goal-oriented practice

'Goal-oriented practice' does not primarily emphasize individual muscles or movement patterns; instead, it focuses on specific motion goals and lets patients explore combinations suitable for performing a particular task. This type of practice results in better motor learning performance compared to practicing without specific goals [82].

f. Variable practice

In the principles of motor rehabilitation, the variable practice can be considered either as a method of providing variability with a single training exercise or presenting the patient with different random individual training exercises. This type of practice can be beneficial for better retention of the training [83]. However, this can hamper the initial results of the training [84] and be detrimental to motor learning [85].

g. Increasing difficulty

Increasing the difficulty in training exercises for motor rehabilitation results in more errors and demands better error processing by the patient. If the difficulty can be balanced with the patient's performance, it can result in a better outcome of the exercise [86].

h. Multisensory stimulation

The human brain always processes and combines sensory stimulation for multiple sources [87]. Combining multiple sensory inputs to provide feedback for the exercises, e.g., combining visual mediums to show the patient's performance, along with tactile and touch feedback, can result in increased performance during the therapy session and better outcomes.

i. Rhythmic cueing

During exercises, any kind of rhythmic cueing through auditory, visual, tactile, or vestibular sensory feedback can be used to create a rhythmic pattern synchronized to the exercise movements. Such rhythmic patterns can create a template based on which the patient can anticipate future moves [88], resulting in better motor activity during the exercise.

j. Explicit feedback/knowledge of results

The principle of explicit feedback or knowledge of results incorporates visual, augmented, or verbal feedback about the performance and achievement of the goal to the patient during the exercise. This type of goal-focused feedback focuses on quantitative task outcomes, for example, if the task is failed or successful, or how accurate the patient was to perform the task [81]. Explicit feedback contributes to learning by the patient through cognitive processing instead of conditioning [89].

k. Implicit feedback/knowledge of performance

The implicit feedback principle of motor rehabilitation includes providing feedback to the patient during exercise based on their performance but without referring to any specific

goal or outcome. These can be based on non-verbal feedback, demonstration, audio-visual cues, and can be provided online during the exercise. This feedback helps the patient process and correct their sensorimotor prediction errors [90], which can result in implicit learning [90].

l. Modulate effector selection

In the early stages of stroke or trauma, a patient can minimize the usage of the affected limb, resulting in loss of neural function of the affected limb [91] [92]. It is possible to constrain the unaffected limb during therapy to force more usage of the affected limb to promote the affected limb's neural recovery.

m. Action observation/embodied practice

Action observation, where patients observe a task done by somebody else before performing it themselves [93], or mirror therapy where the movements in the paretic limb are stimulated by the other limb [94] can increase the patient’s performance during rehabilitation.

n. Motor imagery/mental practice

Mental practice or motor imagery principle is the concept of patients imagining the motion actions without actually performing them. This is particularly suitable for patients with severe impairment of limbs, making them unable to perform rigorous repetitive exercises at the current stage. Using motor imagery can act as a rehearsal of the mind for future movement and can be beneficial for motor learning and rehabilitation [95].

o. Social interaction

In motor rehabilitation, social interaction is the concept of a patient's performance improvement based on the feedback from their social interaction with others. If one's social dependency or acceptance is influenced by their motor skill performance for ADL specific tasks, it can positively influence their learning performance during exercises based on feedback from others [96].

3.5 Robot-aided rehabilitation

Considering the above-discussed principles of rehabilitation, we can now consider robotics in rehabilitation therapy instead of a solely assistive device. A robotic therapy device like an end-effector robot can be used for upper limb rehabilitation where it can provide the patient with various modes of passive, active, active-assisted, and virtual rehabilitation therapies. A robotic rehabilitation device can provide repetitive rehabilitation practices without tiring or time limitations, increasing the patient's dosage. It can also have multiple programming to provide variable and spaced practice. An active rehabilitation robot can facilitate task-specific practice options with increasing difficulty and goal-oriented practice. Virtual elements like rehabilitation exercise games paired with a rehabilitation robot can provide explicit and implicit feedback to the patient with multisensory stimulation. Exercise, where the patient can record and replay their motion, can provide explicit/implicit feedback and certain levels of action observation and embodied practice. And using a robotic device instead of help by another person for performing rehabilitation exercises can increase the patient's independence, resulting in better social interaction and a sense of autonomy.

Therefore, in this research, an end-effector-type rehabilitation robot is developed to provide passive, active, and active-assisted rehabilitation exercises to patients, with the functionality to record and replay motions and capabilities of connecting to rehabilitation games in a virtual environment.

CHAPTER 4

DESIGN OF iTbot

This chapter explained the overall development process and design detail of the developed **i**ntelligent **T**herapeutic Ro**bot (iTbot),** an end-effector type robot aimed towards robot-aided rehabilitation exercise with a minimum viable design. In the beginning, a set of design goals were established with a focus on the principles of motor rehabilitation. Additionally, some goal modifications have been incorporated for the research prototype to add some robustness necessary in the research stage. Next, the design specifications were finalized, and a CAD model was prepared. After that, the robot was fabricated with a mixture of traditional machining combined with rapid manufacturing processes. Finally, the robot was integrated with the existing mechatronic system available at the UWM BioRobotics Lab with necessary modifications in the programming to enable active and active-assisted exercise features.

4.1 Design goals

To make the iTbot a minimum viable solution for a useful robot-aided rehabilitation therapy device, a set of design constraints was set, including limiting the robot to only 2 degrees of freedom (DoF). Doing so makes the robot's mathematical modeling simple, allowing more focus on fine-tuning the control methods aimed for rehabilitation exercises. The design objectives selected are listed below:

a. 2 degrees of freedom motion
b. The workspace should be able to cover human upper limb length in at least one axis

c. Should allow ambidextrous operation, left-handed and right-handed exercises in the same configuration.
d. Allow change of orientation to cover more planes of operation with only two degrees of freedom, i.e., enabling vertical or horizontal mode of operation.

Additionally, some modifiers to the above goals were added for the research prototype. These modifications are added to ensure a rigid and robust test platform while control algorithms and operation mode research is performed. The modifiers are:

a. Thicker and wider links fabricated with aluminum alloy to ensure low deflection and high rigidity.
b. Higher torque capacity motor and gear reducers to reduce physical joint torque limitations
c. Higher factor of safety in fasteners and mounting mechanism.

The above modifications ensure the system is robust enough that any significant positional error, deflection, or elasticity observed during the experiment is caused by the control algorithm, not the physical device. Reducing the disturbance generated in the mechanical system and allowing more focus on the controller and human upper limb interaction.

4.2 Design specifications and component selection

Based on the above design goals, the following components and component specifications were finalized.

a. Materials: A combination of Aluminum 6061 alloy is used for structural components, and 3D printable rapid prototyping plastic is used for covering and mounting parts.

b. **Actuators:** Brushless motors from the Maxon group were combined with harmonic drive gear reducer units were used as joint actuators. For Joint-1 Maxon EC45 Series 70-watt motor was selected, and for Joint-2, Maxon EC45 Series 30-watt version was selected. Detailed datasheets of these two motors are provided in APPENDIX – B of this document. Harmonic Drive CSF-series compact gear units with 100:1 reduction ratio, "CSF-17-100-2UH" was selected for both joints. CSF-series harmonic drive gear reducer units combine the reducer with an output "cross roller" bearing, allowing the gear reducer unit to be used as a complete robot joint directly. Appendix-E shows the technical specification and bearing loading details of the CSF-17-100-2UH gear unit.

c. **Force & Torque Sensor:** To enable force input from the user during active and active-assisted exercise, a six-axes force and torque sensor is used in the end effector of iTbot. RFT series 6-axis force-torque sensor RFT60-HA01 from Robotous Inc. was selected for this purpose. This 6-axes force sensor has ±150N force input range in F_x and F_y direction, ±200N force input range in F_z direction, along with ±4 Nm Torque input range in T_x, T_y, & T_z direction. As in the 2 DoF design, only the X-Y position of the end-effector can be controlled, not the Orientation. And as the robot's end-effector cannot have any motion in the Z direction, only F_x and F_y inputs of the Force sensor was used. Other inputs from the force-torque sensor were ignored. A handle with a soft outer grip and inner bearings for free rotation in the Z direction was designed, and 3D printed.

d. **Electronic control system and motor driver:** To enable the application of multiple control algorithms and various types of data collection required in the research stage, an analog servo driver-based robot control unit operated by a National Instruments

CompactRIO system was chosen. The system is a modified version of the existing robot control and drive system used for other exoskeleton type robots being researched at the BioRobotics Lab, University of Wisconsin Milwaukee [97].

Design specifications of components of the developed iTbot are summarized in *Table 4.1*

Table 4.1 Design specifications and selected components for iTbot at a glance

Fabrication		
Material	Aluminum 6061 alloy with Plastic (Polylactic-acid & Polycarbonate)	
Fabrication process	CNC machining and FDM 3D printing	
Actuators		
Location	Joint-1	Joint-2
Motors	Maxon EC45 70 watt	Maxon EC45 30 watt
Operating voltage (V)	24v	24v
Motor Nominal Speed (rpm)	4860	2940
Nominal Current (A)	3.21	1.01
Torque Constant (mNm/A)	36.9	51
Nominal Motor Torque (mNm)	128	55.3
Weight (g)	147	75
Motor drivers	ZB12A8 Analog Servo Drive	ZB12A8 Analog Servo Drive
Motor driver current rating (A)	12 (peak) 6 (continuous)	12 (peak) 6 (continuous)
Motor driver input	Analog (voltage)	Analog (voltage)
Motor driver feedback	Current sense, Hall sensor pulses	Current sense, Hall sensor pulses
Gear reducer	Harmonic Drive CSF-17-100-2UH	Harmonic Drive CSF-17-100-2UH
Ratio	100:1	100:1
Gear reducer average output torque limit (Nm)	39	39
Estimated max output speed (degrees per second)	290	176
Estimated joint output torque (Nm)	12.8	5.53
Control System		
Controller	NI CompactRIO 9047	
Control architecture	Ni RT Linux Real-Time CPU execution + FPGA	
CPU	Intel Atom 1.6 GHz Quad-Core	
Memory	4GB	
FPGA	Kintex-7 70T FPGA	
Input/Output	5v TTL Digital Logic I/O, ±10v Analog In/Out	
Communication	Ethernet, EtherCAT, CANopen, RS485, RS232	

Sensors	
Location	End effector
Force Sensor	RFT60-HA01
Sensor type	6-axes force/torque
Measuring capacity	Fx, Fy = 150 N, Fz = 200 N, Tx,Ty,Tz = 4 Nm
Measuring resolution	Fx, Fy = 0.1 N, Fz = 0.15N, Tx,Ty,Tz = 0.005 Nm
Communication	EtherCAT
Data refresh rate (Hz)	1000

4.3 CAD Model and Mechanical Design

To make the iTbot a minimum viable solution for useful robot-aided rehabilitation therapy device, a set of CAD models for all the components were prepared in SOLIDWORKS software. Some rendered images from the CAD model is shown in *Figure 4.1*. This CAD model was used to analyze mass and inertia properties and assembly features, clearances, and required dimensions for each joint and link. The CAD model's output was directly used to generate CNC toolpaths and 3D printing codes for fabrication.

Figure 4.1 CAD model of iTbot

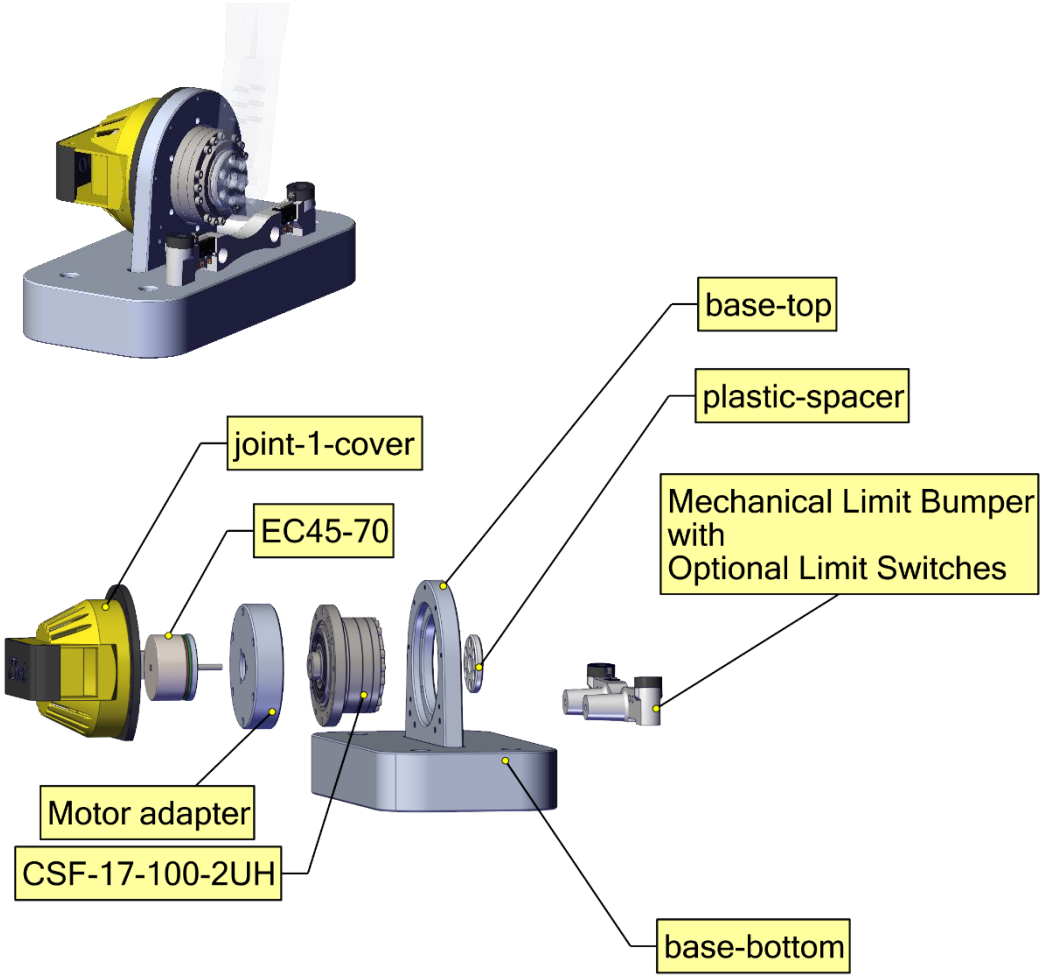

Figure 4.2 Base assembly (Top Left), Exploded view of Joint-1 (Bottom)

The design in the CAD model can be separated into three Assemblies, one for each link and the base. Each assembly is discussed in brief below.

4.3.1 Base

The base of the robot contains two fabricated aluminum parts, one being the bottom base of the robot, another is mounting for Joint-1 hardware. *Figure 4.2* shows the base assembly with an exploded view of the Joint-1. The base part is designed as a heavy block of aluminum to provide stability during the operation of the robot during experiments, and during storage. It also holds a

plastic bumper with rubber stoppers to stop the robot when it reaches the end of its range of motion. The Joint-1 consists of the harmonic drive gear reducer mounted directly to the top base part, with the motor mounted on its back with a custom-designed motor adapter. There is a plastic cover that encloses the harmonic drive gear reducer's motor side and protects the motor's rotating drum and electrical connections.

The Link-1 is attached to the harmonic drive gear reducer unit's output directly, with a plastic spacer in between. The plastic spacer acts as a buffer to absorb impact energy in case of malfunction of the robot during the development and programming of the robot in the research stage.

4.3.2 Link-1

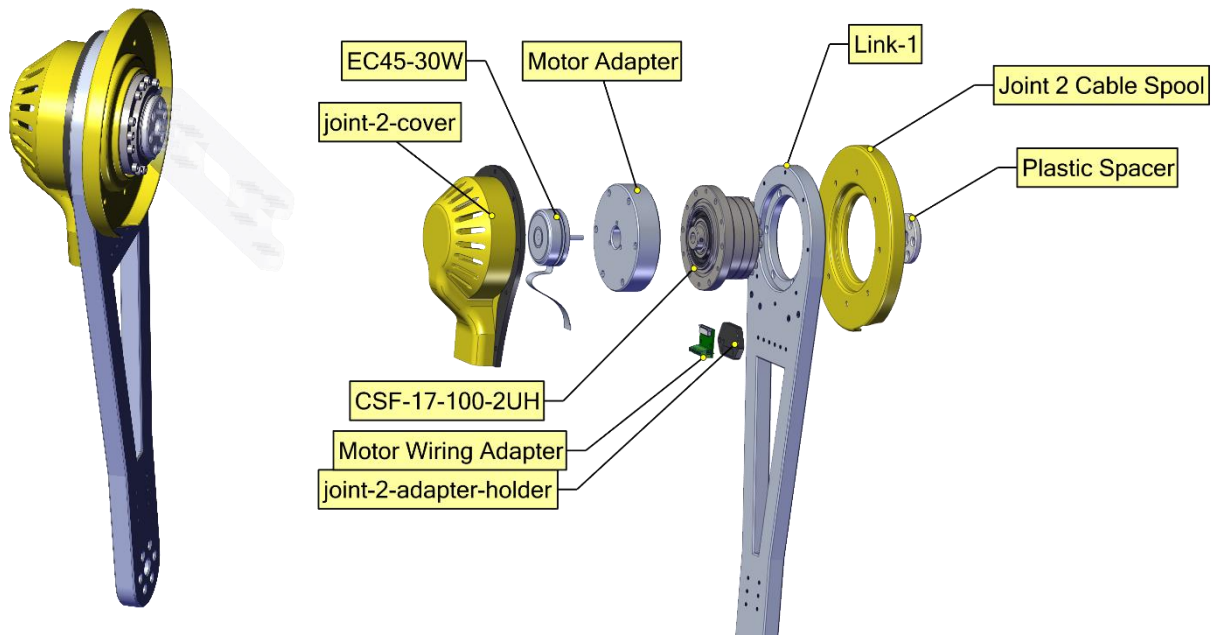

Figure 4.3 Link-1 assembly (Left), Exploded view of Joint-2 (Right)

Figure 4.3 shows the Link-1 assembly with an exploded view of the Joint-2. Once again, this assembly contains a fabricated aluminum part with a harmonic drive gear reducer directly mounted to the piece. The motor is mounted to the harmonic drive with a motor adapter plate similar to the Joint-1. Another plastic part is acting as one half of a cable spool on the other side of the Link-1, holding the slack of wire for the force sensor located at the end effector. Similar to Joint-1, Link-2 is attached to the harmonic drive gear reducer's output through a plastic spacer.

4.3.3 Link-2

Link-2 assembly is shown in *Figure 4.4*. In this assembly, the fabricated aluminum part contains the second half of the Joint-2 wire spool holder. The end of the link contains the end-effector, consisting of the force sensor and the handle. The force sensor is mounted to the aluminum link with a custom-designed mounting bracket 3D printed with high strength polycarbonate plastic. The force sensor's base side is screwed into the plastic bracket, which is then slid in a slot in the aluminum link and then fastened with few screws. The input side of the force sensor is attached to the handle.

The handle is custom designed to match the dimensions of the user's hand profile, in the case of our prototype, the average size of the two adult male lab members who participated in the development iTbot. The handle has a base part that mounts on top of the force sensor, 3D printed in polycarbonate plastic. There is an inner tube with mounting features for two bearings on both ends—this tube screws into the base part. Two ceramic ball bearings with nylon races are inserted on both ends between the inner ring and another outer ring with features for the bearings on both ends. The outer ring is made of 3D printed Polylactic-acid plastic for a comfortable grip. A bracket

is used on top of everything, which screws into the inner ring and holds the whole assembly of bearings and outer tubes in place.

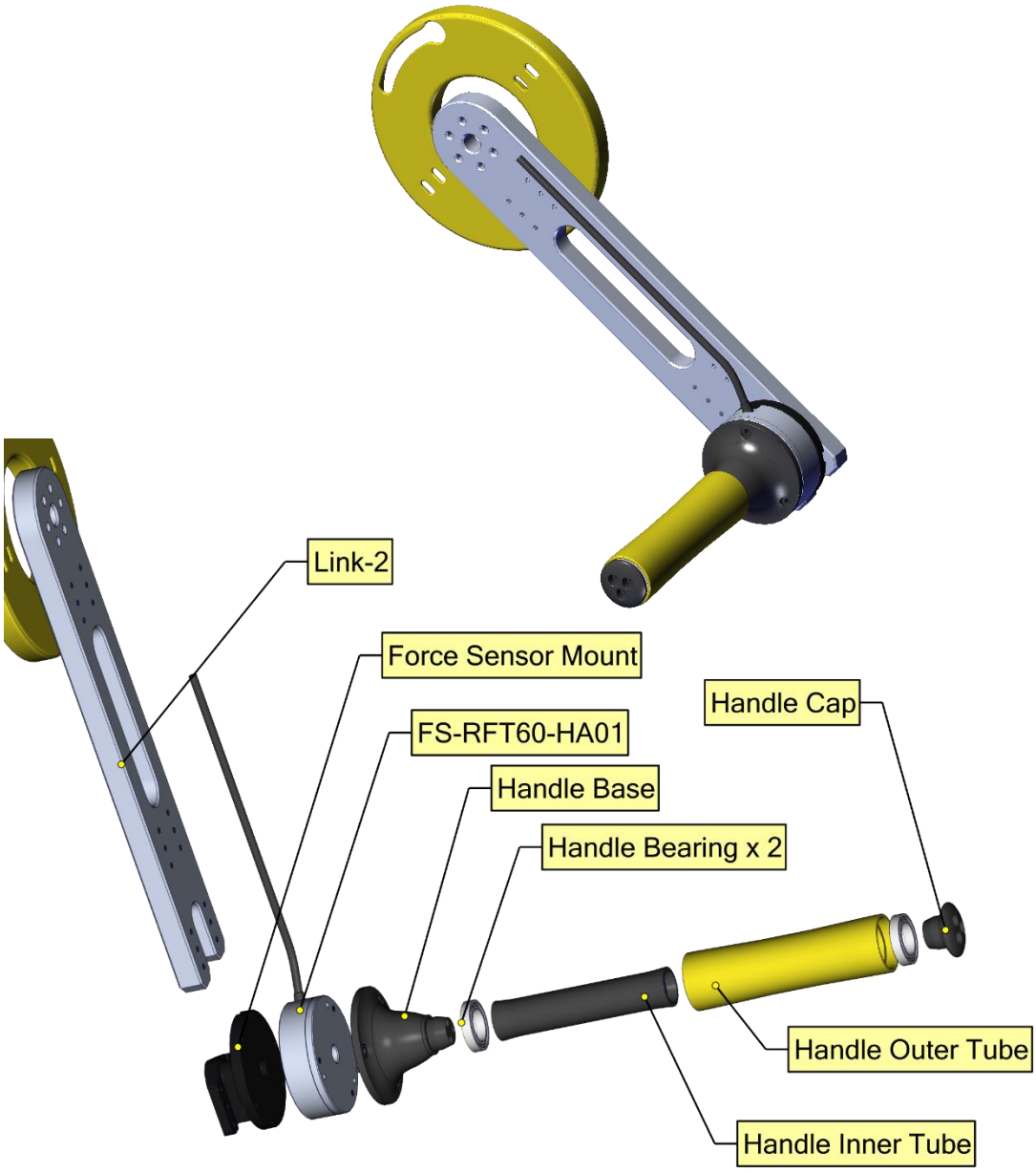

Figure 4.4 Link 2 assembly (Top), Exploded view of End-effector (Bottom)

4.4 Mechanical Parameters

The completed cad model described in Section 4.3 is used to estimate the mechanical parameters of each link and joint of the iTbot. The parameters estimated from the robot are given in the table below. The detail of the mass and inertia properties extracted from SOLIDWORKS can be found in APPENDIX – A.

Table 4.2 Mechanical parameters of iTbot estimated from CAD model

Joint Parameters		
Item	Joint-1	Joint-2
Joint Range of Motion (Degrees)	±85°	±180°
Link Parameters		
Mass (Kg)	1.79	0.65
Location of the center of gravity in link frame (m)	X = 0.26, Y = 0.00, Z = 0.00	X = 0.15, Y = 0.00, Z = 0.02
Robot Properties		
Mass (Kg)	6.67 (3.2 without base)	
Maximum Horizontal reach (m)	±0.55	
Maximum Vertical reach (m)	+0.1 to +0.55	

These parameters confirm that the iTbot can provide a 1.1 m range of motion in the X-axis of its configuration, which fulfills the design goal of covering human upper limb length [98] in one workspace direction. Also, the robot's symmetric design with a symmetric joint range of motion makes it capable of ambidextrous use. And the base design allows positioning of the robot in either horizontal or vertical orientation with proper anchoring availability.

4.5 Electrical and Electronic Design of iTbot

The electrical and electronic configuration for the iTbot system is depicted in *Figure 4.5*. It consists of a Host PC, a NI CompactRIO 9047 controller with a Kinetix-7 70T FPGA, a mainboard, multiple motor driver cards, actuators, and the Robotous RFT60-HA01 force sensor.

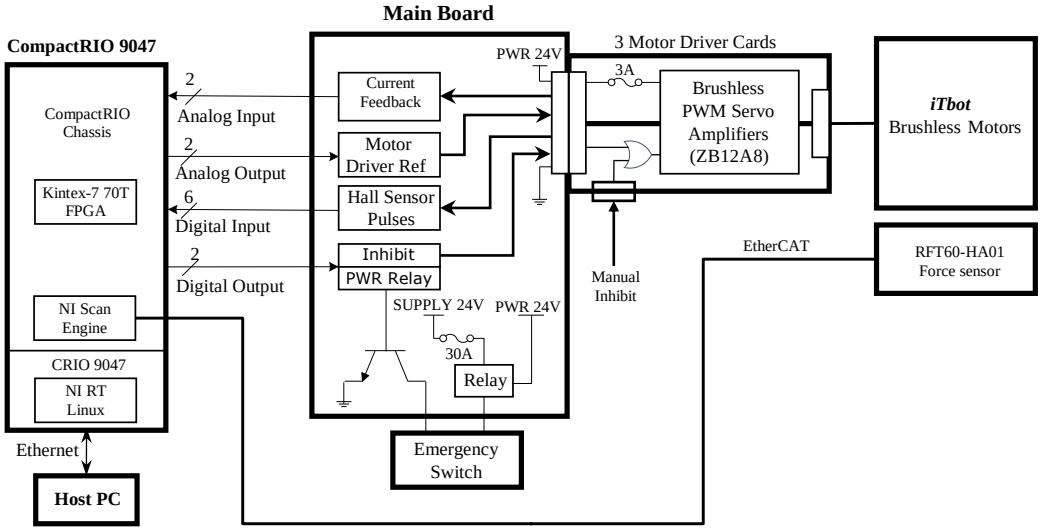

Figure 4.5 Electrical and electronic configuration for iTbot

In practice, this system is capable of running the necessary processing for the kinematic & dynamic models along with additional programming to generate, process, and record trajectory, process user input, and run closed-loop control with a bandwidth up to 2kHz.

Finally, the host pc contains the user interface required to operate the robot and the video game interface developed in Unity game engine.

CHAPTER 5

KINEMATICS AND DYNAMIC MODELING

This chapter presents the kinematic, inverse kinematic, and dynamic modeling done for design-optimization, simulation, and development of iTbot. For kinematic analysis, modified Denavit-Hartenberg (DH) parameters were used. Geometric method for inverse kinematic model and Iterative Newton-Euler methods dynamic model is used. At first, the DH notation for the iTbot has been introduced. Then kinematic modeling has been explained. Then geometric approaches to solving inverse kinematics of the robot have been discussed, and the dynamic modeling of the proposed iTRob is presented.

5.1 Kinematics

The position and orientation of the robot end-effector relative to the joint angles are obtained from the forward kinematics of the robot. For the forward kinematics analysis of the iTbot, modified Denavit-Hartenberg (DH) [99] parameters are used. To describe the location of each robot link relative to its neighbors, a coordinate frame (link frame) is attached to each link of the robot. The procedure of link frame attachment and the definition of modified DH notations are briefly described in the following subsection.

5.1.1 Co-ordinate Frame Assignment Procedure

There are various ways to assign coordinate frames to each link of a serial manipulator. For the Kinematic modeling of iTbot, the modified Denavit-Hartenberg method is used [100]. The notations steps as adapted from [99] are as follows:

- Assume each joint is 1DoF revolute joint;

- Identify and locate the axes of rotation;
- Label the joint axes $Z_0, \ldots \ldots, Z_n$;

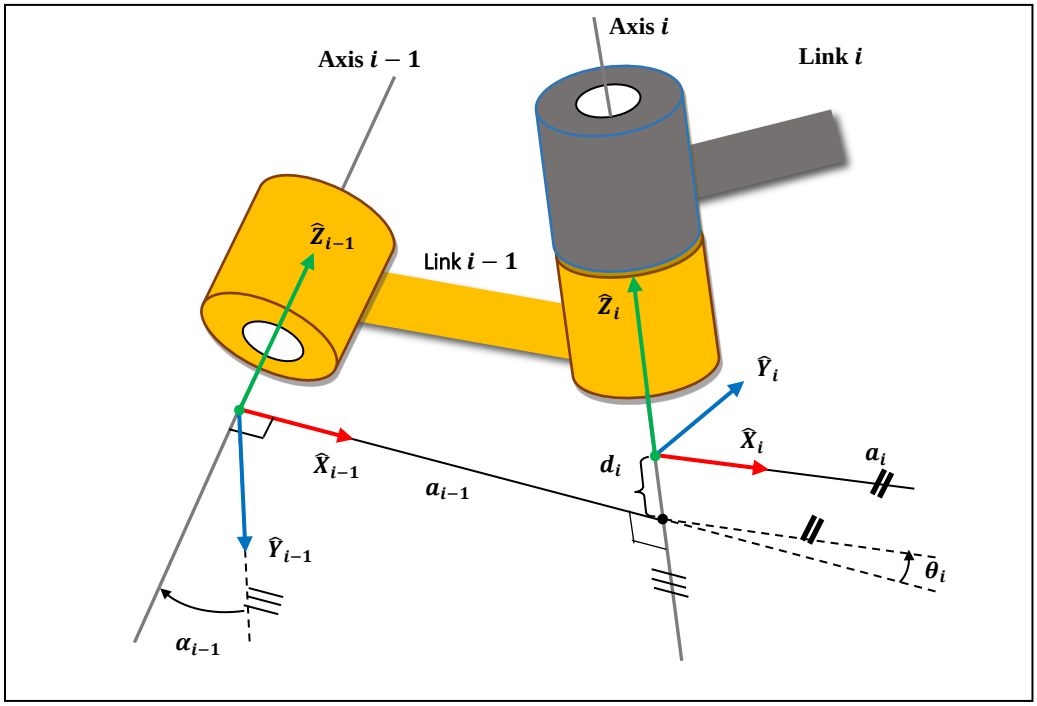

Figure 5.1 Coordinate frame assignment, Adapted from Craig (2005) [100]

- Locate the origin of each link-frame (O_i) where the common perpendicular line between the successive joint axes (i.e., Z_{i-1} and Z_i) intersects. If the joint axes are not parallel, locate the link-frame origin at the point of intersection between the axes;
- Locate the X_i axis (at link frame origin O_i) as pointing along the common normal line between the axes Z_{i-1} and Z_i. If the joint axes intersect, establish X_i in a direction *normal* to the plane containing both axes (Z_{i-1} and Z_i);
- Establish the Y_i axis through the origin O_i to complete a right-hand coordinate system.

5.1.2 Definition of D-H Parameters

A serial link manipulator type robot can be defined using four parameters (two parameters for describing the link itself and the other two for describing the link's relation to a neighboring link). These parameters are known as Denavit-Hartenberg (DH) parameters. If the coordinate frames are assigned as mentioned in the previous section [99], the definitions of the DH parameters becomes as follows [101]:

- Link Length (a_i): the length measured along X_i, from axis Z_i to axis $Z_{i+1;}$
- Link Twist (α_i): the angle measured about X_i, from axis Z_i to axis $Z_{i+1;}$
- Link Offset (d_i): the distance measured along the axis $Z_{i;}$ from X_{i-1} *to* X_i, and
- Joint Angle (θ_i): the angle measured about Z_i, from X_{i-1} *to* $X_{i.}$

In order to do the kinematic and dynamic analysis of this serial link end-effector type robot using these modified Denavit-Hartenberg (DH) parameters, the following link frames assignment for iTbot is prepared (*Figure 5.2*).

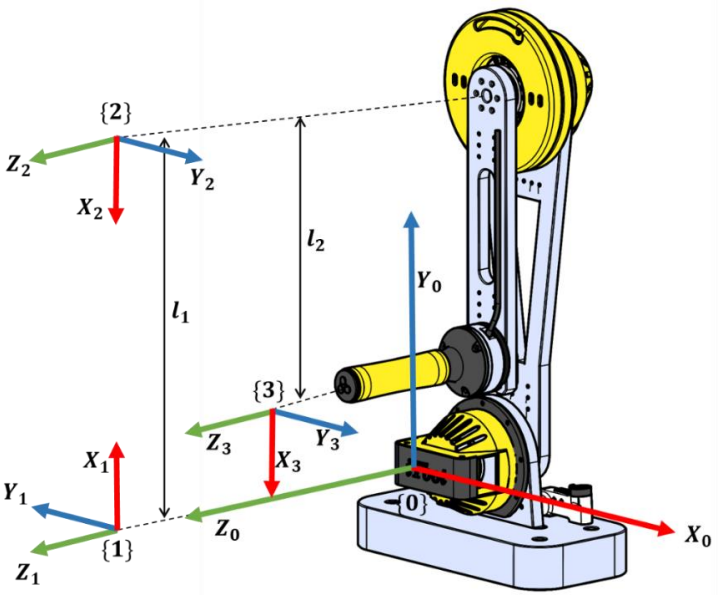

Figure 5.2 Coordinate frame assignment for 2Do iTbot

To obtain the DH parameters, it is assumed that the coordinate frames (i.e., the link-frames which map from one axes of rotation to the successive one) coincide with the corresponding joint axes of rotation, i.e., frame {1} coincides with joint 1, frame {2} with joint 2 and finally, frame {3} define the end-effector position of the iTbot. The frame {0} define the base frame (world frame) of the robot. The DH parameters corresponding to the link-frame assignment in *Figure 5.2* are summarized in *Table 5.1*.

Table 5.1 Modified Denavit-Hartenberg parameters

Joint *(i)*	$\boldsymbol{\alpha_{i-1}}$	$\boldsymbol{d_i}$	$\boldsymbol{a_{i-1}}$	$\boldsymbol{\theta_i}$
1	0	0	0	$\theta_1 + {}^{\pi}/_{2}$
2	0	0	l_1	$\theta_2 + \pi$
3	0	0	l_2	0

where, α_{i-1} is the link twist, a_{i-1} corresponds to link length, d_i stands for link offset, and θ_i is the joint angle of the iTbot.

The general form of a link transformation that relates frame {i} relative to the frame {i-1} [100] is:

$$ {}^{i-1}_{i}T = \begin{bmatrix} {}^{i-1}_{i}R^{3\times3} & {}^{i-1}_{i}P^{3\times1} \\ 0^{1\times3} & 1 \end{bmatrix} \tag{5.1} $$

Where, ${}^{i-1}_{i}R$ is the rotation matrix that represents the frame $\{i\}$ relative to frame $\{i-1\}$ and can be articulated as follows:

$$ {}^{i-1}_{i}R = \begin{bmatrix} \cos\theta_i & -\sin\theta_i & 0 \\ \sin\theta_i \cos\alpha_{i-1} & \cos\theta_i \cos\alpha_{i-1} & -\sin\alpha_{i-1} \\ \sin\theta_i \sin\alpha_{i-1} & \cos\theta_i \sin\alpha_{i-1} & \cos\alpha_{i-1} \end{bmatrix} \tag{5.2} $$

and, ${}^{i-1}_{i}P$ is the vector that locates the origin of the frame $\{i\}$ relative to frame $\{i-1\}$ and can be expressed as the following:

$$ {}^{i-1}_{i}P = [a_{i-1} \quad -sin(\alpha_{i-1})d_i \quad cos(\alpha_{i-1})d_i]^T \tag{5.3} $$

Using Equations (5.1), (5.2), and (5.3), the individual homogeneous transfer matrix that relates two successive frames of the iTbot *Figure 5.2* can be found as:

$$ {}^{0}_{1}T = \begin{bmatrix} cos\ (\theta_1 + \pi/2) & -\sin(\theta_1 + \pi/2) & 0 & 0 \\ \sin(\theta_1 + \pi/2) & cos\ (\theta_1 + \pi/2) & 0 & 0 \\ 0 & 0 & 1 & 0 \\ 0 & 0 & 0 & 1 \end{bmatrix} \tag{5.4} $$

$$ {}^{1}_{2}T = \begin{bmatrix} -\cos(\theta_2) & sin(\theta_2) & 0 & l_1 \\ -\sin(\theta_2) & -\cos(\theta_2) & 0 & 0 \\ 0 & 0 & 1 & 0 \\ 0 & 0 & 0 & 1 \end{bmatrix} \tag{5.5} $$

$$ {}^{2}_{3}T = \begin{bmatrix} 1 & 0 & 0 & l_2 \\ 0 & 1 & 0 & 0 \\ 0 & 0 & 1 & 0 \\ 0 & 0 & 0 & 1 \end{bmatrix} \tag{5.6} $$

The homogenous transformation matrix that relates frame {3} to frame {0} can be obtained by multiplying individual transformation matrices that result in the generic form (5.7).

$$ {}^{0}_{3}T = [{}^{0}_{1}T.\,{}^{1}_{2}T.\,{}^{2}_{3}T] \tag{5.7} $$

$$ {}^{0}_{3}T = \begin{bmatrix} \sin(\theta_1+\theta_2) & \cos(\theta_1+\theta_2) & 0 & l_2\sin(\theta_1+\theta_2) - l_1\sin(\theta_1) \\ -\cos(\theta_1+\theta_2) & \sin(\theta_1+\theta_2) & 0 & l_1\cos(\theta_1) - l_2\cos(\theta_1+\theta_2) \\ 0 & 0 & 1 & 0 \\ 0 & 0 & 0 & 1 \end{bmatrix} \tag{5.8} $$

The single transformation matrix found from Equation (5.8) represents the reference frame's positions and orientations attached to the end-effector with respect to the base reference frame {0}.

The vector that gives the position of the end-effector with respect to frame {0} (*Figure 5.2*) is denoted by Equation (5.9).

$$ {}^{0}_{3}P = \begin{bmatrix} P_x \\ P_y \\ P_z \end{bmatrix} = \begin{bmatrix} l_2\sin(\theta_1+\theta_2) - l_1\sin(\theta_1) \\ l_1\cos(\theta_1) - l_2\cos(\theta_1+\theta_2) \\ 0 \end{bmatrix} \tag{5.9} $$

The above equations are used to define the workspace of the developed iTbot and for the application of various control approaches.

The cartesian linear velocities of the end-effector with respect to the base frame {0} are obtained by differentiating equation 5.9 with respect to time (t) as follows:

$$ {}^{\mathbf{0}}_{\mathbf{3}}\boldsymbol{V} = \begin{bmatrix} v_x \\ v_y \\ v_z \end{bmatrix} = \frac{d\,{}^{\mathbf{0}}_{\mathbf{3}}\boldsymbol{P}}{dt} = \frac{\partial\,{}^{\mathbf{0}}_{\mathbf{3}}\boldsymbol{P}}{\partial\theta_1}\dot{\theta}_1 + \frac{\partial\,{}^{\mathbf{0}}_{\mathbf{3}}\boldsymbol{P}}{\partial\theta_2}\dot{\theta}_2 \tag{5.10} $$

Which can be represented as,

$$\mathbf{{}^{0}_{3}V} = {}^{0}J(\theta)\begin{bmatrix}\dot{\theta}_1\\ \dot{\theta}_2\end{bmatrix} = {}^{0}J(\theta)\dot{\boldsymbol{\theta}} \tag{5.11}$$

$$\text{Where, } {}^{0}J(\theta) = \begin{bmatrix} l_2cos(\theta_1+\theta_2) - l_1cos(\theta_1) & l_2cos(\theta_1+\theta_2) \\ l_2sin(\theta_1+\theta_2) - l_1sin(\theta_1) & l_2sin(\theta_1+\theta_2) \\ 0 & 0 \end{bmatrix} \tag{5.12}$$

${}^{0}J(\theta)$ is the Jacobians that relates the joint velocities to Cartesian linear velocities of the end-effector of the robot. Jacobians are time-varying linear transformations. Superscript '0' on $J(\theta)$ define the Jacobian written in frame $\{0\}$. As the iTbot is a 2DoFs planar robot and there is no linear velocity along Z-axis. Throughout the rest of this thesis $\mathbf{{}^{0}_{3}V}$ and ${}^{0}J(\theta)$ are defined as follows:

$$\mathbf{{}^{0}_{3}V} = \begin{bmatrix}v_x\\ v_y\end{bmatrix} \; and \;\; {}^{0}J(\theta) = \begin{bmatrix} l_2cos(\theta_1+\theta_2) - l_1cos(\theta_1) & l_2cos(\theta_1+\theta_2) \\ l_2sin(\theta_1+\theta_2) - l_1sin(\theta_1) & l_2sin(\theta_1+\theta_2) \end{bmatrix} \tag{5.13}$$

The Jacobian matrices can be derived in any frame. Changing the frame of reference of a Jacobian is accomplished utilizing the following relationship:

$${}^{A}J(\theta) = {}^{A}_{B}R\,{}^{B}J(\theta) \tag{5.14}$$

5.2 Inverse Kinematics

The previous section has shown how to determine the end-effector position given the robot's joint angles. A problem of practical interest is the inverse problem where the desired position of the end-effector with respect to the base frame is given, and finding out the required joint angles is needed. Here, the geometric approach for solving the inverse kinematics of iTbot is explained.

5.2.1 Geometric inverse kinematic solution

In a geometric approach to finding an inverse kinematic solution, the robot spatial geometry is decomposed into several plane-geometry problems. As the iTbot is a 2DoFs planar robot, plane geometry can be applied directly to find a solution.

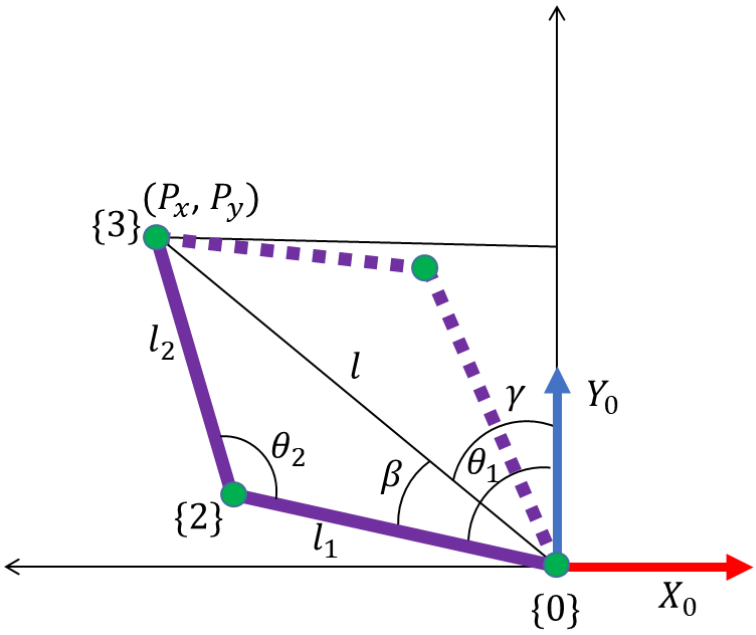

Figure 5.3 Geometric inverse kinematics model of the 2DoF iTbot

Figure 5.3 shows the triangle formed by l_1, l_2 and the line joining the origin of frame {0} with the origin of frame {3}. Considering the solid triangle, by applying the law of cosines θ_2 can be solved as:

$$\theta_2 = \cos^{-1}\left(\frac{{l_1}^2 + {l_2}^2 - l^2}{2l_1 l_2}\right) \tag{5.15}$$

Where, $l^2 = {P_x}^2 + {P_y}^2$

For this triangle to exist, the condition $l = \sqrt{{P_x}^2 + {P_y}^2} \leq l_1 + l_2$ must need to be satisfied. This condition would be checked at this point in a computational algorithm to verify the existence of solutions.

This condition is not satisfied when the target point is out of reach of the robot. Assuming a solution exists, this Equation can only be solved for that value of θ_2 that lies between 0 and ± 180 degrees because only for these values does the triangle in Fig. 5.3 exist.

To solve for θ_1, the expressions for angles γ and β has been found as indicated in Fig. 5.3. First, γ may be in any quadrant, depending on the signs of P_x and P_y. The angle γ obtained by using two-argument arctangent:

$$\gamma = \text{Atan2}(-P_x, P_y) \tag{5.16}$$

Again, by applying the law of cosines, β can be solved as:

$$\beta = \cos^{-1}\left(\frac{{l_1}^2 + l^2 - {l_2}^2}{2ll_1}\right) \tag{5.17}$$

Then the angle θ_1 can be obtained as:

$$\theta_1 = \gamma + \beta \tag{5.18}$$

The dashed lines in *Figure 5.3* represent the other possible configuration of the robot, which would lead to the same position of the frame {3}. The other possible solution (the one indicated by the dashed line) is found by symmetry:

$$\acute{\theta_2} = -\theta_2 \tag{5.19}$$

$$\theta_1 = \gamma - \beta \tag{5.20}$$

Above mentioned geometric approach only applicable to the joint angles between 0 and ± 180 degrees. However, inside the reachable workspace, there are two possible orientations of the end-effector except for the workspace's boundaries. One single solution can be obtained by using additional constrain for the joint angles. In practice, the iTbot programming always compares the angular distances of each joint from both solutions from the robot's current angular position. It discards the solution that gives the higher combined angular distance.

5.3 Dynamics

To simulate the joint movements of iTbot and for experimentation using nonlinear control such as Computed Torque control, the dynamics of iTbot were analyzed. Dynamics calculates the motion of bodies under the action of external forces. The iterative Newton-Euler formulation and the Lagrangian formulation are used widely to develop the dynamic model of manipulators. The Newton-Euler approach is computationally more efficient compared to the Lagrangian approach [100] for 2 DoF robots such as iTbot. Therefore, the iterative Newton-Euler method [102] was used to develop a dynamic model for this robot.

5.3.1 Iterative Newton-Euler Formulation:

In this approach, each link of the robot is considered as a rigid body. If the center of mass of a rigid body is accelerating with an acceleration $\dot{\boldsymbol{V}}_c$. Then, the force, F, acting at the center of mass and causing this acceleration is given by Newton′s equation

$$\boldsymbol{F} = m\dot{\boldsymbol{V}}_c \tag{5.21}$$

Where, m is the mass of the rigid body.

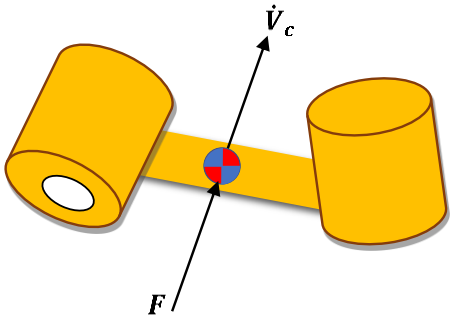

Figure 5.4 A force F acting at the center of mass of a body causes acceleration at $\dot{V}_c$

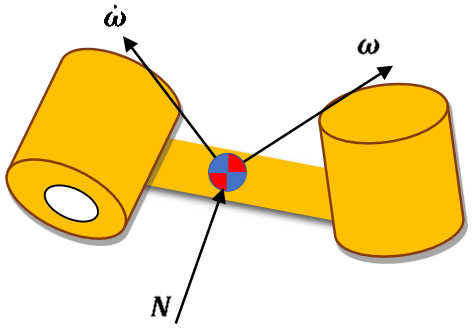

Figure 5.5 A moment N is acting on a body, and the body is rotating with velocity ω and accelerating at $\dot{\omega}$.

If the rigid body rotating with angular velocity ω and with angular acceleration $\dot{\omega}$, then the resulting moment, N, given by Euler's Equation [100]

$$\boldsymbol{N} = I_c\dot{\boldsymbol{\omega}} + \boldsymbol{\omega} \times I_c\boldsymbol{\omega} \tag{5.22}$$

where I_c is the inertia tensor of the body at its center of mass.

Based on the knowledge of the kinematics and the mass distribution information of the robot, the joint torques (τ_i), as well as the dynamic model of a manipulator, can be computed using the following steps:

5.3.1.1 Outward iterations:

The acting inertial force and torque at the center of mass of each link are calculated iteratively, starting with link 1 and moving successively, link by link, outward to link *n*. For this purpose, it is necessary to compute the rotational velocity and linear and rotational acceleration of the center of mass of each link of the robot at any given instant. The propagation of the rotational velocity from link to link and the equation for transforming angular acceleration from one link to the next is given by [100]:

$$^{i+1}_{i+1}\boldsymbol{\omega} = {}^{i+1}_{i}R\ {}^{i}_{i}\boldsymbol{\omega} + \dot{\boldsymbol{\theta}}_{i+1}\ {}^{i+1}_{i+1}\hat{Z} \tag{5.23}$$

$$^{i+1}_{i+1}\dot{\boldsymbol{\omega}} = {}^{i+1}_{i}R\ {}^{i}_{i}\dot{\boldsymbol{\omega}} + {}^{i+1}_{i}R\ {}^{i}_{i}\boldsymbol{\omega} \times \dot{\boldsymbol{\theta}}_{i+1}\ {}^{i+1}_{i+1}\hat{Z} + \ddot{\boldsymbol{\theta}}_{i+1}\ {}^{i+1}_{i+1}\hat{Z} \tag{5.24}$$

The linear acceleration of each link frame origin and the corresponding linear acceleration transformation to the link center of mass obtained by the following iterative equations [100]:

$$ {}^{i+1}_{i+1}\dot{\boldsymbol{V}} = {}^{i+1}_{i}R[\,{}^{i}_{i}\dot{\boldsymbol{\omega}} \times {}^{i}_{i+1}\boldsymbol{P} + {}^{i}_{i}\boldsymbol{\omega} \times \left({}^{i}_{i}\boldsymbol{\omega} \times {}^{i}_{i+1}\boldsymbol{P}\right) + {}^{i}_{i}\dot{\boldsymbol{V}}\,] \tag{5.25} $$

$$ {}^{i+1}_{i+1}\dot{\boldsymbol{V}}_c = {}^{i+1}_{i+1}\dot{\boldsymbol{\omega}} \times {}^{i+1}_{i+1}\boldsymbol{P}_c + {}^{i+1}_{i+1}\boldsymbol{\omega} \times \left({}^{i+1}_{i+1}\boldsymbol{\omega} + {}^{i+1}_{i+1}\boldsymbol{P}_c\right) + {}^{i+1}_{i+1}\dot{\boldsymbol{V}} \tag{5.26} $$

Here, the parameters with subscript *'c'* represent that it is in an imaginary frame $\{C_i\}$, attached to each link, having its origin located at the center of mass of the link and having the same orientation as the link frame, {i}.

Having computed the linear and angular acceleration of the mass center of each link, the inertial force and torque acting at the center of mass of each link is obtained by the Newton-Euler equations as [100]:

$$ {}^{i+1}_{i+1}\boldsymbol{F} = m_{i+1}\,{}^{i+1}_{i+1}\dot{\boldsymbol{V}}_c \tag{5.27} $$

$$ {}^{i+1}_{i+1}\boldsymbol{N} = {}^{i+1}_{i+1}I_c\,{}^{i+1}_{i+1}\dot{\boldsymbol{\omega}} + {}^{i+1}_{i+1}\boldsymbol{\omega} \times {}^{i+1}_{i+1}I_c\,{}^{i+1}_{i+1}\boldsymbol{\omega} \tag{5.28} $$

5.3.1.2 Inward iterations:

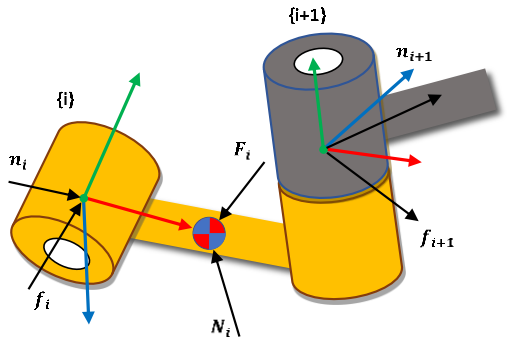

Figure 5.6 The force balance, including inertial forces, for a single robot link. Where, f_i and n_i represents the force and torque exerted on link i by the link i-1.

Now, the force and moment balance equation based on a free-body diagram of a typical robot link, as shown in

$$ {}^{i}_{i}\boldsymbol{f} = {}_{i+1}{}^{i}R\ {}^{i+1}_{i+1}\boldsymbol{f} + {}^{i}_{i}\boldsymbol{F} \tag{5.31} $$

$$ {}^{i}_{i}\boldsymbol{n} = {}^{i}_{i}\boldsymbol{N} + {}_{i+1}{}^{i}R\ {}^{i+1}_{i+1}\boldsymbol{n} + {}^{i}_{i}\boldsymbol{P}_c \times {}^{i}_{i}\boldsymbol{F} + ({}_{i+1}{}^{i}\boldsymbol{P} \times {}_{i+1}{}^{i}R\ {}^{i+1}_{i+1}\boldsymbol{f} \tag{5.32} $$

can be written as:

$$ {}^{i}_{i}\boldsymbol{F} = {}^{i}_{i}\boldsymbol{f} - {}_{i+1}{}^{i}R\ {}^{i+1}_{i+1}\boldsymbol{f} \tag{5.29} $$

$$ {}^{i}_{i}\boldsymbol{N} = {}^{i}_{i}\boldsymbol{n} - {}_{i+1}{}^{i}\boldsymbol{n} + \left(-{}^{i}_{i}\boldsymbol{P}_c\right) \times {}^{i}_{i}\boldsymbol{f} - ({}_{i+1}{}^{i}\boldsymbol{P} - {}^{i}_{i}\boldsymbol{P}_c) \times {}_{i+1}{}^{i}\boldsymbol{f} \tag{5.30} $$

Finally, rearrange the force and torque equations so that they appear as iterative relationships from a higher-numbered neighbor to a lower-numbered neighbor:

$$ {}^{i}_{i}\boldsymbol{f} = {}_{i+1}{}^{i}R\ {}^{i+1}_{i+1}\boldsymbol{f} + {}^{i}_{i}\boldsymbol{F} \tag{5.31} $$

$$ {}^{i}_{i}\boldsymbol{n} = {}^{i}_{i}\boldsymbol{N} + {}_{i+1}{}^{i}R\ {}^{i+1}_{i+1}\boldsymbol{n} + {}^{i}_{i}\boldsymbol{P}_c \times {}^{i}_{i}\boldsymbol{F} + ({}_{i+1}{}^{i}\boldsymbol{P} \times {}_{i+1}{}^{i}R\ {}^{i+1}_{i+1}\boldsymbol{f} \tag{5.32} $$

These equations are evaluated link by link, starting from link n and working inward toward the robot's base.

The required joint torques are found by taking the $\hat{Z}$ component of the torque applied by one link on its neighbor:

$$ \boldsymbol{\tau}_i = {}^{i}_{i}\boldsymbol{n}^{\boldsymbol{T}}\,{}^{i}_{i}\hat{Z} \tag{5.33} $$

If the inertia tensor of each link of the iTbot at its center of mass is given by:

$$I_{c1} = \begin{bmatrix} I_{x1} & 0 & 0 \\ 0 & I_{y1} & 0 \\ 0 & 0 & I_{z1} \end{bmatrix} \tag{5.34}$$

$$\text{And, } I_{c2} = \begin{bmatrix} I_{x2} & 0 & 0 \\ 0 & I_{y2} & 0 \\ 0 & 0 & I_{z2} \end{bmatrix} \tag{5.35}$$

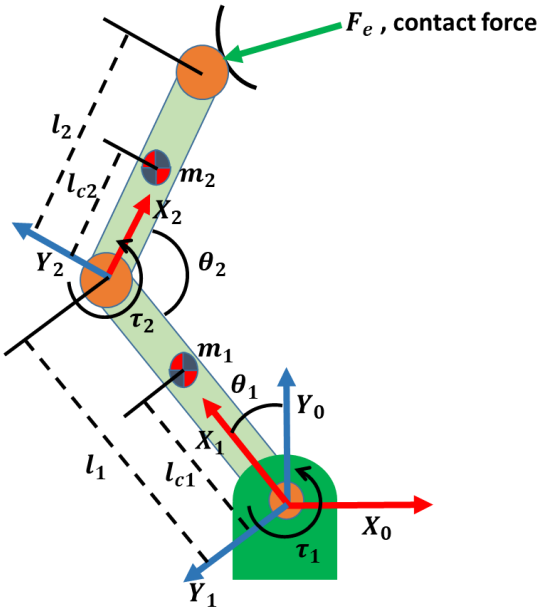

Figure 5.7 iTbot nomenclature for dynamic modeling with contact force at the end-effector.

Then, the joint torques of the iTbot for vertical configuration with active gravity compensation, based on the nomenclature provided in *Figure 5.7*, can be found by the iterative Newton-Euler formulation as:

$$\tau_1 = (m_2 l_1^2 - 2m_2 l_1 l_{c2} \cos(\theta_2) + m_1 l_{c1}^2 + m_2 l_{c2}^2 + I_{z1} + I_{z2})\ddot{\theta}_1 \quad (5.36)$$
$$+ (m_2 l_{c2}^2 - m_2 l_1 l_{c2} \cos(\theta_2) + I_{z2})\ddot{\theta}_2 + m_2 l_1 l_{c2} \sin(\theta_2)\, \dot{\theta}_2^2$$
$$+ 2m_2 l_1 l_{c2} \sin(\theta_2)\dot{\theta}_1\dot{\theta}_2 + (m_2 l_{c2} \sin(\theta_1 + \theta_2)$$
$$- m_1 l_{c1} \sin(\theta_1) - m_2 l_1 \sin(\theta_1))g$$

$$\tau_2 = (I_{z2} + m_2 l_{c2}(l_{c2} - l_1 \cos(\theta_2)))\ddot{\theta}_1 + (m_2 l_{c2}^2 + I_{z2})\ddot{\theta}_2 \quad (5.37)$$
$$- m_2 l_1 l_{c2} \sin(\theta_2)\, \dot{\theta}_1^2 + (m_2 l_{c2} \sin(\theta_1 + \theta_2))g$$

Equations (5.36) and (5.37) give expressions for the torque at the actuators as a function of joint position, velocity, and acceleration. The dynamic Equation of iTbot can be written in the form given by Equation (5.38):

$$\boldsymbol{\tau} = M(\boldsymbol{\theta})\ddot{\boldsymbol{\theta}} + V\left(\boldsymbol{\theta}, \dot{\boldsymbol{\theta}}\right) + G(\boldsymbol{\theta}) \quad (5.38)$$

where $\boldsymbol{\tau} = \begin{bmatrix} \tau_1 \\ \tau_2 \end{bmatrix}$ and $\ddot{\boldsymbol{\theta}} = \begin{bmatrix} \ddot{\theta}_1 \\ \ddot{\theta}_2 \end{bmatrix}$ are the 2×1 torque and acceleration vector. $M(\boldsymbol{\theta})$ is the 2×2 mass matrix given as:

$$M(\boldsymbol{\theta}) =$$

$$\begin{bmatrix} m_2 l_1^2 - 2m_2 l_1 l_{c2} \cos(\theta_2) + m_1 l_{c1}^2 + m_2 l_{c2}^2 + I_{z1} + I_{z2} & m_2 l_{c2}^2 - m_2 l_1 l_{c2} \cos(\theta_2) + I_{z2} \\ I_{z2} + m_2 l_{c2}(l_{c2} - l_1 \cos(\theta_2)) & m_2 l_{c2}^2 + I_{z2} \end{bmatrix} \quad (5.39)$$

$V\left(\theta, \dot{\theta}\right)$ is a 2×1 vector of centrifugal and Coriolis terms given as:

$$V(\boldsymbol{\theta}, \dot{\boldsymbol{\theta}}) = \begin{bmatrix} m_2 l_1 l_{c2} \sin(\theta_2)\, \dot{\theta}_2^2 + 2 m_2 l_1 l_{c2} \sin(\theta_2) \dot{\theta}_1 \dot{\theta}_2 \\ -m_2 l_1 l_{c2} \sin(\theta_2)\, \dot{\theta}_1^2 \end{bmatrix} \tag{5.40}$$

$G(\theta)$ is a 2×1 vector of gravity terms given as :

$$G(\boldsymbol{\theta}) = \begin{bmatrix} (m_2 l_{c2} \sin(\theta_1 + \theta_2) - m_1 l_{c1} \sin(\theta_1) - m_2 l_1 \sin(\theta_1)) g \\ (m_2 l_{c2} \sin(\theta_1 + \theta_2)) g \end{bmatrix} \tag{5.41}$$

If $F(\theta, \dot{\theta}) \in \mathbb{R}^2$ is the vector of nonlinear Coulomb friction and expressed by equation (5.40).

$$F(\boldsymbol{\theta}, \dot{\boldsymbol{\theta}}) = c.sgn(\dot{\boldsymbol{\theta}}). \tag{5.42}$$

Then by adding friction to the model, the dynamic Equation (5.38) results in Equation (5.39):

$$\boldsymbol{\tau} = M(\boldsymbol{\theta})\ddot{\boldsymbol{\theta}} + V(\boldsymbol{\theta}, \dot{\boldsymbol{\theta}}) + G(\boldsymbol{\theta}) + F(\boldsymbol{\theta}, \dot{\boldsymbol{\theta}}) \tag{5.43}$$

Furthermore, to consider the effect of the contact force acting on the end-effector, the left side of the Equation (5.39) can be replaced by

$$\boldsymbol{\acute{\tau}} = \boldsymbol{\tau} - J^T(\boldsymbol{\theta}) \boldsymbol{F_e} \tag{5.44}$$

Where, $\boldsymbol{F_e} = \begin{bmatrix} F_x \\ F_y \end{bmatrix}$ is the vector of contact force at the end-effector of the iTbot, which is obtained from the force sensor mounted on the iTbot's end-effector, $J(\boldsymbol{\theta})$ is the jacobian matrix of the iTbot. The Jacobean matrix, $J(\boldsymbol{\theta})$And contact force, $\boldsymbol{F_e}$, must be written in the same frame of the robot.

For the horizontal configuration of the iTbot, the term $G(\boldsymbol{\theta})$ in the dynamic equation becomes zero. All other terms remain the same as of vertical configuration of the iTbot.

***iTbot* Parameters:** The center of mass of the iTbot's links was computed using SolidWorks software (see APPENDIX – A for Links 1 and 2)

CHAPTER 6

CONTROL AND SIMULATION

6.1 Proportional-Integral-Derivative (PID) Control

For initial testing and control of the developed iTbot, a PID control technique has been used [100]. The general layout of the PID control approach used for iTbot is depicted in Figure 6.1. The joint torque commands are expressed by Equation (6.1):

$$\tau = K_P(\theta_d - \theta) + K_V\left(\dot{\theta}_d - \dot{\theta}\right) + K_I \int (\theta_d - \theta)\, dt \tag{6.1}$$

Where,

$\theta_d, \theta \in \mathbb{R}^2$ are the vectors of desired and measured joint angles,

$\dot{\theta_d}$, $\dot{\theta} \in \mathbb{R}^2$are the vectors of desired and measured joint velocities,

K_P, K_V, K_I are the diagonal positive definite gain matrices,

$\tau \in \mathbb{R}^2$ is the generalized torque vector.

E is an error vector and its derivative $\dot{E}$ given by equation (6.2)(6.3):

$$E = \theta_d - \theta \tag{6.2}$$

$$\dot{E} = \dot{\theta_d} - \dot{\theta} \tag{6.3}$$

Therefore, this Equation (6.1) has been reformulated as an error equation (6.4):

$$\tau = K_P E + K_V \dot{E} + K_I \int E\, dt \tag{6.4}$$

By decoupling relation (6.4), individual torque command for each joint is given by Equation (6.5).

$$\tau_i = K_{P_i} e_i + K_{V_i} \dot{e}_i + K_{I_i} \int e_i\, dt \tag{6.5}$$

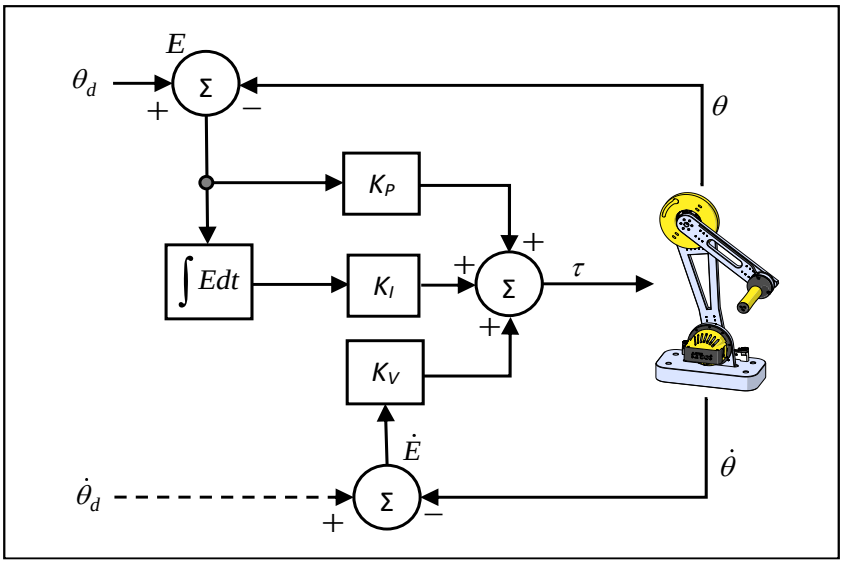

Figure 6.1 Schematic of PID control

6.1.1 Simulation with PID control

With the SIMULINK (MathWorks, USA) software, the simulations for iTbot with PID control have been done. A brief description of the trajectories used in the simulations (throughout this CHAPTER 6) are presented below:

Joint-1 trajectory:

The trajectory runs from 0° position of Joint-1. After 1 second of waiting, it first moves to -45° position in 3 seconds, and then gets back to 0° position in 3 seconds; Afterwards the joint 1 moves

to positive direction 45° within 3 seconds and returns to 0° position within 3 seconds, where it waits for 1 more second. The associated velocity and acceleration profile can be seen in *Figure 6.2*.

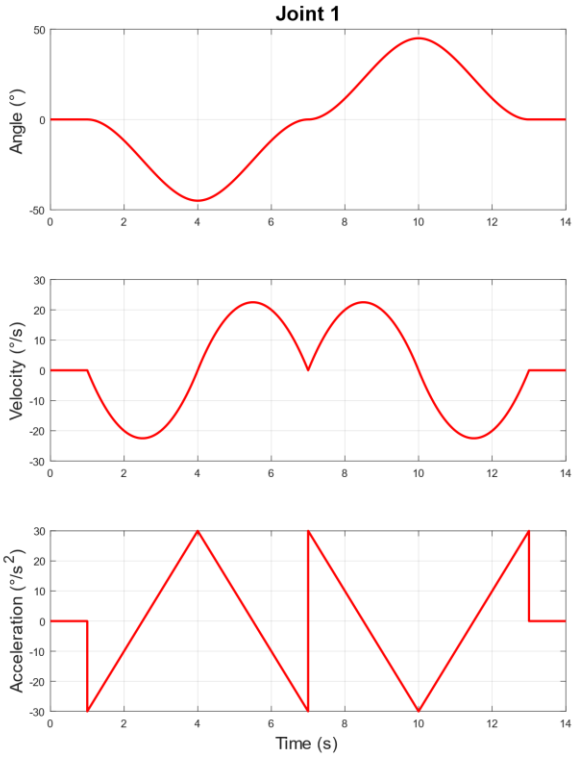

Figure 6.2 Generated trajectory for Joint 1 movement

Joint-2 trajectory:

The trajectory runs from 0° position of Joint-2. After 1 second of waiting, it first moves to -90° position in 3 seconds, and then gets back to 0° position in 3 seconds; Afterwards the joint 2 moves to positive direction 90° within 3 seconds and returns to 0° position within 3 seconds, where it waits for 1 more second. The associated velocity and acceleration profile can be seen in *Figure 6.3*. Simultaneous movement of Joint 1 and Joint 2 can be seen in *Figure 6.4*.

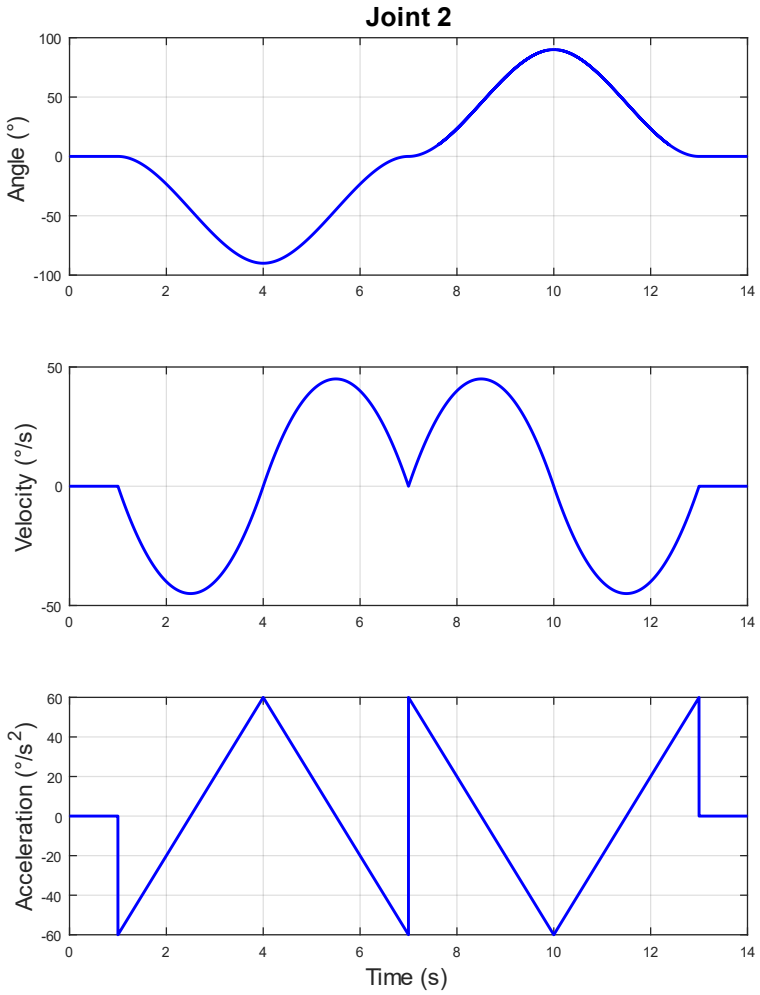

Figure 6.3 Generated trajectory for Joint 2 movement

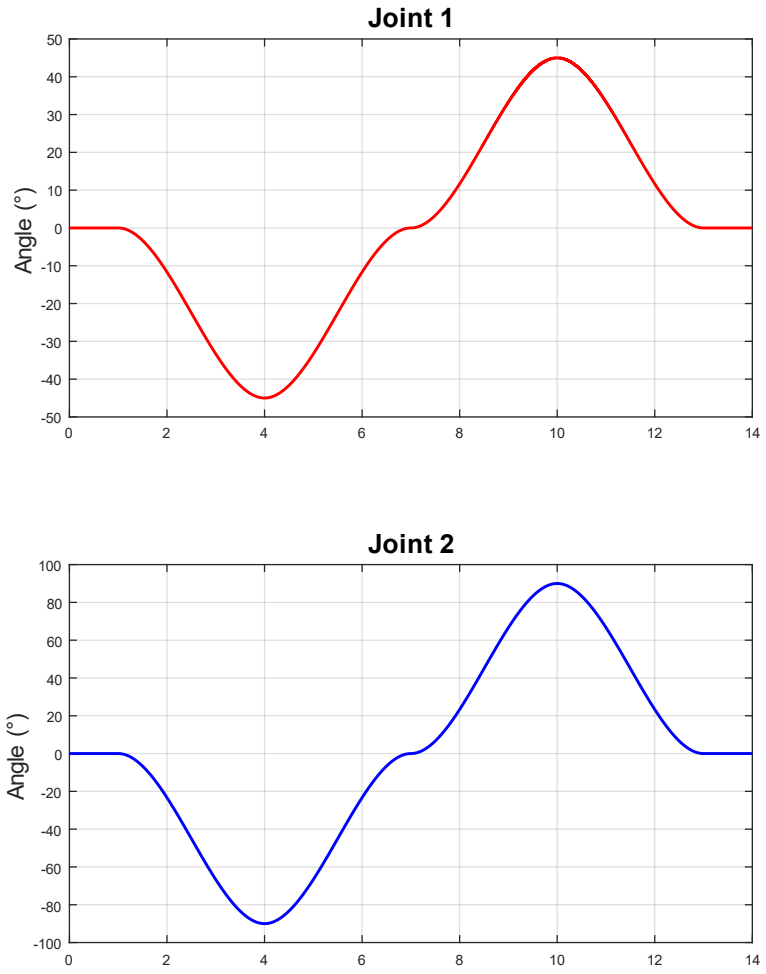

Figure 6.4 Generated simultaneous motion for Joint 1 and Joint 2

In all cases, initial velocities and acceleration are given as zero. Note that the desired trajectories and associated velocities were generated using the cubic polynomial approach [100]. The control gains used for the simulation were found by trial and error and are as follows:

$$K_P = diag[700 \quad 700],$$

$$K_V = diag[10 \quad 18], \text{ and}$$

$$K_I = diag[0.1 \quad 0.1].$$

6.1.1.1 iTbot Vertical Configuration: Simultaneous Joint movements (PID)

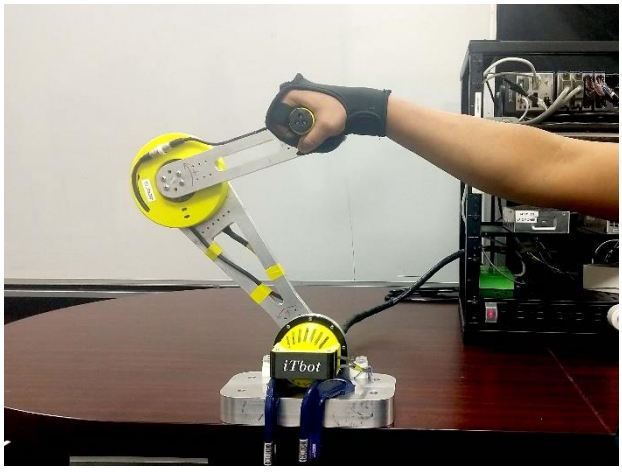

Figure 6.5 Vertical Configuration of iTbot

Both joints (Joint-1 – range: +45° -45°, & Joint-2 – range: +90° -90°) move at the same time period (14s) and follows the trajectory mentioned in *Figure 6.4* while iTbot was in its vertical configuration (*Figure 6.5*). The simulated results can be seen in *Figure 6.6*, *Figure 6.7*, and *Figure 6.8*. The tracking performance of two joints' simultaneous movement can be seen from *Figure 6.6*, where 1st column corresponds to Joint-1, and the 2nd column corresponds to Joint-2. The first row

shows the trajectory comparison (Given joint angles – red dotted line, Measured joint angles – solid blue line) for two joints. The second row shows the tracking error, and the third row shows the measured torque from the simulation. Here the maximum tracking error was less than 0.4° (0.88%), which proves that the tracking performance is quite good. *Figure 6.7 and Figure 6.8* show the plots of the joints separately. Here, the given velocities (third row) are denoted with the red dotted line, and the measured trajectory from the simulation is shown with a solid blue line. Maximum joint torque for iTbot's Joint-1 was found to be -4.5 Nm and +4.5 Nm; for Joint-2, the maximum joint torque is -1 Nm and +1 Nm. The positive and negative signs denoted the direction of the joint torques.

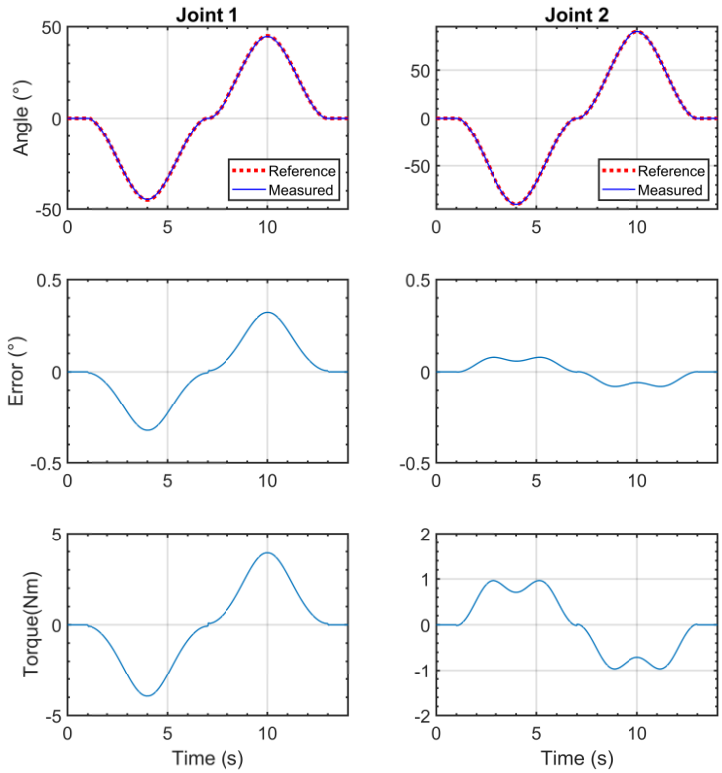

Figure 6.6 Both joints' simultaneous motion (PID) while iTbot is in vertical configuration

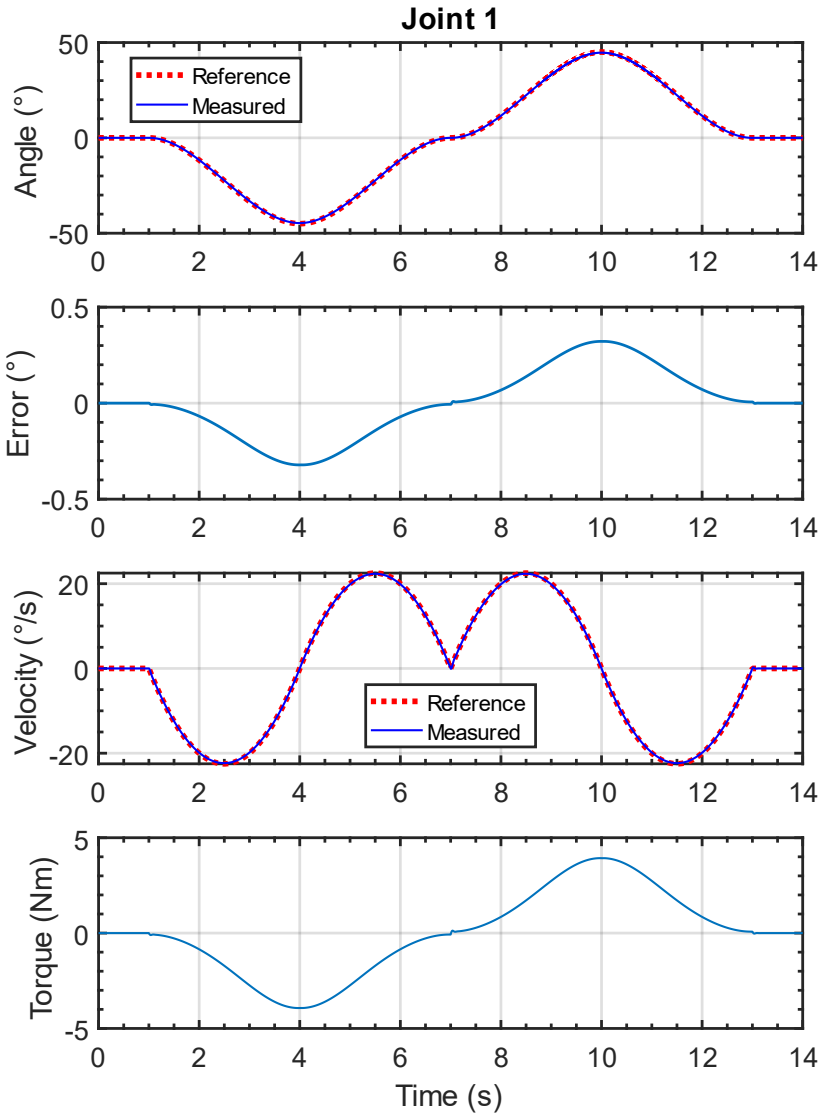

Figure 6.7 Both joints' simultaneous movement (detail of Joint-1 movement with velocity comparison (PID) while iTbot is in vertical configuration

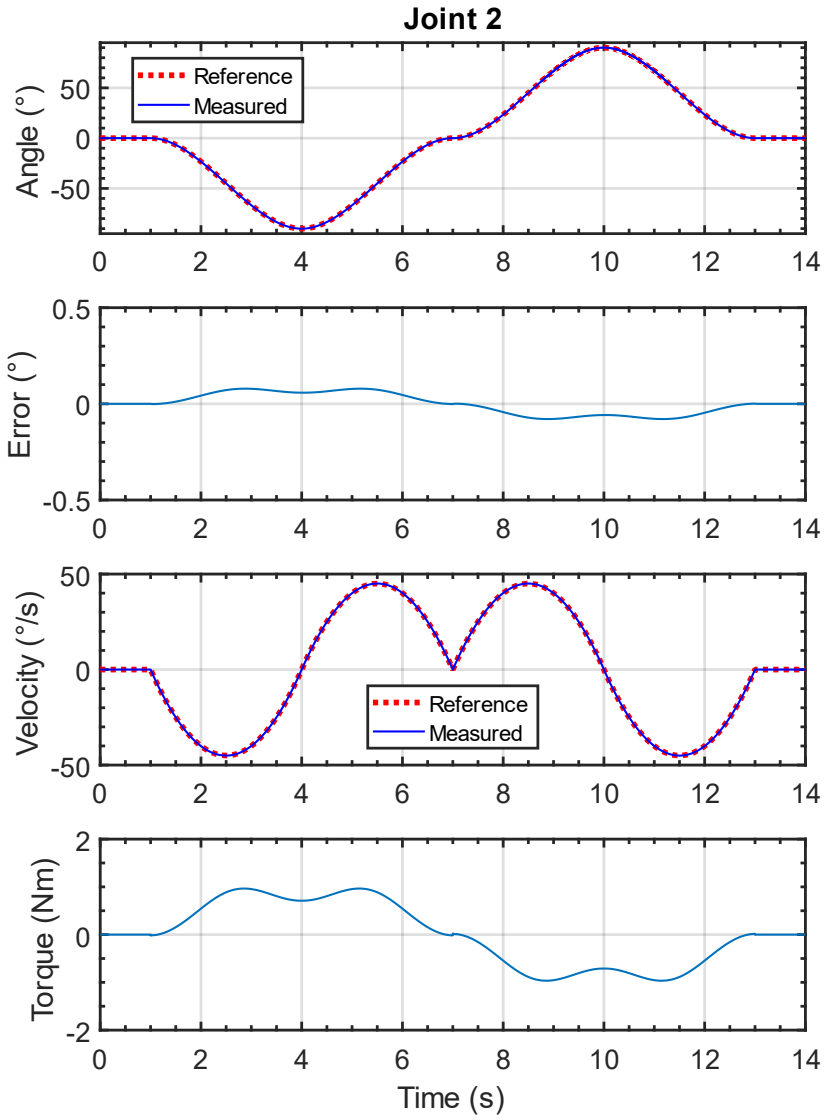

Figure 6.8 Both joints' simultaneous movement (detail of Joint-2 movement with velocity comparison (PID) while iTbot is in vertical configuration

6.1.1.2 iTbot Horizontal Configuration: Simultaneous Joint movements (PID)

Figure 6.9 Horizontal Configuration of iTbot

The same trajectory (*Figure 6.4*) has been simulated for iTbot's horizontal configuration (*Figure 6.9*). The simulated results can be seen in *Figure 6.10*, *Figure 6.11*, and *Figure 6.12*. The tracking performance of two joints' simultaneous movement can be seen from *Figure 6.10*, where 1st column corresponds to Joint-1, and the 2nd column corresponds to Joint-2. The first row shows the trajectory comparison (Given joint angles – red dotted line, Measured joint angles – solid blue line) for two joints. The second row shows the tracking error, and the third row shows the measured torque from the simulation. Here the tracking error was close to zero, which proves that the tracking performance is excellent. *Figure 6.11* and *Figure 6.12* show the plots of the joints separately. Here, the given velocities (third row) are denoted with the red dotted line, and the measured trajectory from the simulation is shown with a solid blue line. Maximum joint torque for iTbot's Joint-1 was found to be -0.15 Nm and +0.15 Nm; for Joint-2, the maximum joint torque is -0.06 Nm and +0.06 Nm. The positive and negative signs denoted the direction of the joint torques.

It is to be noted that, in the horizontal configuration, there is no gravitational effect on either Joint 1 or Joint 2 motor, and due to this, the generated torque is lower than generated torque for the same trajectory while the robot was in vertical configuration.

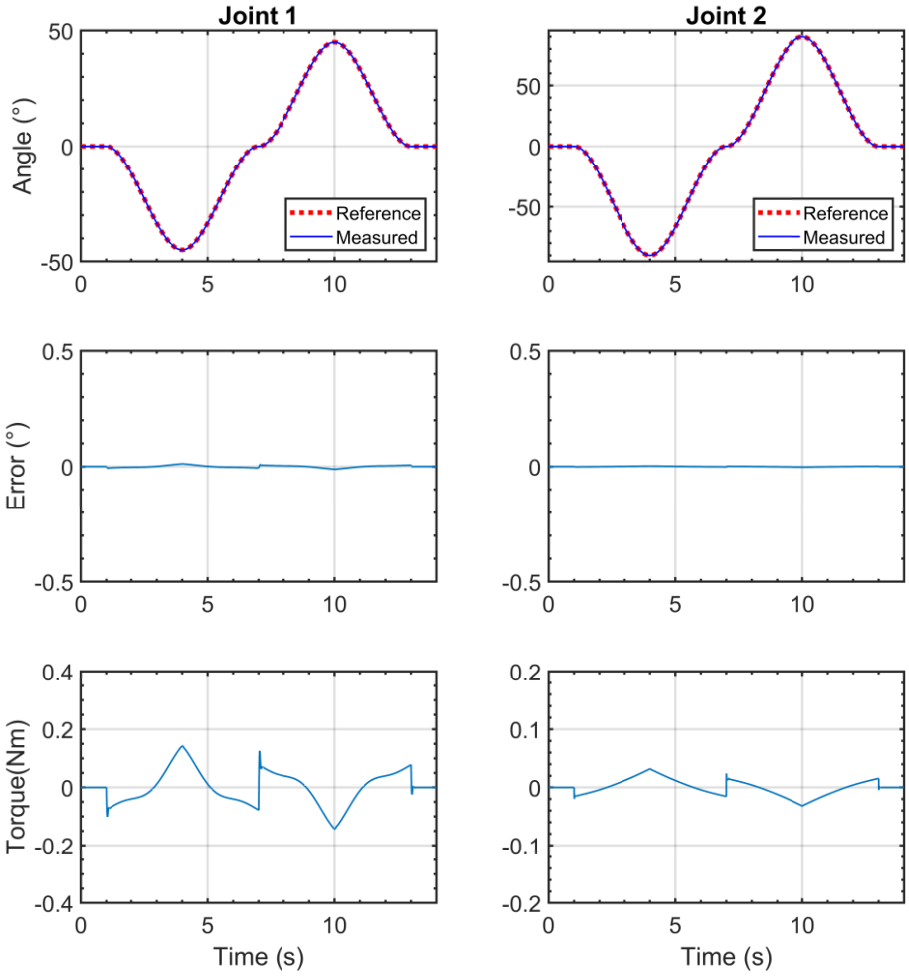

Figure 6.10 Both joints' simultaneous motion (PID) while iTbot is in horizontal configuration

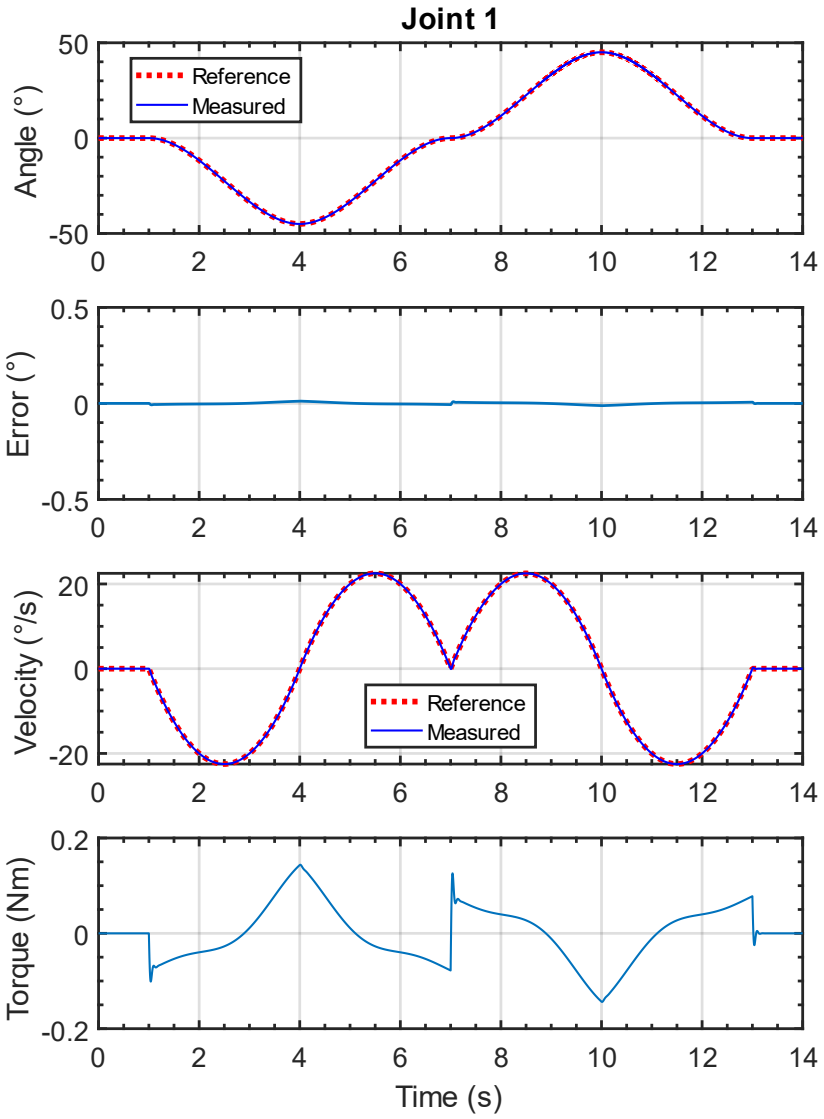

Figure 6.11 Both joints' simultaneous movement (detail of Joint-1 movement with velocity comparison (PID) while iTbot is in horizontal configuration

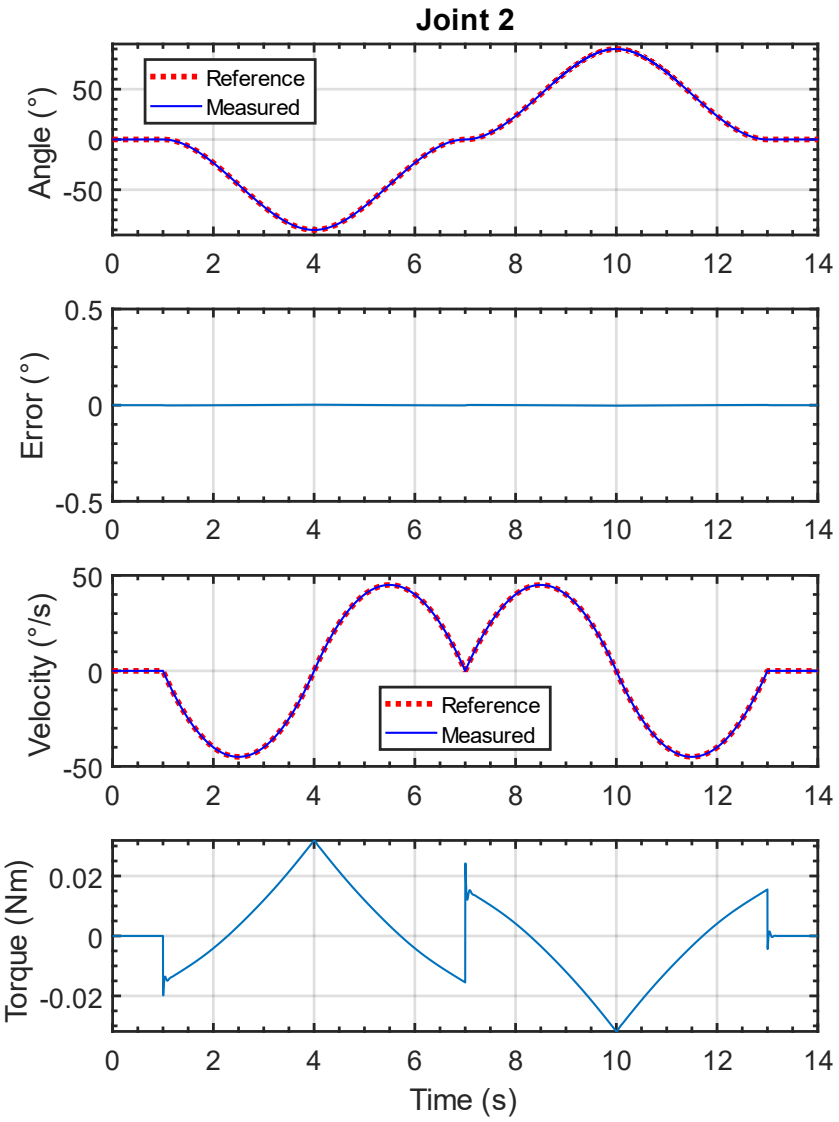

Figure 6.12 Both joints' simultaneous movement (detail of Joint-2 movement with velocity comparison (PID) while iTbot is in horizontal configuration

6.2 Modified Computed Torque Control (mCTC)

To realize better tracking performance of the iTbot, the dynamic models of the iTbot, including the effect of Gravity in the vertical and horizontal orientation, have been implemented using a nonlinear computed torque control (CTC) technique.

The dynamic behavior of the iTbot is expressed by the well-known rigid body dynamic equation (6.6):

$$M(\theta)\ddot{\theta} + V\left(\theta, \dot{\theta}\right) + G(\theta) + F\left(\theta, \dot{\theta}\right) = \tau \tag{6.6}$$

Where,

$\theta \in \mathbb{R}^2$ is the joint variables vector,

τ is the generalized torque vector,

$M(\theta) \in \mathbb{R}^{2\times2}$ is the inertia matrix,

$V\left(\theta, \dot{\theta}\right) \in \mathbb{R}^2$ is the Coriolis/ centrifugal vector,

$G(\theta) \in \mathbb{R}^2$ is the gravity vector,

$F\left(\theta, \dot{\theta}\right) \in \mathbb{R}^2$ is the friction vector.

The friction vector is modeled as a nonlinear Coulomb friction formulated by Equation (6.7):

$$\tau_{friction} = F\left(\theta, \dot{\theta}\right) = c.sgn\left(\dot{\theta}\right) \tag{6.7}$$

Where,

c is the Coulomb-friction constant.

Equation (6.6) can be written as (6.8) for controller implementation:

$$\ddot{\theta} = -M^{-1}(\theta)\left[V\left(\theta,\dot{\theta}\right) + G(\theta) + F\left(\theta,\dot{\theta}\right)\right] + M^{-1}(\theta)\tau \qquad (6.8)$$

$M^{-1}(\theta)$ always exists since $M(\theta)$ is symmetrical and positive definite.

The schematic of the used modified computed torque control technique is shown in *Figure 6.13*. As a modification to the conventional computed torque control approach, an integral term was added to have a better tracking performance and to compensate for the trajectory tracking error that can result from imperfect parameter estimation namely friction, and other external disturbances.

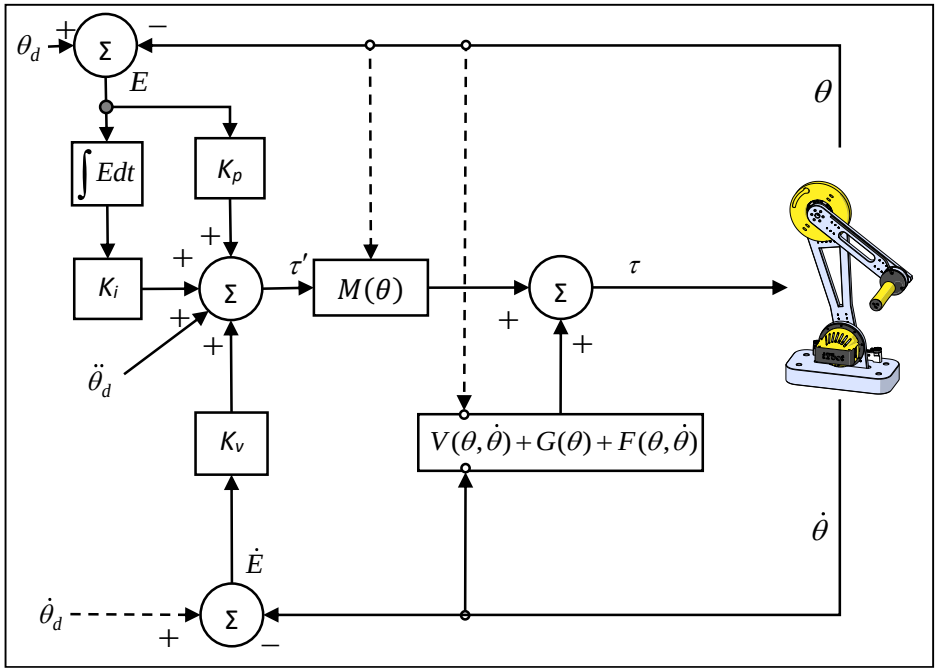

Figure 6.13 Schematic of Modified Computed Torque Control (mCTC)

The control torque in *Figure 6.13* is expressed by:

$$\tau = M(\theta)\left[\ddot{\theta_d} + K_v\left(\dot{\theta}_d - \dot{\theta}\right) + K_p(\theta_d - \theta) + K_i \int (\theta_d - \theta)\, dt\right] + V\left(\theta, \dot{\theta}\right) + G(\theta) + F\left(\theta, \dot{\theta}\right) \tag{6.9}$$

From relations (6.6) and (6.9), Equation (6.10) is found:

$$\ddot{\theta} = \ddot{\theta_d} + K_v\left(\dot{\theta}_d - \dot{\theta}\right) + K_p(\theta_d - \theta) + K_i \int (\theta_d - \theta)\, dt \tag{6.10}$$

Where,

$\theta_d, \dot{\theta}_d,$ and $\ddot{\theta}_d$ are the desired position, velocity, and acceleration, respectively,

K_p, K_v, and K_i diagonal positive definite matrices.

The error vector E and its derivatives are given by Equation (6.11), (6.12) & (6.13):

$$E = \theta_d - \theta \tag{6.11}$$

$$\dot{E} = \dot{\theta_d} - \dot{\theta} \tag{6.12}$$

$$\ddot{E} = \ddot{\theta_d} - \ddot{\theta} \tag{6.13}$$

Therefore, Equation (6.10) is rewritten in the following Equation (6.14):

$$\ddot{E} + K_v\dot{E} + K_pE + K_i \int E\, dt = 0 \tag{6.14}$$

Where, K_p, K_v, and K_i control gains are positive definite matrices.

6.2.1 Simulation with modified Computed Torque control (mCTC)

For this nonlinear control implementation, robot mass was incorporated in the mass terms $M(\theta)$, centrifugal & Coriolis terms $V(\theta, \dot{\theta})$, and gravity terms $G(\theta)$. The same trajectories as the PID controller simulation were used. The control gains used for the simulation were found by trial and error and are as follows:

$$K_P = diag[1000 \quad 1500],$$

$$K_V = diag[10 \quad 10], \text{ and}$$

$$K_I = diag[10 \quad 10].$$

6.2.1.1 iTbot Vertical Configuration: Simultaneous Joint movements (mCTC)

The simulated results using the mCTC for both iTbot's joint movements (Joint-1 – range: +45° -45°, and Joint-2 – range: +90° -90°) can be seen in *Figure 6.14*, *Figure 6.15*, and *Figure 6.16*. The tracking performance of both joints' simultaneous movements can be seen in *Figure 6.14*. The first row shows the trajectory comparison (Given joint angles – red dotted line, Measured joint angles – solid blue line) for all joints. The second row shows the tracking error, and the third row shows the measured torque from the simulation. Here the maximum tracking error was less than 0.05° (0.06%), which proves that the tracking performance is excellent. *Figure 6.15* and *Figure 6.16* show the plots of the joints separately. Here, the given velocities (third row) are denoted with a red dotted line, and the measured trajectory from the simulation is shown with a solid blue line. Maximum joint torque (using robot mass only) for Joint-1 found to be -4.6 Nm and +4.6 Nm; for

Joint-2, the maximum joint torque is -1 Nm and +1 Nm. The positive and negative signs denoted the direction of the joint torques.

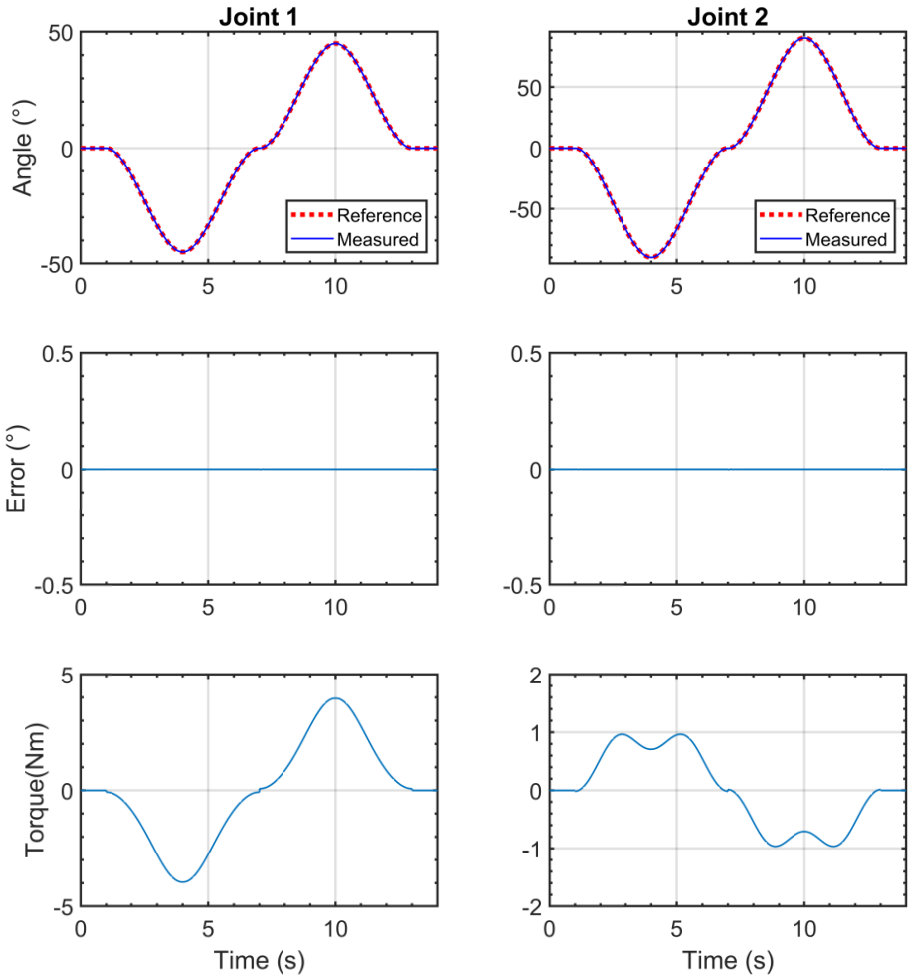

Figure 6.14 Simultaneous motion (mCTC) while iTbot is in vertical configuration

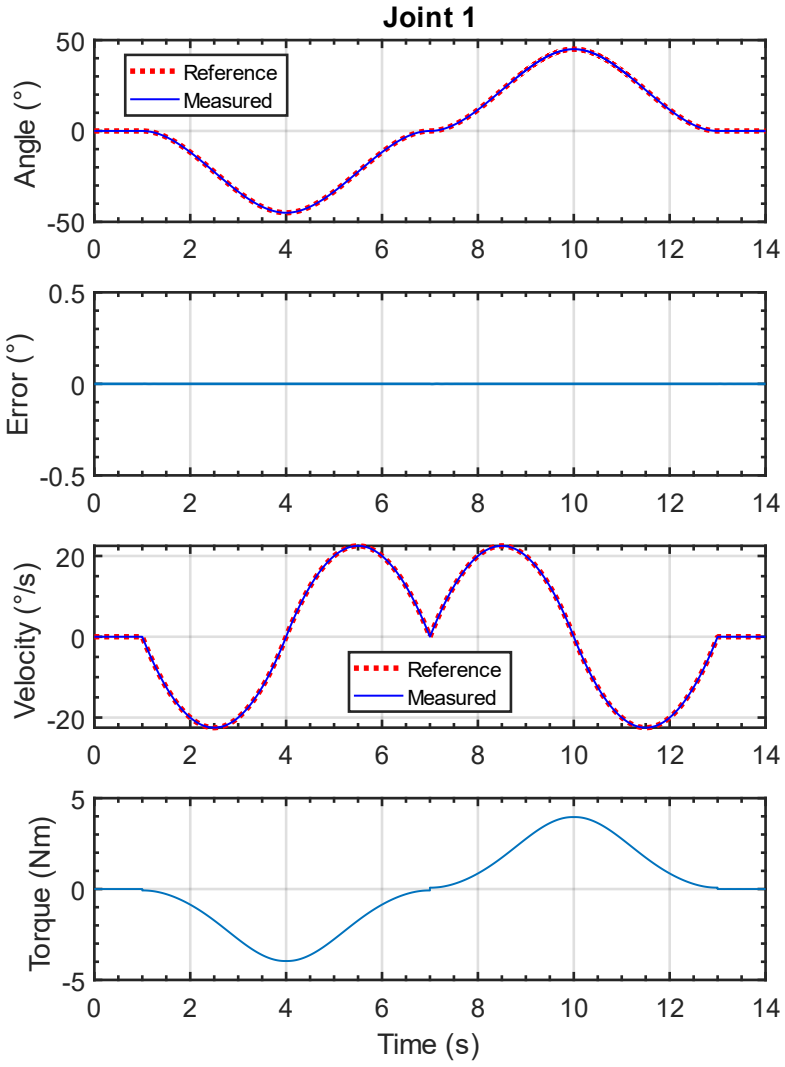

Figure 6.15 Both joints simultaneous movement (detail of Joint-1 movement with velocity comparison) (mCTC) while iTbot is in vertical configuration

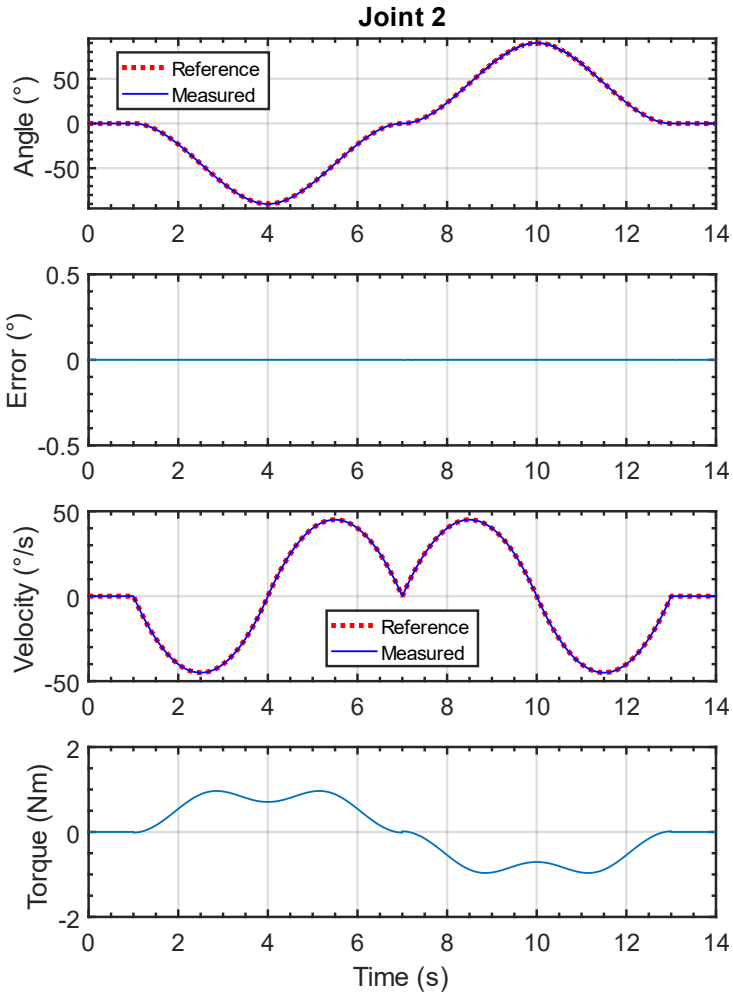

Figure 6.16 Both joints simultaneous movement (detail of Joint-2 movement with velocity comparison) (mCTC) while iTbot is in vertical configuration

6.2.1.2 iTbot Horizontal Configuration: Simultaneous Joint movements (mCTC)

Previously defined trajectories (*Figure 6.4*) have been simulated for this configuration, and the results can be seen in *Figure 6.17*, *Figure 6.18*, and *Figure 6.19*. The tracking performance of both joints' simultaneous movements can be seen in *Figure 6.17*. The first row shows the trajectory comparison (Given joint angles – red dotted line, Measured (simulated output) joint angles – solid blue line) for all joints. The second row shows the tracking error, and the third row shows the measured torque from the simulation. The tracking error was found to be almost zero, which proves that the tracking performance is excellent in this configuration. *Figure 6.18* and *Figure 6.19* show the plots of the joints separately. Here, the given velocities (third row) are denoted with a red dotted line, and the measured trajectory from the simulation is shown with a solid blue line. Joint torque (using robot mass only) for Joint-1, found to be +0.17 and -0.1,76 Nm, and for Joint 2, the torque values are +0.03 Nm and -0.03 Nm . It is to be noted that, same as simulation with PID in iTbot's horizontal configuration, the torque generated is lower than iTbot's vertical configuration as there is no gravitational effect on either Joint 1 or Joint 2.

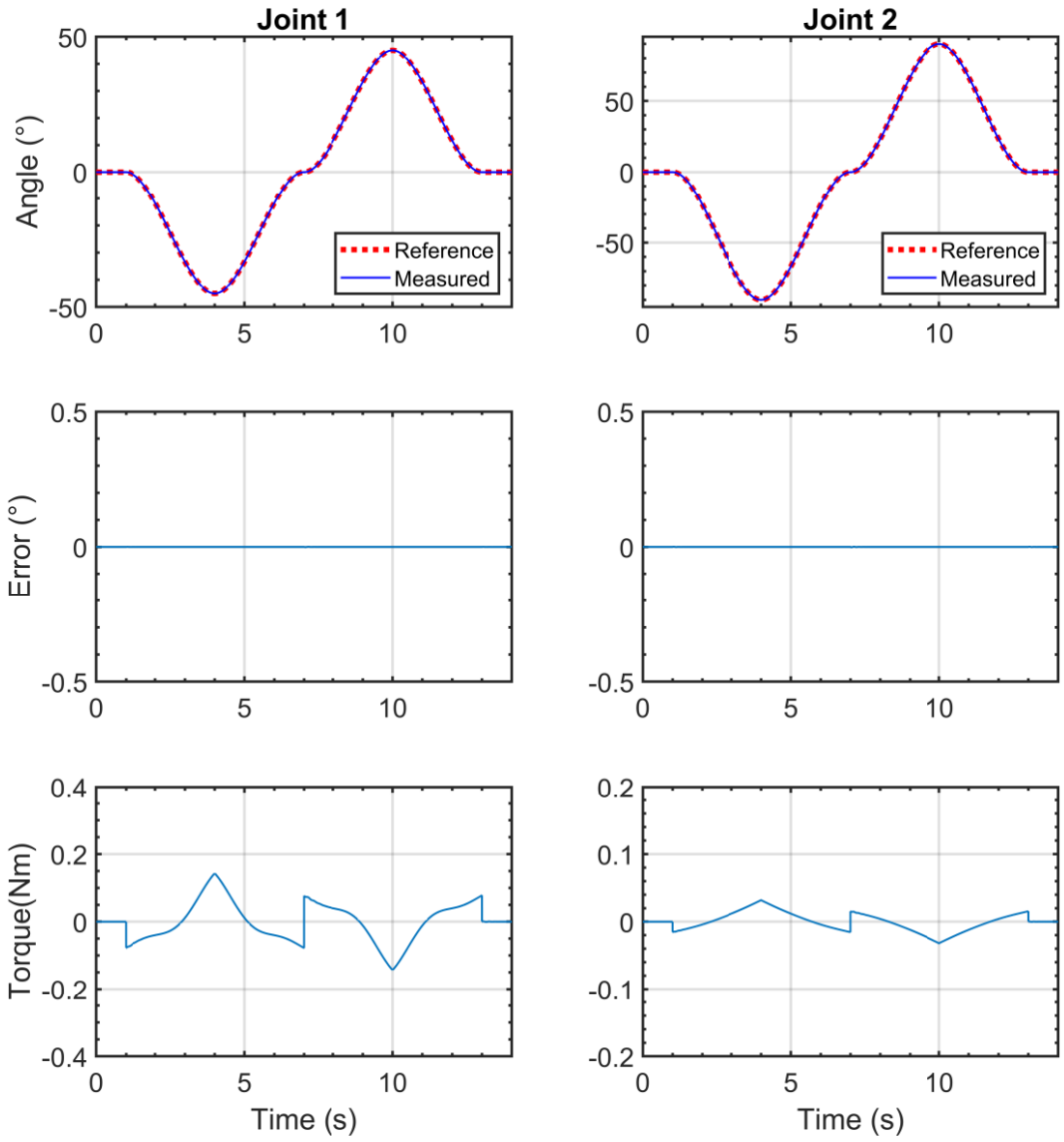

Figure 6.17 Simultaneous motion (mCTC) while iTbot is in horizontal configuration

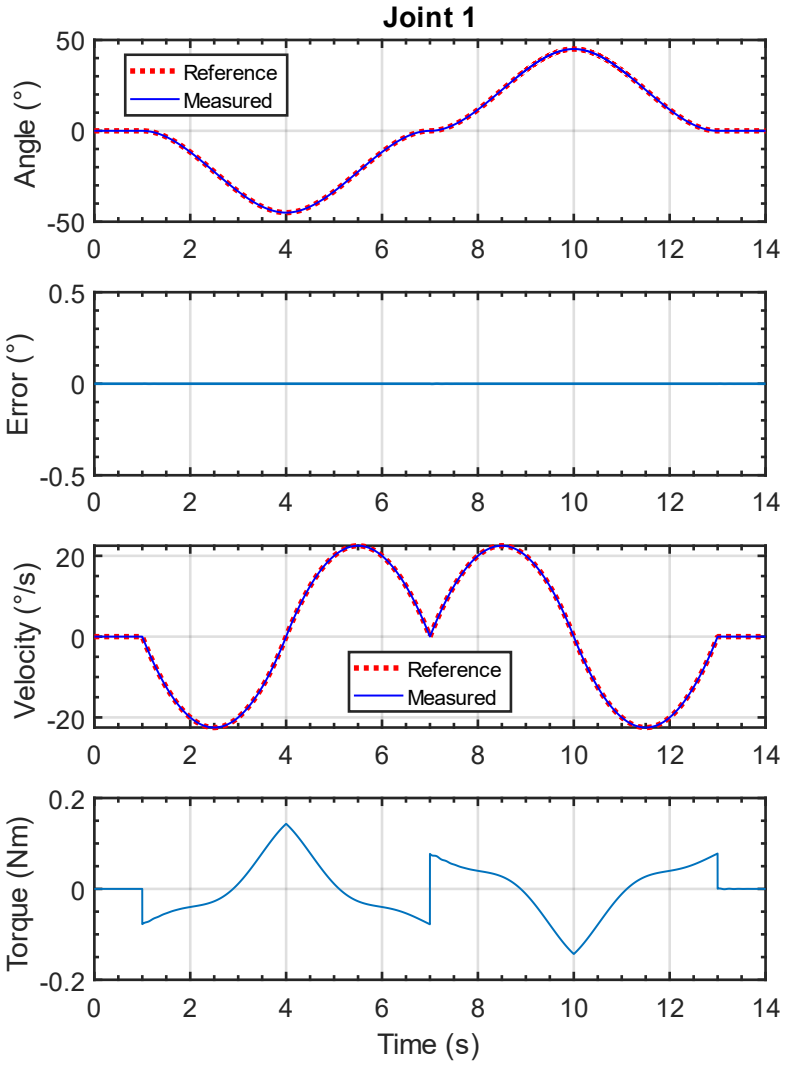

Figure 6.18 Both joints simultaneous movement (detail of Joint-1 movement with velocity comparison) (mCTC) while iTbot is in horizontal configuration

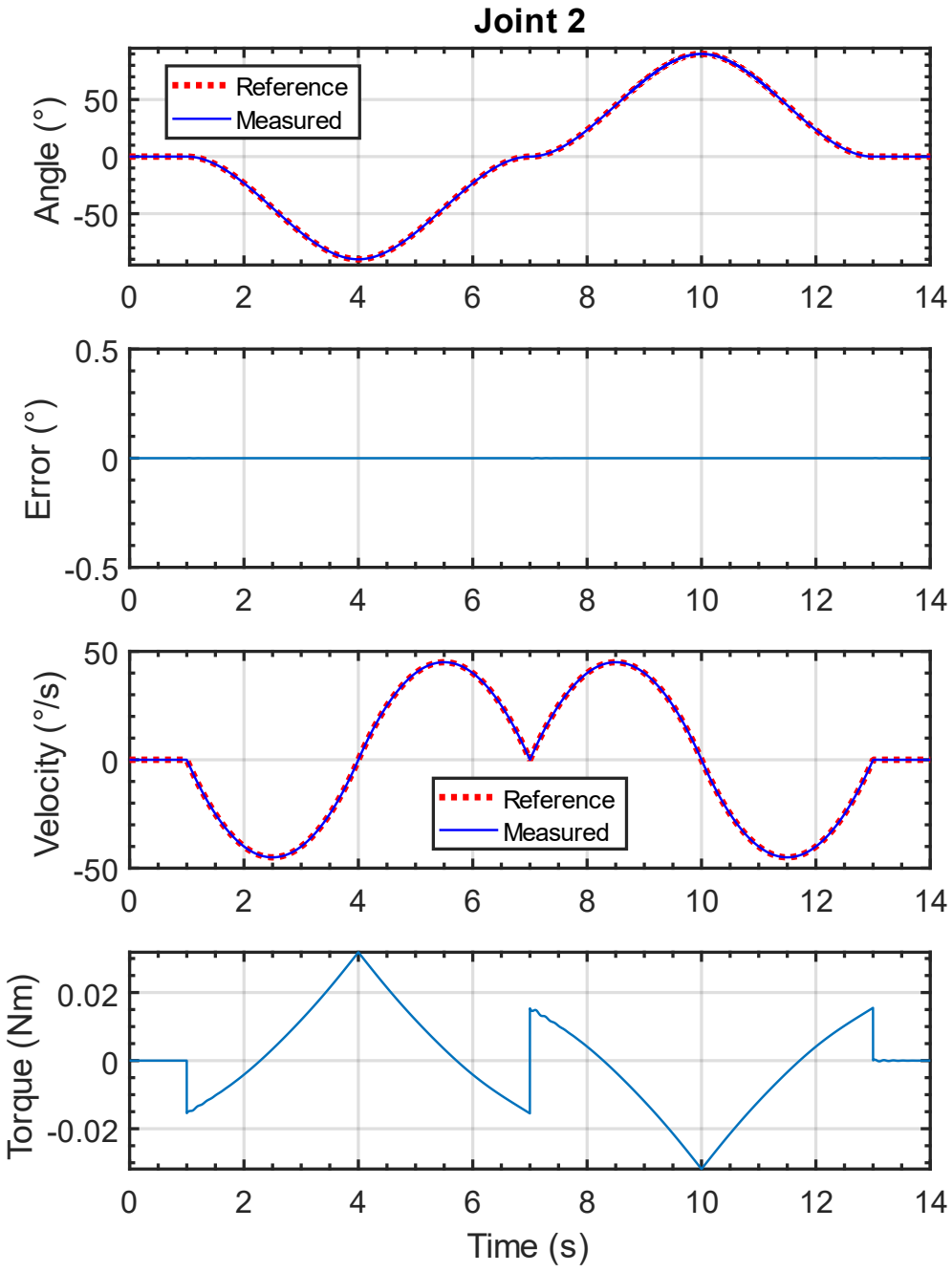

Figure 6.19 Both joints simultaneous movement (detail of Joint-2 movement with velocity comparison) (mCTC) while iTbot is in horizontal configuration

6.3 Sliding Mode Control based on Innovative Reaching Law (SMiRL)

The second model-based controller used in iTbot is a newly proposed controller based on Sliding Mode Control (SMC) with an innovative Reaching Law is used. The theory of SMC in a nonlinear system is well known [103]; a brief description of its application on iTbot, its shortcomings, and the reasoning behind choosing the novel innovative Reaching Law over other current Reaching Laws are discussed.

The dynamic model of the designed end-effector 2-DOfs exoskeleton manipulator is given by the following equation:

$$M(q)q + C(q,\dot{q})\ddot{q} + f_{dis} = \tau \tag{6.15}$$

Where $q\epsilon\mathbb{R}^2$ denotes the generalized coordinates vector. $M(q) \in \mathbb{R}^{2\times2}$, $C(q,\dot{q})\dot{q} \in \mathbb{R}^2$, and $G(q) \in \mathbb{R}^2$are respectively the symmetric, bounded, inertia matrix, the Coriolis and centrifugal torques, and the gravitational torques. $\tau \in \mathbb{R}^2$ is the torque input vector and $f_{dis} \in \mathbb{R}^2$ represents the uncertainties and external disturbance.

Assuming that $q = x$ and $q_d = x^d$, the robot's dynamics (6.15) can be rewritten in accordance with the general form of nonlinear systems:

$$\ddot{x} = f(x,\dot{x}) + g(x)u + \omega(x,\dot{x}) \tag{6.16}$$

where, $g(x) = M^{-1}(q)$, $u = \tau$, f $(x,\dot{x}) = M^{-1}(q)\big(C(q,\dot{q})q + G(q)\big)$, and $w(x,\dot{x}) = M^{-1}(q)f_{dis}$. The tracking position error, which tends to zero, can be defined as: $e = x - x^d$,where $x, x^d \in \mathbb{R}^2$ is the desired trajectory. Selecting a switching function *S* to track position

and velocity errors is often one of the first steps in designing SMC controllers. Commonly, this sliding surface is chosen as follows:

$$S = \dot{e} + \lambda e \tag{6.17}$$

Where $\lambda \in \mathbb{R}^{2\times 2}$ is a diagonal positive matrix. It is worth mentioning that the value of λ plays a crucial role in the error tracking convergence rate to zero.

Now considering the Lyapunov function: $V(S) = \frac{1}{2}S^T S$, we can find its time derivative,

$$\dot{V} = S^T \dot{S} \tag{6.18}$$

The criterion for stability is therefore $\dot{V} < 0$. This requires $\dot{S}^T S < 0$, which results in the known control law switching phenomenon around $S = 0$.

Based on the derivative of (6.19) we can propose the control law as

$$\mathrm{u} = g^{-1}[\ddot{x}^d - \lambda\dot{e} - \mathrm{f} - \omega + \dot{S}] \tag{6.19}$$

It is noteworthy, from (6.19), that the control input is highly dependent on $\dot{S}$, which in turn determines the rate of S. That is, if $\dot{S} \ll 0$ for $S > 0$ (with the opposite being also true), the system's forced trajectory converges to $S = 0$. Hence, commonly referring to $\dot{S}$ as the "reaching law". When system's trajectory is in the vicinity of $S = 0$, with $\dot{V} < 0$, $\dot{S} < 0$ dictates how close is the system exactly from the sliding manifold $S = 0$. Consequently, a "switching" phenomenon emerges in order to maintain the condition: $\dot{S}^T S < 0$.

Remark 1.: The control law defined by (6.19) is inputted to system (6.16) if it is unperturbed, i.e. for a given known $\omega(x, \dot{x})$. However, in real-time, system (6.16) will be subject to uncertainties and external disturbances. In such a case, an estimation of $\omega(x)$. will be integrated into control law (6.19) in the next sections.

In fact, all reaching laws have proven to be highly helpful and applicable in designing SMCs [104]. Yet, adopting any of these reaching laws seems to come with an inevitable trade-off between the convergence rate and chattering reduction or the chattering reduction and controller's robustness. One common behavior between these laws is that the choice of a large gain value K_{1i} (coefficient of $sign(S_i)$), is required to ensure a fast convergence rate to the desired surface. However, this, in turn, results in increased chattering, a significantly damaging problem due to the generated high-frequency control signals. As a result, an adaptive reaching law, the Exponential Reaching Law (ERL), has been proposed [105] to deal with the gain values. This ERL is given by (6.20):

$$\dot{S}_i = -\frac{K_{1i}}{\mu_i + (1-\mu_i)e^{-\alpha_i |S_i|^{P_i}}} sign(S_i) \tag{6.20}$$

where,

μ_i and P_i are strictly positive constants, with $\mu_i < 1$. As a consequence of (6.20), the limitation related to the gain value can be easily overcome with the controller dynamically self-adjusting to the variations resulting from the switching function S_i. This operation permits the gain K_{1i} to smoothly vary between K_{1i} and K_{1i}/μ_i.

Indeed, the ERL focuses primarily on reducing chattering using the innovative law defined by (6.20). However, completely eliminating this chattering effect remains questionable, especially

when the term $K_{1i}sign(S_i)$ is conserved, thus putting restrictions on improving the chattering. It is almost impossible to increase the convergence speed without causing chattering attenuation. That is, any decrease in the reaching time drives the term K_{1i} higher, which again causes the chattering phenomenon. It was further noticed that the state of the control system does not perfectly overlap with the reference trajectory due to the continuous low chattering degree.

6.3.1 Proposed Control System – Sliding Mode Control based on Innovative Reaching Law (SMiRL):

This section presents the mathematical formulation of the proposed reach- ing law that would make use of ERL's advantages, in addition to ensuring a convergence time less than that provided by ERL. The proposed reaching law is given by:

$$\dot{S}_i = -\frac{K_{1i}}{\mu_i + (1-\mu_i)e^{-\alpha_i|S_i|^{P_i}}}|S_i|^{\gamma}sign(S_i) - \rho_i \frac{K_{1i}(1-\gamma)}{\mu_i}sign(S_i) \quad (6.21)$$

where μ_i, α_i, and P_i are strictly positive constants with $\mu_i < 1$ and $0 < \gamma < 0.5$. ρ_i is determined by $\lim_{t\to\infty}\rho_i = 0$, and $\int_0^t \rho_i(w)dw = Q_i < \infty$, where $\rho_i = 1/(1 + t^i)$ and t^i is the time execution of the exercise. In fact, the second term of the proposed law (6.21) is to conserve the control input robustness, especially at the start of the trajectory. As time progresses, this term would vanish due to the definition of ρ_i.

In the preceding section, the advantages of each term, such as ERL and power rate, were briefly explained. It was noticed that the term γ is usually assigned a high value in the conventional power rate law to ensure fast convergence to the equilibrium point, however resulting with undesirable

chattering. In efforts of improving this, in the proposed law, a limit on γ was enforced such that: 0 < γ < 0.5. This would not only ensure fast convergence, but also minimize the chattering.

6.3.2 Simulation using SMiRL:

The simulations for iTbot with SMiRL has been done in SIMULINK software. For this nonlinear control implementation, the iTRob's mass and inertia tensor were incorporated in the mass terms $M(\theta)$, centrifugal & Coriolis terms $V(\theta, \dot{\theta})$, and gravity terms $G(\theta)$. The same trajectories as other simulations were used. The control gains used for the simulation were found by trial and error and are as follows:

$$K_{1i} = diag[9.5 \quad 9.5],$$

$$\lambda = diag[10 \quad 10], \text{ and}$$

$$\mu_1 = \mu_2 = 0.6$$

$$\alpha_1 = \alpha_2 = 20$$

$$P_1 = P_2 = 15$$

$$\gamma = 0.5$$

6.3.2.1 iTbot Vertical Configuration: Simultaneous Joint movements (SMiRL)

The simulated results using the SMiRL for both iTbot's joint movements (Joint-1 – range: -45° +45°, and Joint-2 – range: -90° +90°) can be seen in *Figure 6.20*, *Figure 6.21*, and *Figure 6.22*. The tracking performance of both joints' simultaneous movements can be seen in *Figure 6.20*. Here the maximum tracking error was less than 0.01° (0.006%), which proves that the tracking

performance is excellent. *Figure 6.21* and *Figure 6.22* show the plots of the joints separately. Here, the given velocities (third row) are denoted with a red dotted line, and the measured trajectory from the simulation is shown with a solid blue line. Maximum joint torque (using robot mass only) for Joint-1 found to be -4.1 Nm and +4.1 Nm; for Joint-2, the maximum joint torque is -1.1 Nm and +1.1 Nm. The positive and negative signs denoted the direction of the joint torques.

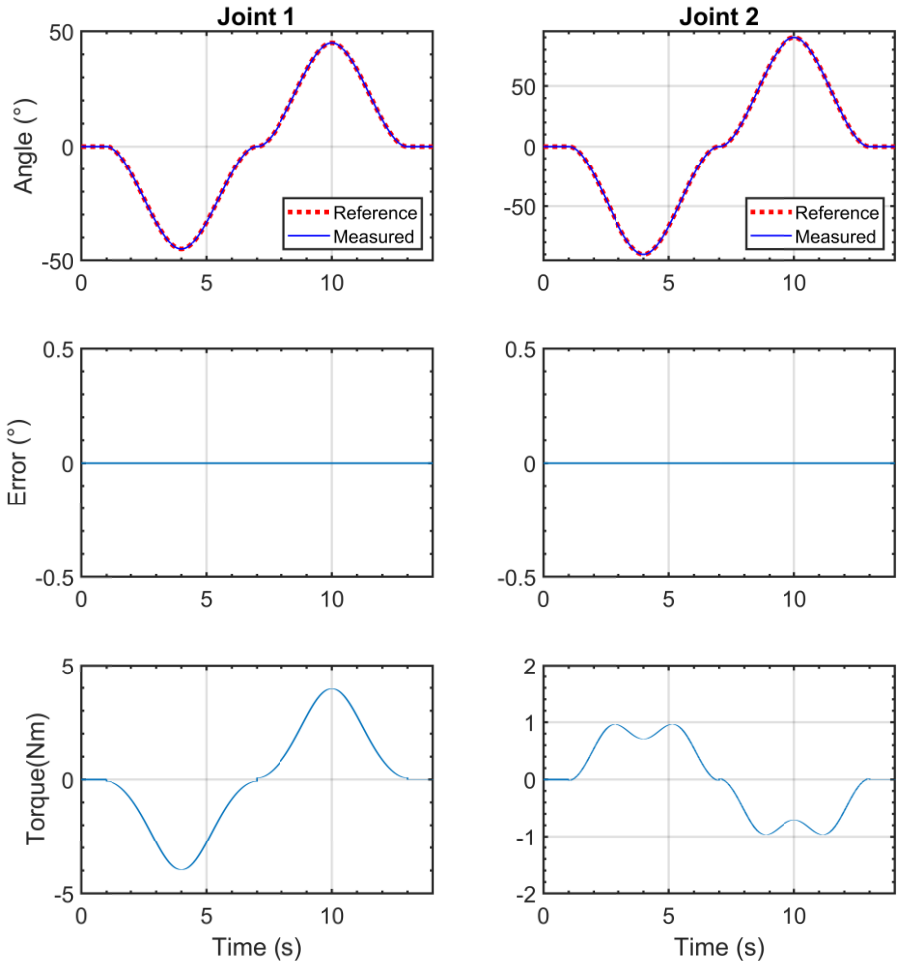

Figure 6.20 Simultaneous motion (SMiRL) while iTbot is in vertical configuration

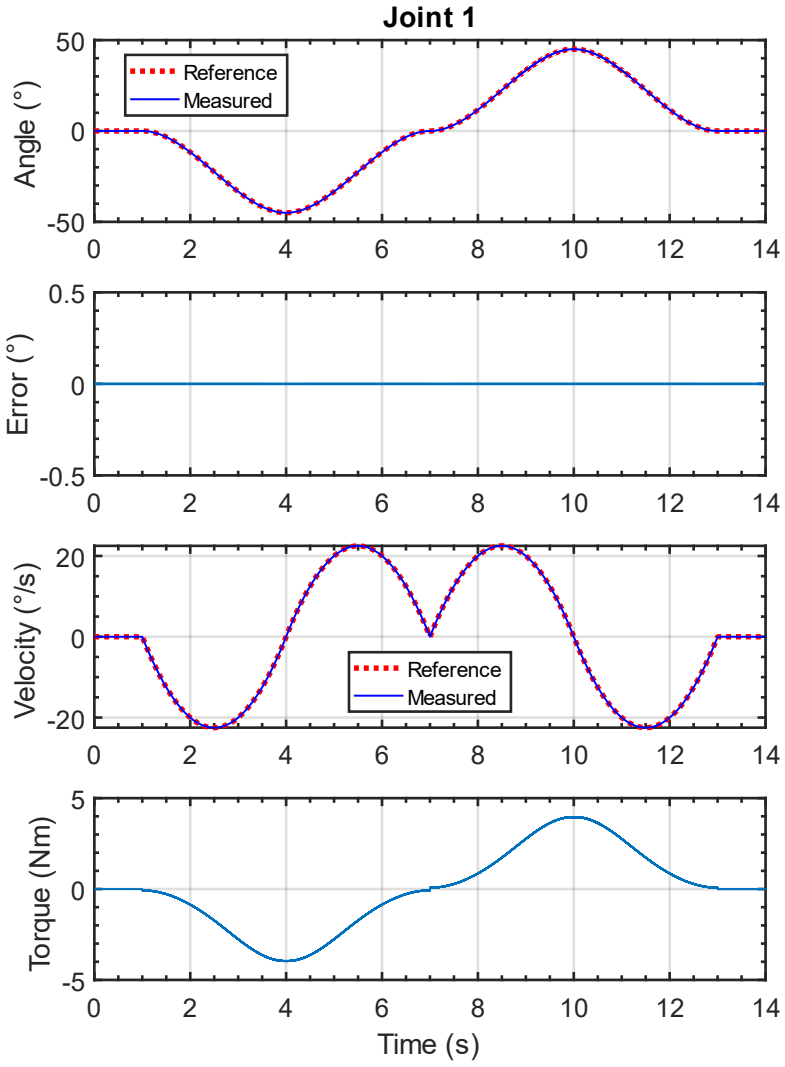

Figure 6.21 Both joints simultaneous movement (detail of Joint-1 movement with velocity comparison) (SMiRL) while iTbot is in vertical configuration

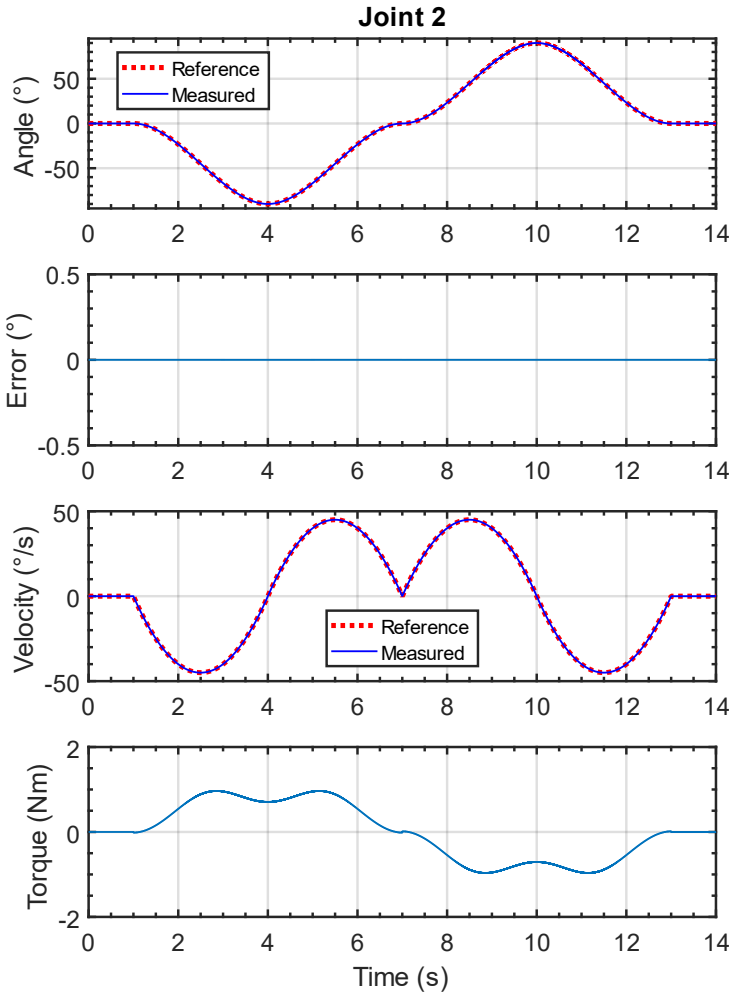

Figure 6.22 Both joints simultaneous movement (detail of Joint-2 movement with velocity comparison) (SMiRL) while iTbot is in vertical configuration

6.3.2.2 iTbot Horizontal Configuration: Simultaneous Joint movements (SMiRL)

Previously defined trajectories have been simulated for this configuration, and the results can be seen in *Figure 6.23*, *Figure 6.24*, and *Figure 6.25*. The tracking performance of both joints'

simultaneous movements can be seen in *Figure 6.23*. The tracking error was found to be almost zero, which proves that the tracking performance is excellent in this configuration. Although some high control action can be seen in Joint 1, this is due to the setting of gain parameters that can be alleviated during experimentation.

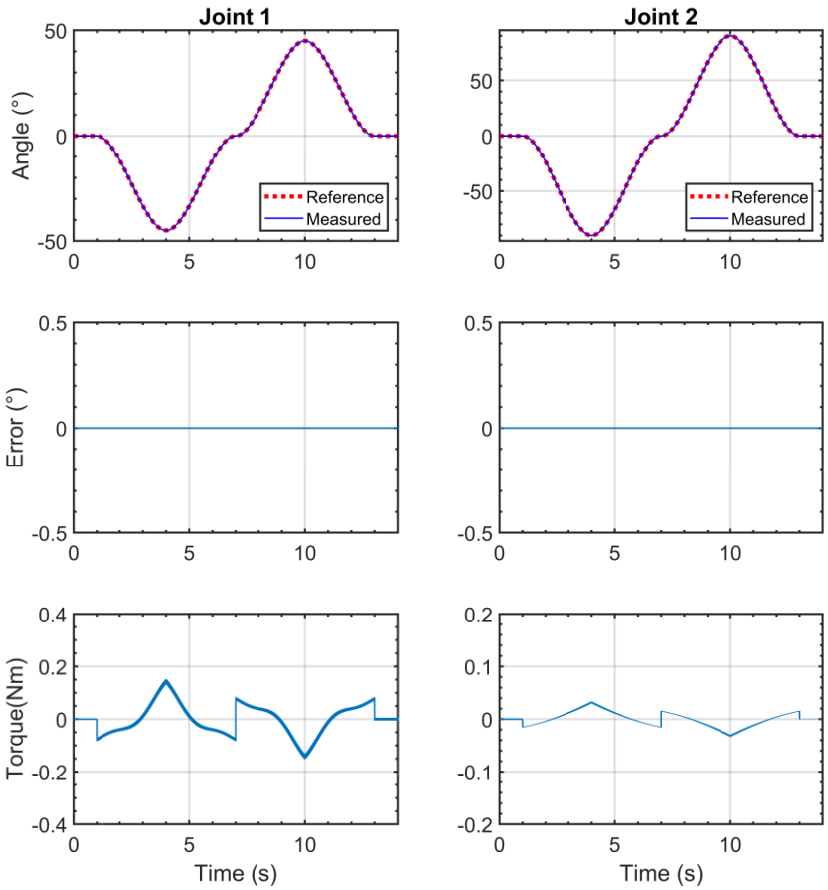

Figure 6.23 Simultaneous motion (SMiRL) while iTbot is in horizontal configuration

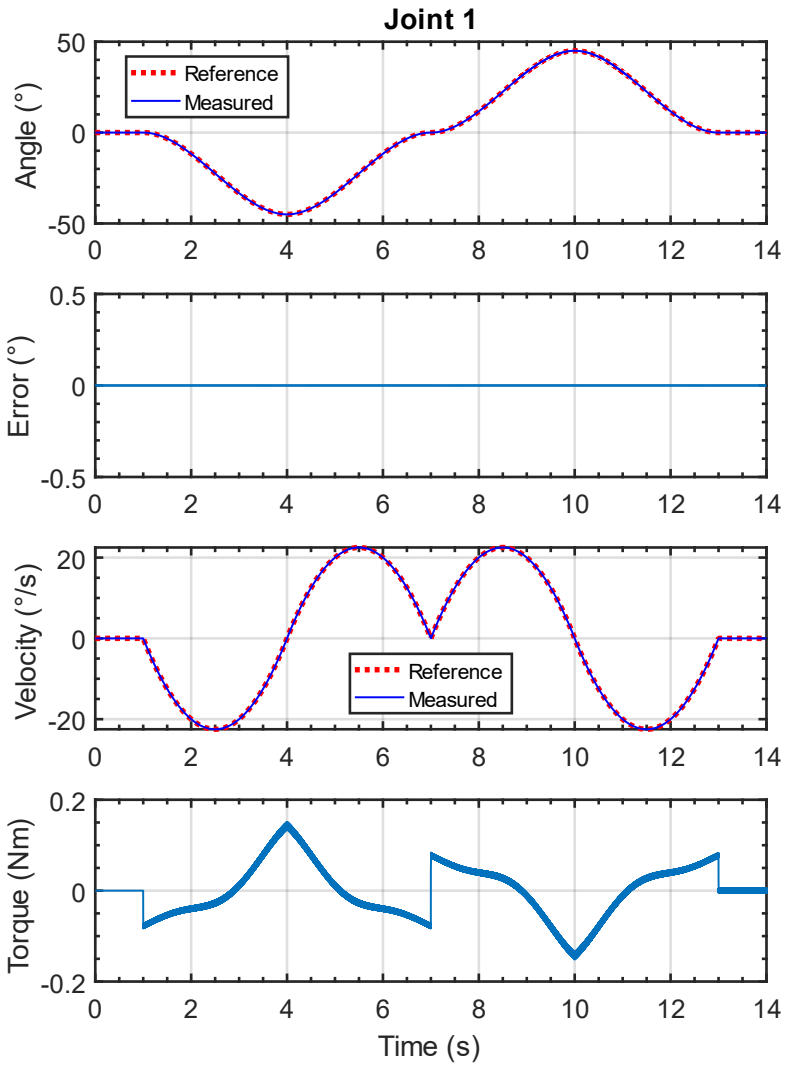

Figure 6.24 Both joints simultaneous movement (detail of Joint-1 movement with velocity comparison) (SMiRL) while iTbot is in horizontal configuration

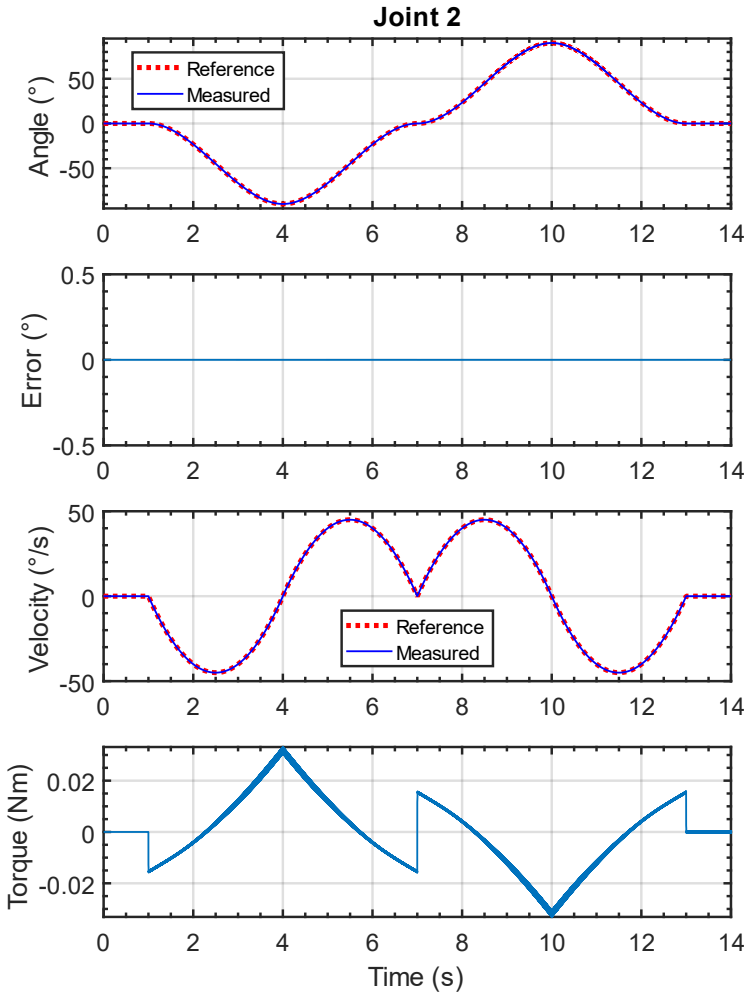

Figure 6.25 Both joints simultaneous movement (detail of Joint-2 movement with velocity comparison) (SMiRL) while iTbot is in horizontal configuration

6.4 Admittance-based Active and Active-assistive Movements [106]

The robot's active or active-assistive mode helps the user based on feedback received by a force sensor mounted on the robot's end-effector. To do this, the assistive controller partially modifies the robot's trajectory in relation to the force sensor input. The first step is to transform the force

sensor input to the corresponding torques exerted on the robot's two joints. From geometric solution of the 2 DoF robot iTbot, the joint torques resulting from the X and Y component of the forces exerted on the end effector can be expressed by:

$$\tau_1 = -l_1 sin\theta_2 F_x + (l_2 - l_1 cos\theta_2) F_y \tag{6.22}$$

$$\tau_2 = l_2 F_y$$

Where,

$l_1 and\ l_2$ are the link lengths

$F_x\ and\ F_y$ are the x and y components of the force

$\theta_1\ and\ \theta_2$ are the joint angles

$\tau_1\ and\ \tau_2$ are the joint torques generated by the force

Knowing the result from (6.17) and applying the impedance definition in the form of an admittance relation, we have a direct form with which to modify the desired trajectory as follows:

$$q_a = q_d + \tau \left(\frac{1}{K + C_s}\right) \tag{6.23}$$

Where, q_a is the $2x1$ vector of the new desired trajectory defined by the admittance, q_d is the $2x1$ vector with the original desired trajectory from the trajectory planner. K and C are the gain matrices corresponding to a spring and damper constant, respectively. Adjusting these constants provide higher or lower resistance to subject's movements using the force inputs.

CHAPTER 7

EXPERIMENTS AND RESULTS

This chapter covers the experimentation of iTbot with healthy human subjects to demonstrate the use of robot-aided rehabilitation based on principles of motor rehabilitation discussed in Chapter 3. The beginning of this chapter describes the experimental setup with the integration of the controller(s) to the iTbot robot, along with verification of simulation results. After that, the iTbot was used to perform various passive, active, and active-assisted rehabilitation exercises, each set of exercises focusing on a specific set of motor rehabilitation principles. Quantitative measures of the robot's effectiveness to perform such exercises are evaluated by measuring tracking errors for passive exercises; observing the user's effectiveness of performing goal-oriented active and active-assisted exercises of varying difficulty. Furthermore, the force sensor input and electromyogram (EMG) data for the user's muscle activation is recorded along with the robot's position tracking data to quantitively track the user's improvement of performing active exercises over time. The chapter ends with a brief discussion on the experimental results.

7.1 Experimental Setup and Control Implementation

The experimental setup for the iTbot system consists of the robot and its control system set up in a desktop configuration. The robot was configured for vertical configuration for right-handed and left-handed use, as well as horizontal configuration for parts of the experiment depicted in *Figure 7.1*. During active exercise, the user's muscle activation data is logged using the Delsys Trigno series EMG electrodes, as shown in *Figure 7.2*.

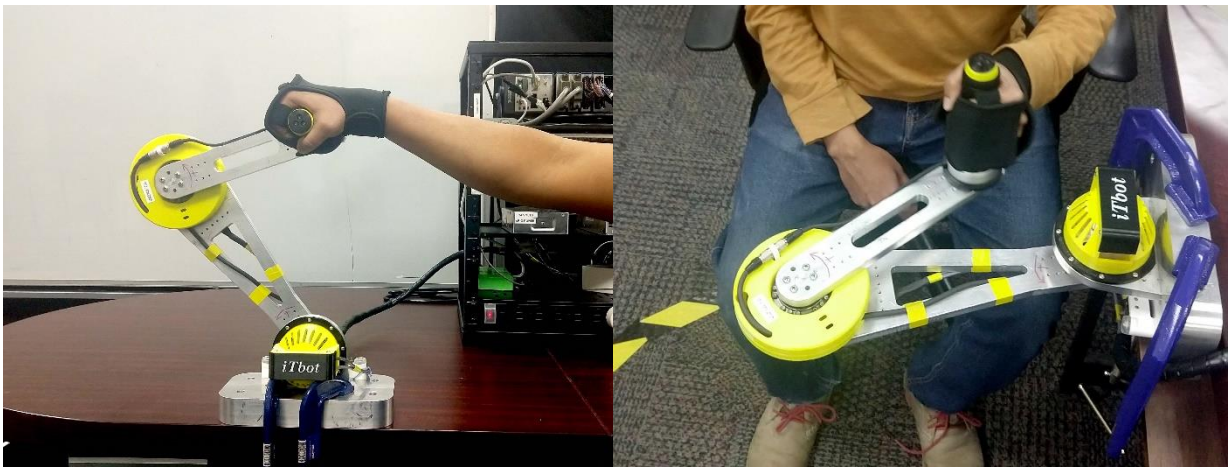

Figure 7.1 Vertical (left) and Horizontal (right) configuration of the robot

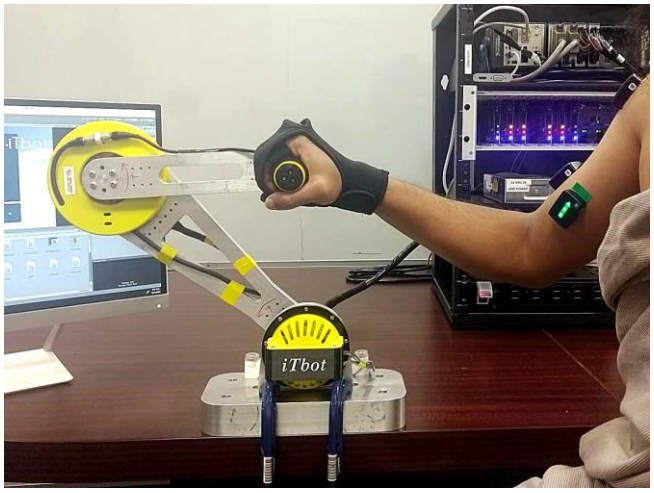

Figure 7.2 Active exercise with EMG data acquisition

Figure 7.3 shows the location of EMG electrodes per channel on a subject's body. The list of muscles recorded by each channel of EMG are as follows:

Ch.1: Deltoid (anterior part)

Ch.2: Deltoid (posterior part)

Ch.3: Pectoralis major (clavicular part)

Ch.4: Biceps (proximal part)

Ch.5: Biceps (lateral part)

Ch.6: Triceps (lateral part)

Ch.7: Triceps (proximal part)

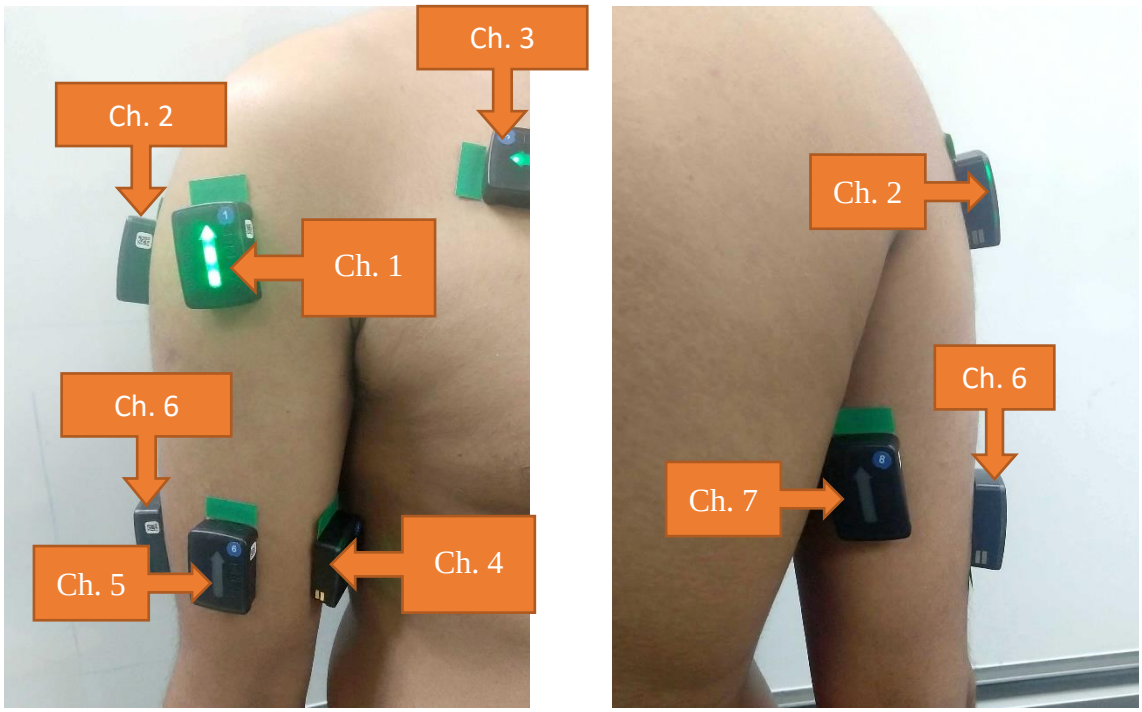

Figure 7.3 Location of the EMG electrodes on Subject-A's upper arm (Left: Front view, Right: View from behind)

During initial testing, a joint-based trajectory was used to test the performance of the three control algorithms used in the iTbot robot (i.e., PID, mCTC, and SMiRL). The trajectory is an estimated motion therapy to stimulate the user's elbow flexion-extension motion. However, it is later observed that in an end-effector type robot, like the iTbot, where the user's arm is not constrained, this trajectory results in multi-joints (i.e., shoulder, elbow, and wrist joints) motion of the arm. In this trajectory, Joint-1 of the robot moves 8 degrees in a positive direction in 3 seconds, while

Joint-2 moves 80 degrees in the positive direction at the same time. This trajectory is shown in *Figure 7.4*.

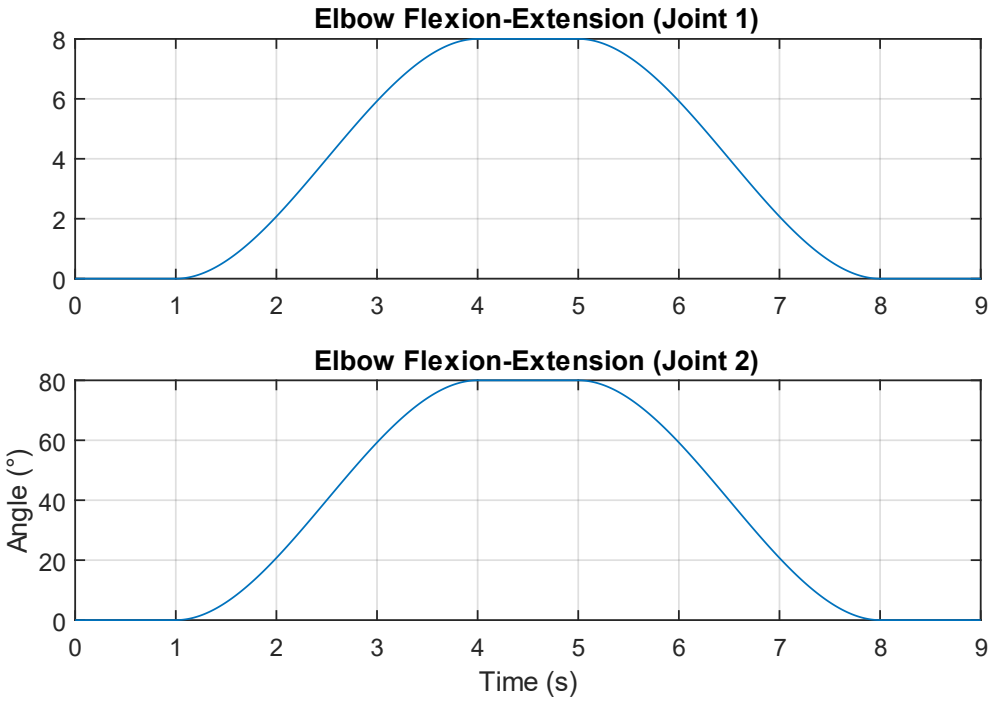

Figure 7.4 Generated trajectory for Elbow Flexion-Extension exercise

For the exercise in vertical mode, test subject-A (age: 28 years; height: 5ft 4 in; Weight: 125 lbs.) attached their right upper limb with the robot as shown in *Figure 7.5*. The exercise trajectory is run 3 times, with 3 different controllers (i.e. PID, mCTC, and SMiRL) with the following gains for Joint-1, 2 respectively:

PID Gains: Kp = 600, 320
Kv = 70, 90
Ki = 6, 3

mCTC Gains: Kp = 12000, 21000

Kv = 80, 40

Ki = 15, 7

SMiRL Gains: Lambda = 75, 400

K = 25, 25

Delta = 0.3, 0.1

Alpha = -800, -15

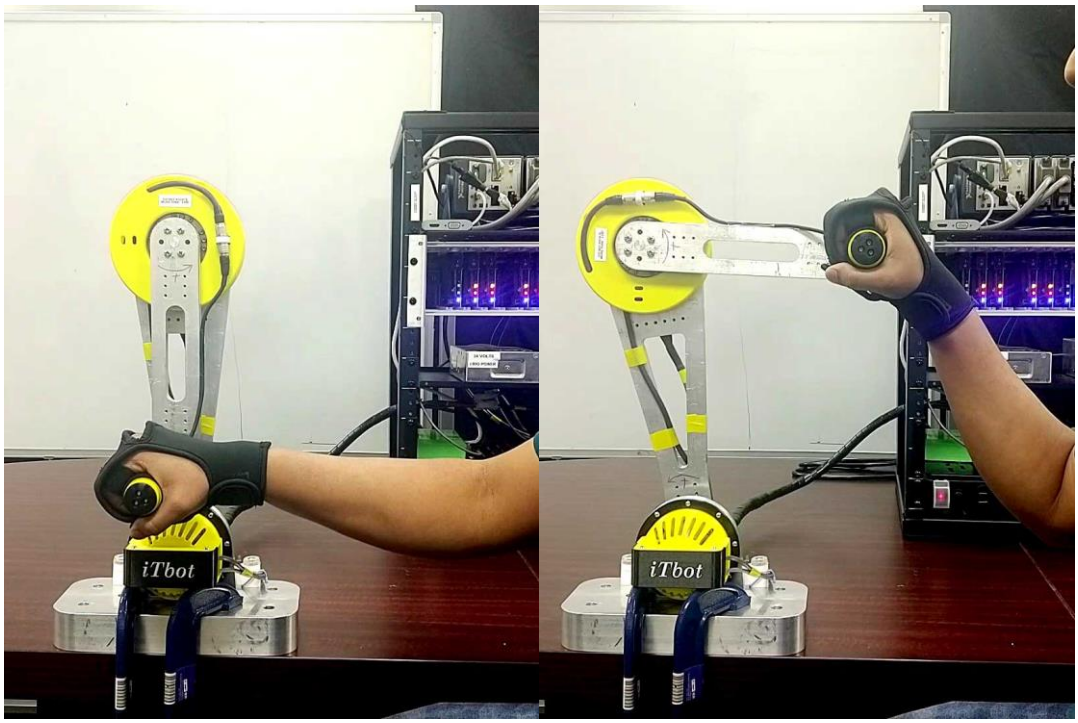

Figure 7.5 Elbow Flexion-Extension exercise using three different controllers

The results with joint angles, velocity, motor current, and tracking errors for both Joint-1 and Joint-2 are plotted in figures, *Figure 7.6*, *Figure 7.7*, and *Figure 7.8*

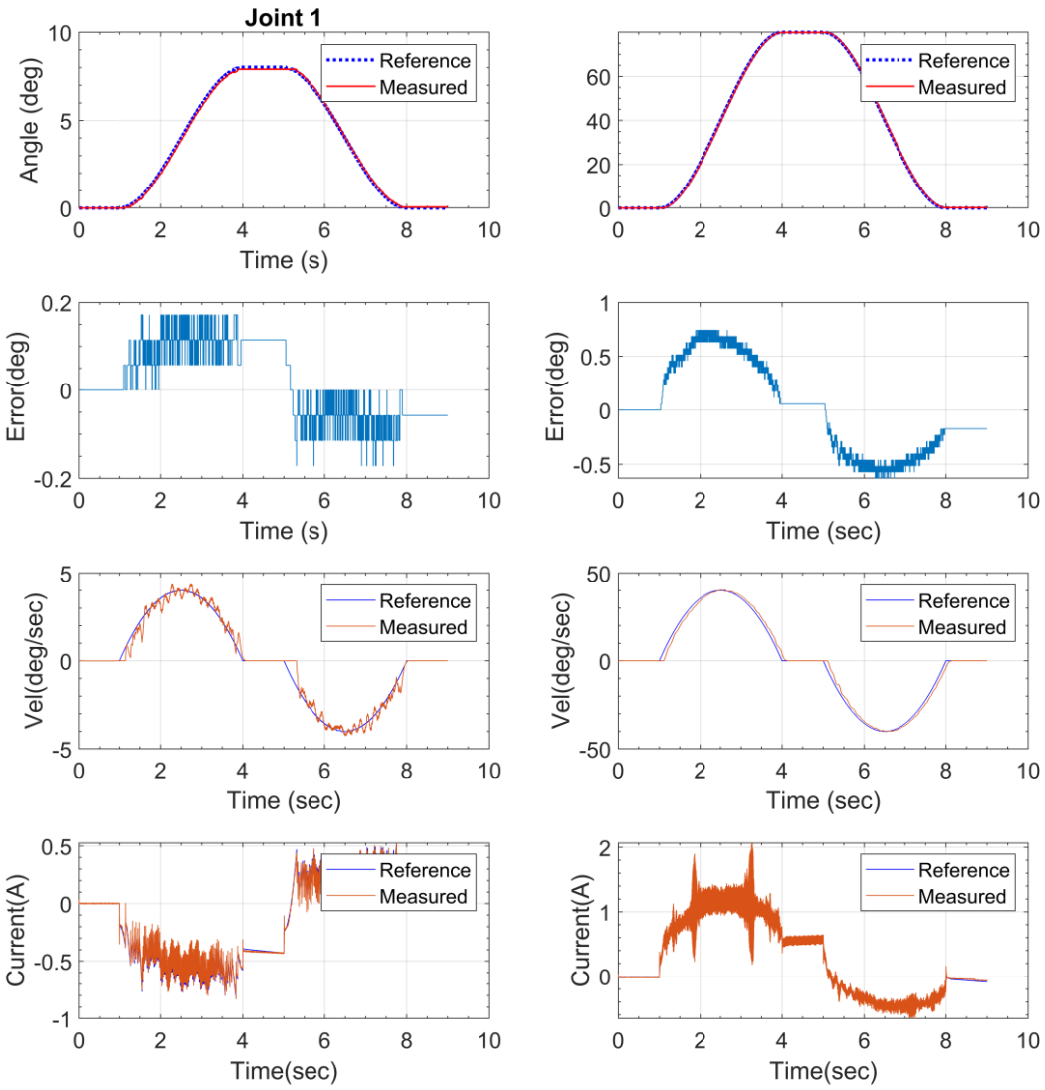

Figure 7.6 Elbow Flexion-Extension exercise using PID controller in vertical orientation of the robot

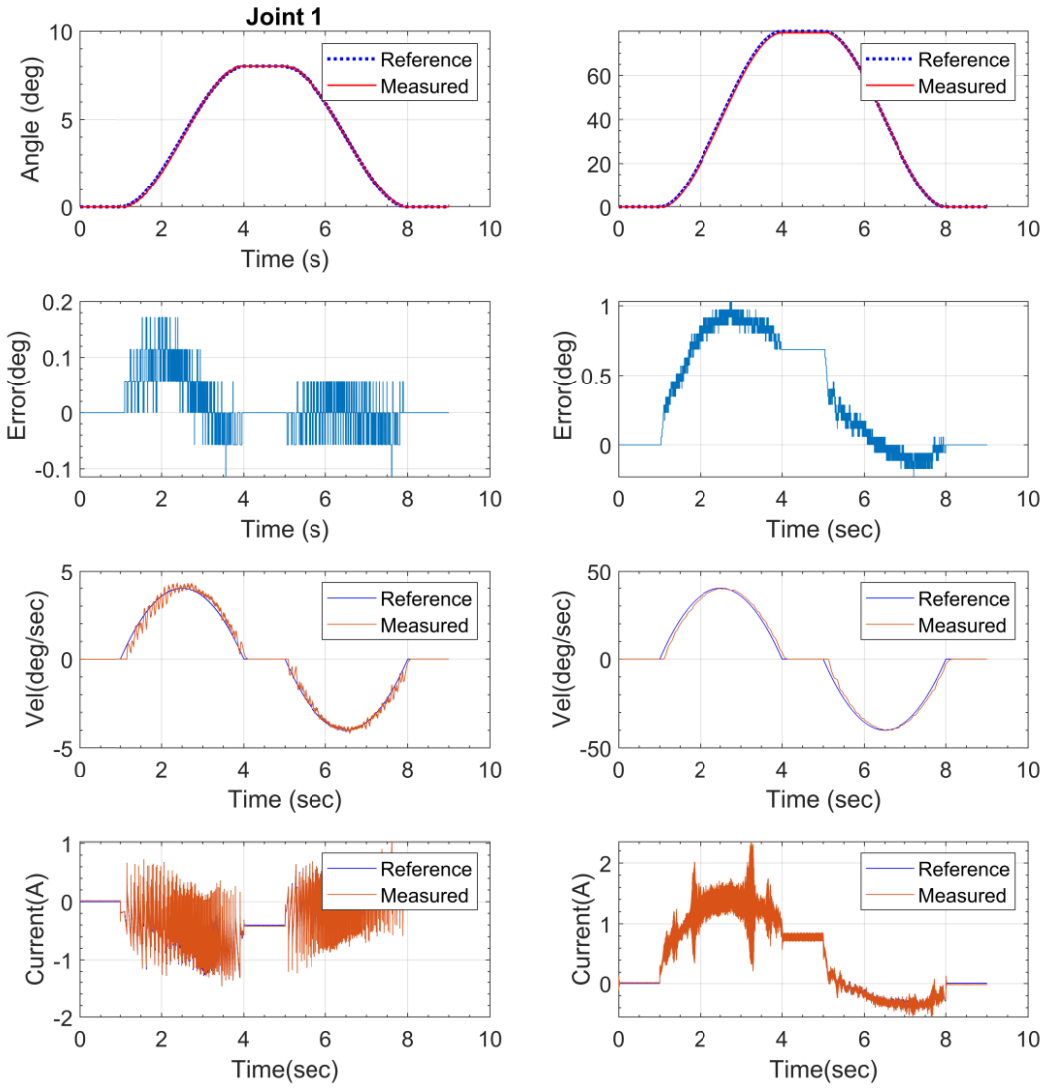

Figure 7.7 Elbow Flexion-Extension exercise using mCTC controller in vertical orientation of the robot

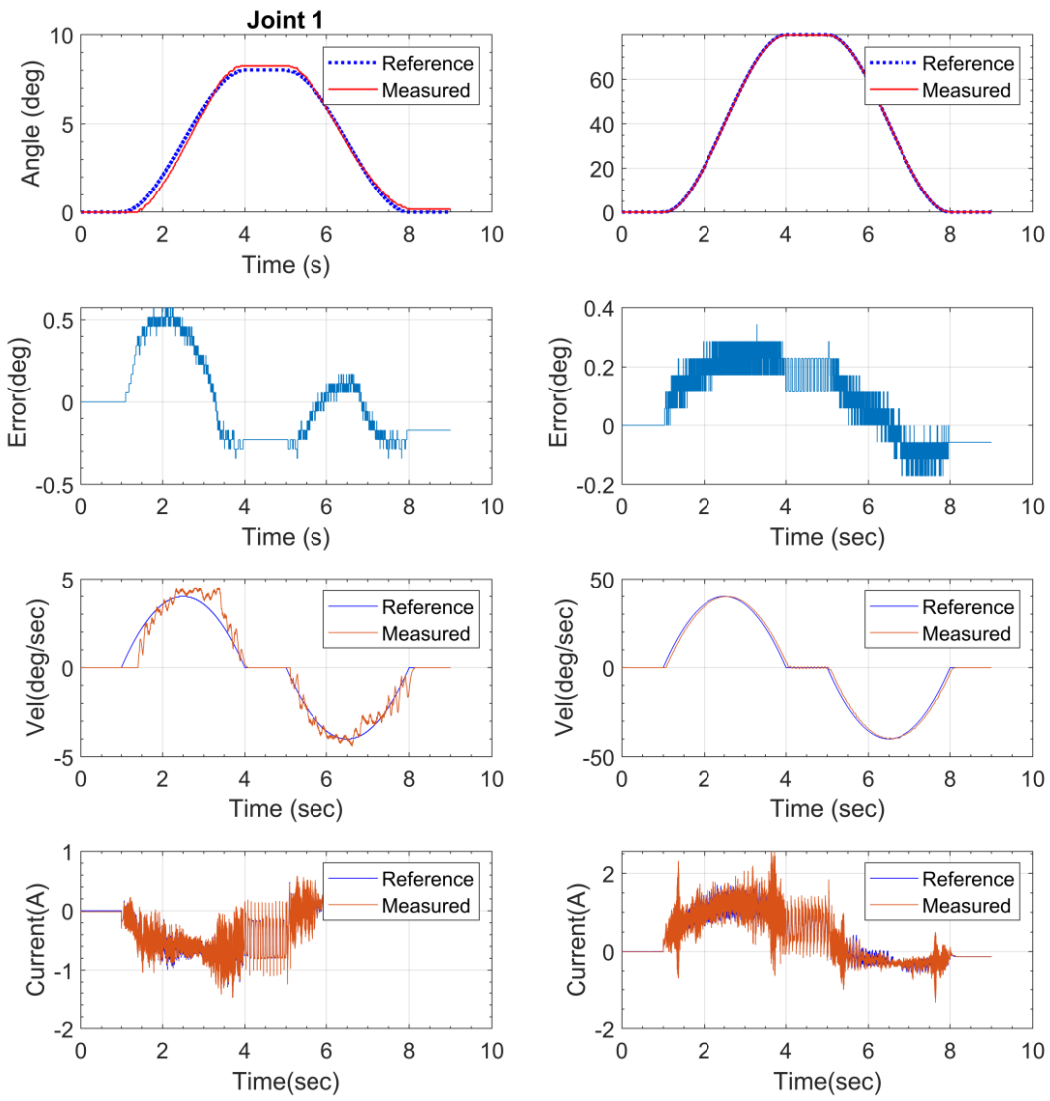

Figure 7.8 Elbow Flexion-Extension exercise using SMiRL controller in vertical orientation of the robot

From the above results, we can see that although all three controllers are capable of running the robot at decently low tracking error, all three of them show some amount of chattering at the gains used. This chattering can be further reduced by extended tuning of the gain parameters for each controller.

For the exercise in horizontal mode, test subject-B (age: 29 years; height: 5ft 1in; Weight: 115 lbs.) attached their right upper limb with the robot as shown in *Figure 7.1* (Right). A mirrored version of vertical mode trajectory, which is now working as an estimated motion for shoulder internal-external rotation, is run three times, with three different controllers (i.e., PID, mCTC, and SMiRL) with the same gains for Joint-1, and Joint-2 respectively:

PID Gains: Kp = 600, 320
Kv = 70, 90
Ki = 6, 3

mCTC Gains: Kp = 12000, 21000
Kv = 80, 40
Ki = 15, 7

SMiRL Gains: Lambda = 75, 400
K = 25, 25
Delta = 0.3, 0.1
Alpha = -800, -15

The results with position (joint angles), velocity, motor current, and tracking errors for both Joint-1 and Joint-2 in the horizontal position are plotted in figures, *Figure 7.9*, *Figure 7.10*, and *Figure 7.11*.

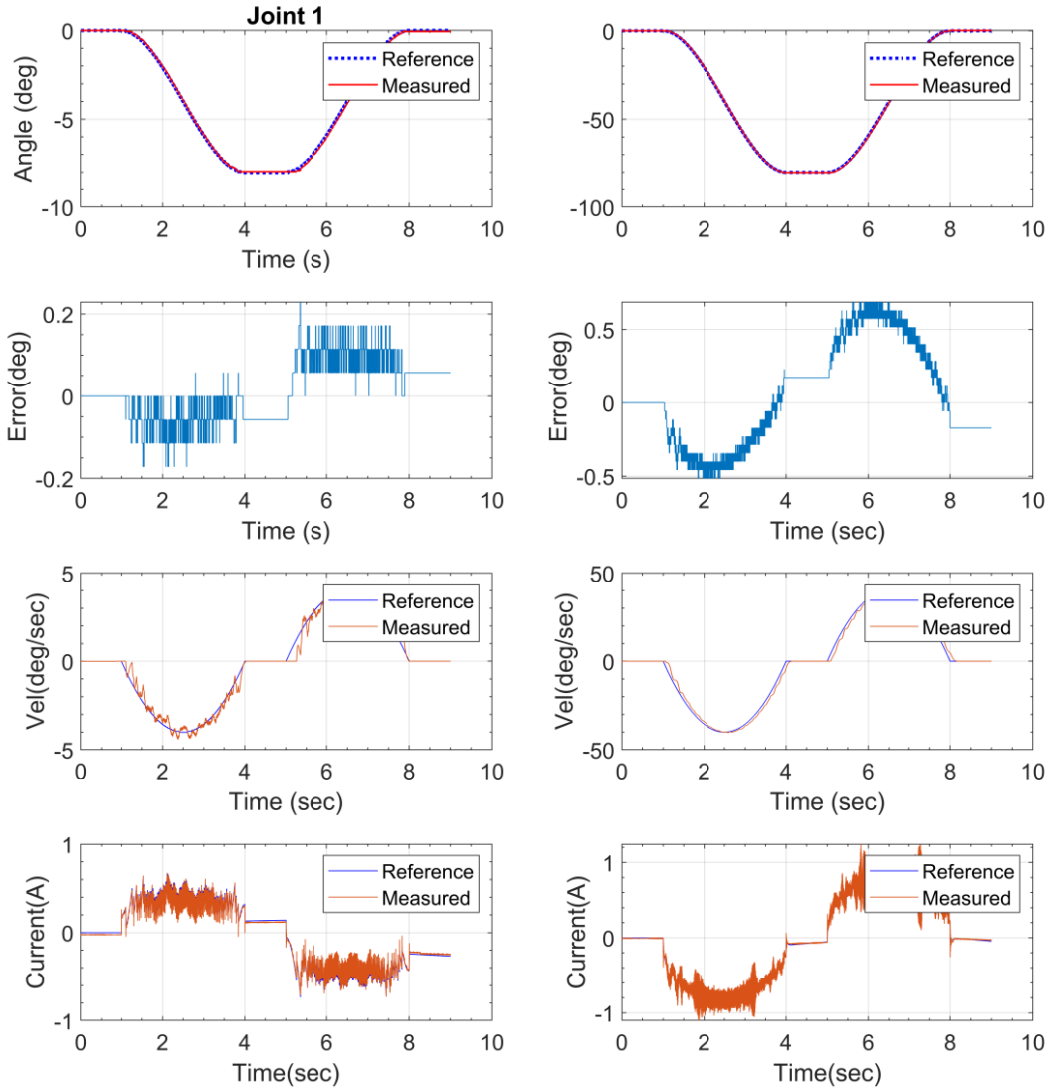

Figure 7.9 Elbow Flexion-Extension exercise using PID controller in horizontal orientation of the robot

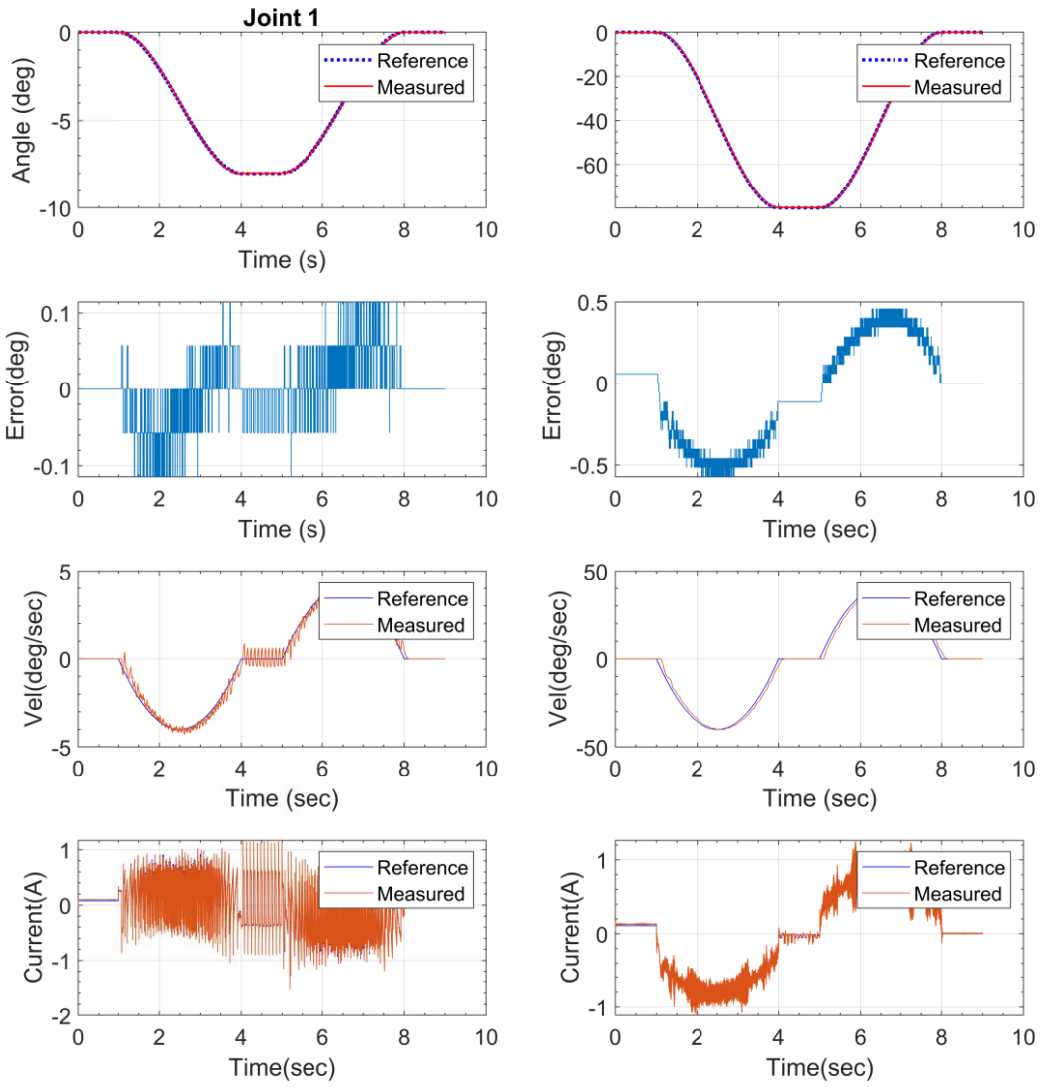

Figure 7.10 Elbow Flexion-Extension exercise using mCTC controller in horizontal orientation of the robot

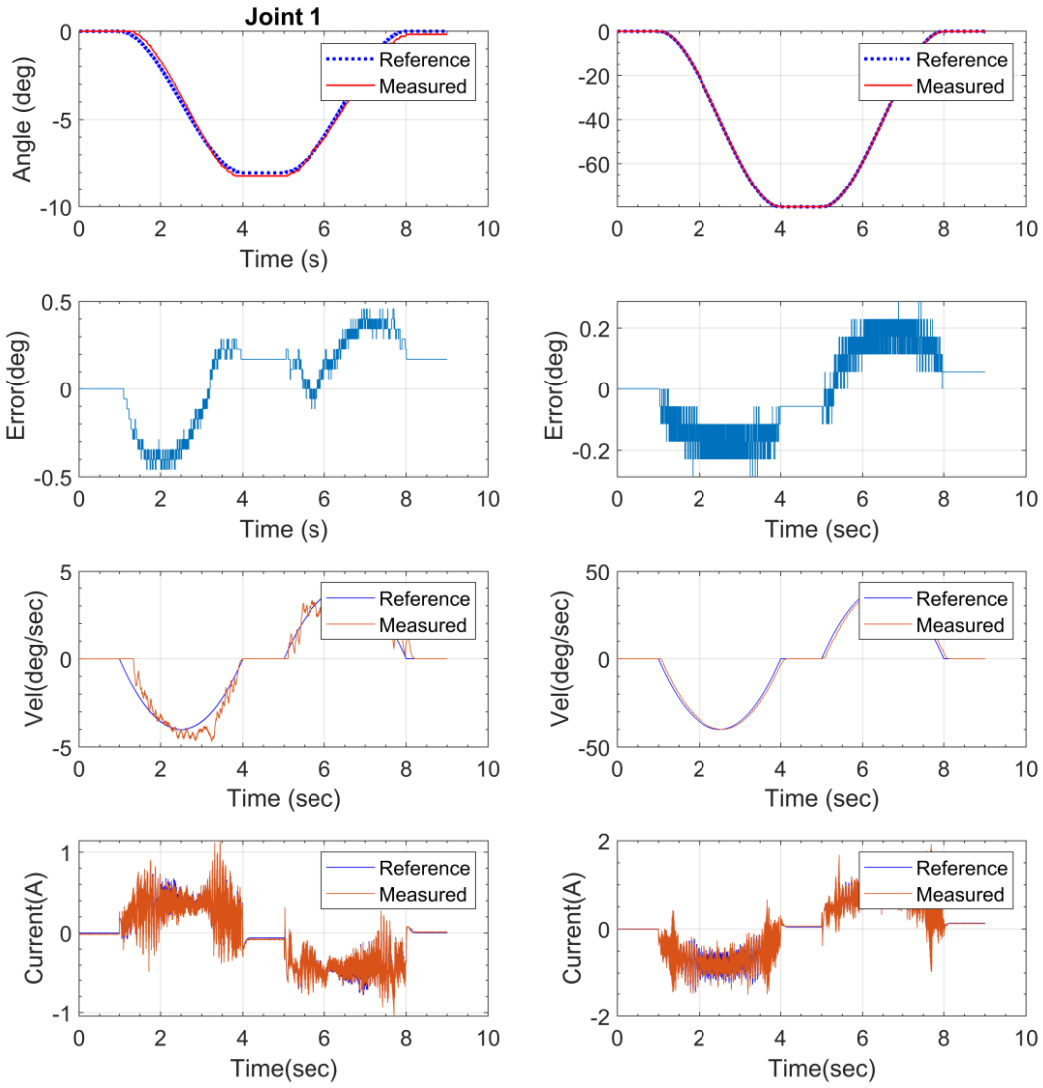

Figure 7.11 Elbow Flexion-Extension exercise using SMiRL controller in horizontal orientation of the robot

Once again, we can see that although all three controllers are capable of running the robot at decently low tracking error, all three of them show some amount of chattering at the gains used. This chattering can be further reduced by extended tuning of the gain parameters for each controller. Moreover, we can see using different dynamic models for horizontal and vertical orientation of the iTbot with the acceleration due to gravity is acting on different axis results in a near-identical performance for both model-based controllers (i.e., mCTC and SMiRL).

7.2 Rehabilitation Exercise Experiments

At this stage, when the mechanical, electrical, and controller performance of the iTbot is verified, some example or demo rehabilitation exercises were performed with the participation of healthy subjects (Subject-A and Subject-B). These exercises were performed to test the capability of the iTbot to provide rehabilitation therapy that matches the principles of motor rehabilitation using rehab robotics discussed in Chapter 3. The rehabilitation exercises can be grouped into three categories; passive, active, and active-assisted; based on their working principle. Each category provides a subset of the principles of motor rehabilitation.

7.2.1 Passive Rehabilitation Exercises:

Two types of passive rehabilitation exercises have been evaluated while running experiments with iTbot. The first type being repetitive motion exercises, focusing on the massed practice/repetitive practice principle of motor rehabilitation. This type of exercise can increase the dosage or duration of the therapy to a patient, increasing the speed of recovery.

For the massed practice/repetitive practice exercise, five different new trajectories were tested. These trajectories are the robot's joint-based trajectories generated by approximation of the user′s

arm's motion. As observed during the elbow flexion-extension trajectory in the previous stage, end-effector type robots like iTbot are not suitable for motion therapy of particular joints of the upper arm; instead, these types of robots are advantageous to provide multi-joint movement exercises. Therefore, the majority of the motions chosen do not focus on the individual joint of the user. Instead, those trajectories target to mimic the hand's general motions, where users can orient each joint of their arm as they wish to perform the target motion. Indeed, standard rehabilitation therapy focuses on multi-joint movement exercises, such as picking and placing an object, reaching movement exercises, etc. The trajectories chosen for this type of exercises are:

- Diagonal reaching with an intermediate point

  In this trajectory, Joint-1 moves to -20° position in 2 seconds, then come back to 8° position at the endpoint in 2 seconds more, while Joint-2 moves from 0° to -65° in first 2 seconds, then to -135° in another two seconds. Both joints then follow the same path in the same amount of time to go back to zero position. This results in a more vertical motion of the user's hand.

- Diagonal reaching in a continuous motion

  In this trajectory, Joint-1 moves directly from 0° to 8° in 4 seconds, while Joint-2 moves from 0° to -135° at the same time. This results in an arc motion of the user's hand.

- Shoulder Flexion-Extension

  In this trajectory, Joint-1 moves to -65° in 3 seconds to a suitable position, then Joint 1 and 2 moves simultaneously to -20° and -90° degree positions and back to move the user's shoulder in a flexion-extension motion.

- A vertical half star pattern

  In this pattern, Joint-1 moves from 0°, -45°, -60°, -45°, -35°, -16°, -45°, -5°, -45°, and 0°, where Joint-2 moves from 0°, -45°, -100°, -45°, -115°, -45°, 115°, -45°, -100, -45°, and 0° sequence simultaneously, each in 2 seconds, to draw a half star pattern vertically. This results in all joints' motion in the user's upper limb, focusing on elbow and shoulder flexion-extension.

- A horizontal half star pattern

  This trajectory follows the same rotations for each joint, but in a reverse direction, and is executed in the robot's horizontal configuration. This results in a half star pattern in the horizontal plane, resulting in motion in all upper limb joints, with more focus on shoulder horizontal abduction-adduction.

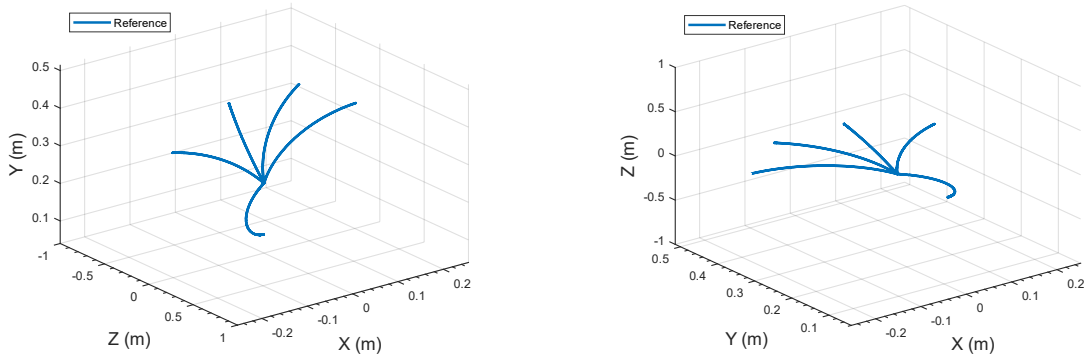

Figure 7.12 Cartesian representation of the Vertical half star pattern (left) and Horizontal half star pattern (right)

Each of these trajectories (representing multi-joint upper-limb exercises) was used with all three of the previously tested control algorithms (i.e., PID, CTC, SMiRL), and the position data, tracking

errors, and required torques were recorded for each run. Figures 7.11 through 7.25 show the position, tracking errors, and motor currents data recorded during the exercises.

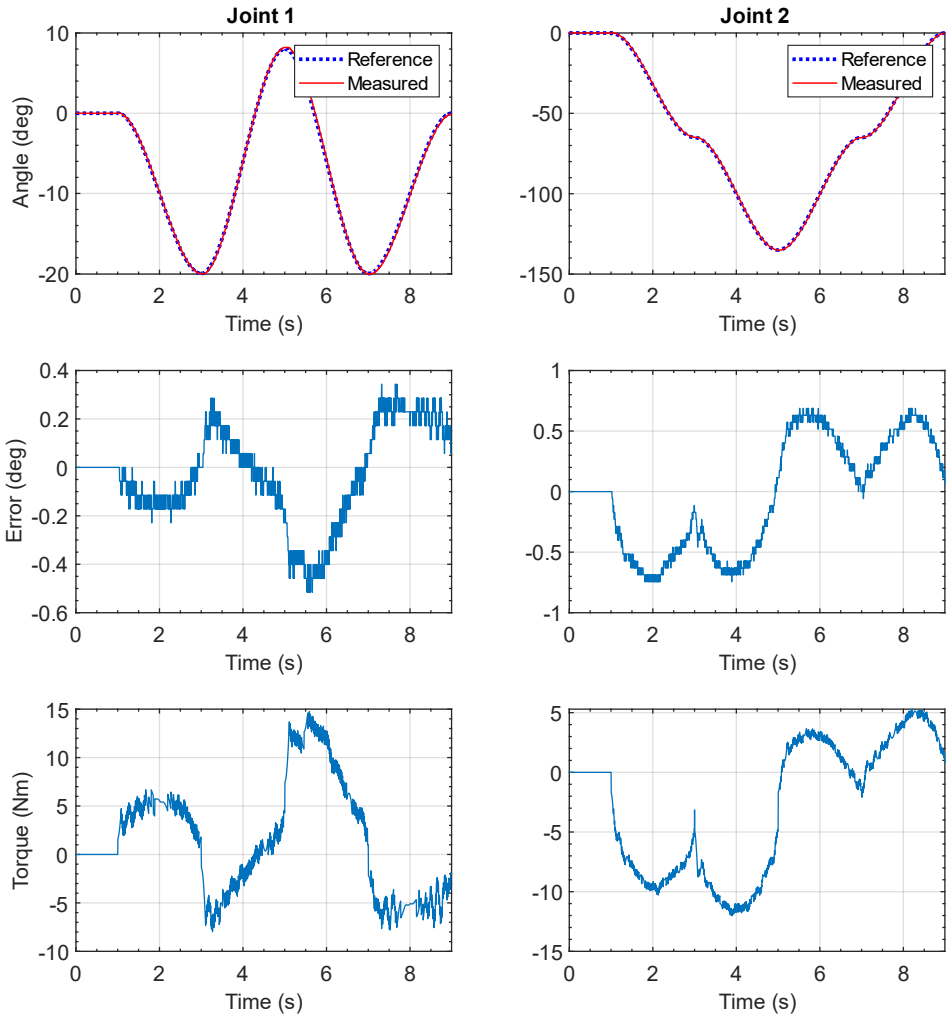

Figure 7.13 Position, Tracking Error, and Torque data for right hand Diagonal Reaching motion (intermediate point) with PID controller.

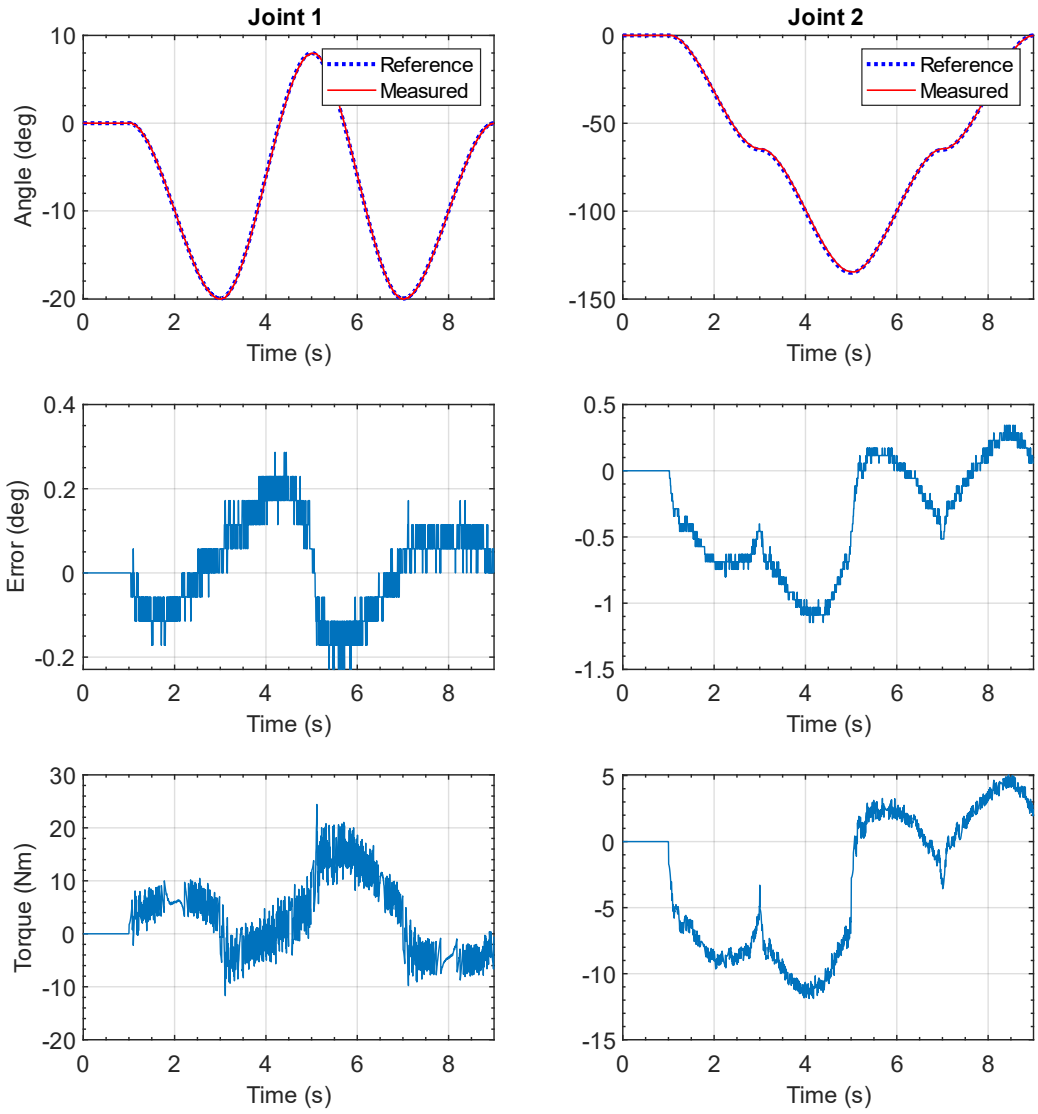

Figure 7.14 Position, Tracking Error, and Torque data for Diagonal Reaching motion (intermediate point) with mCTC controller.

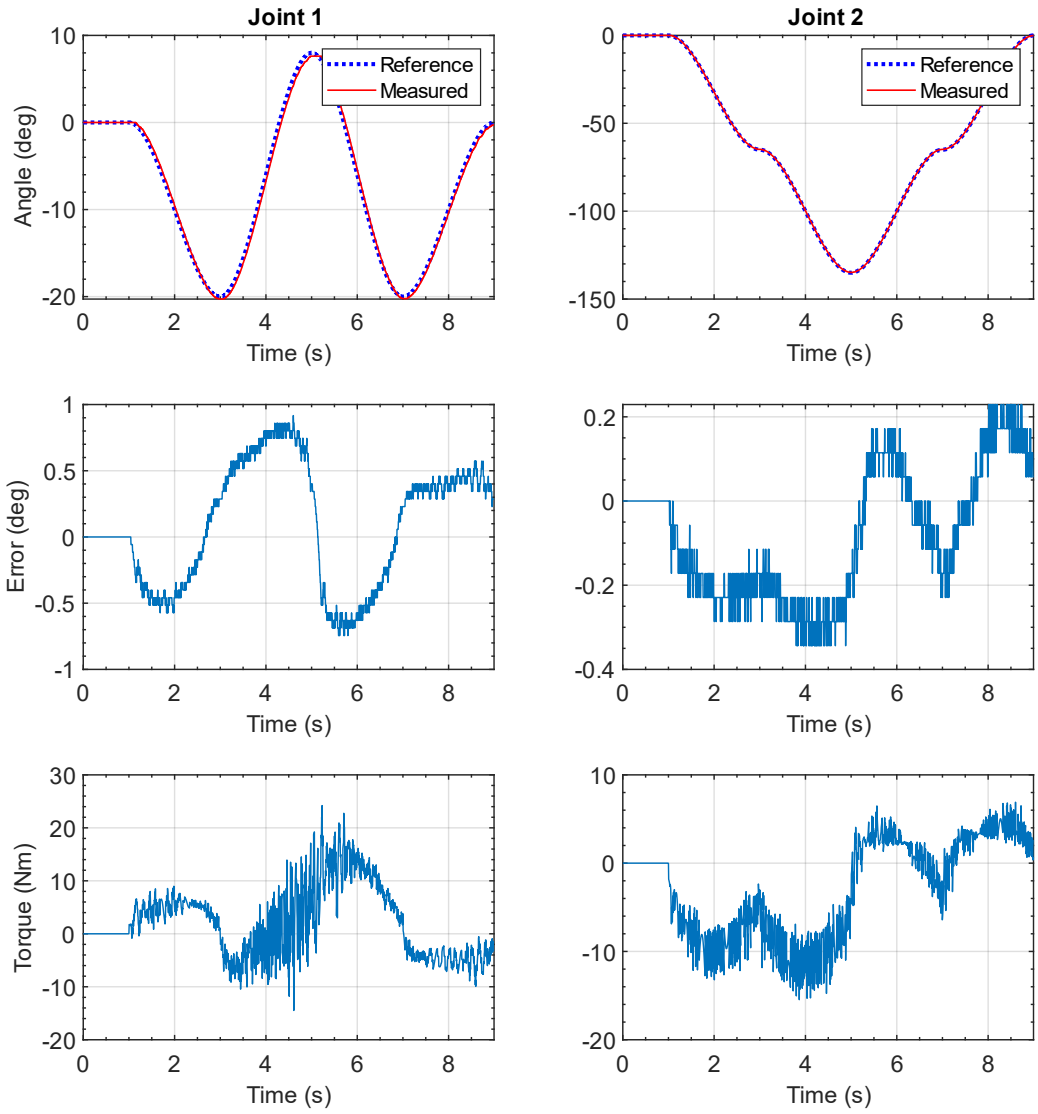

Figure 7.15 Position, Tracking Error, and Torque data for Diagonal Reaching motion (intermediate point) with SMiRL controller.

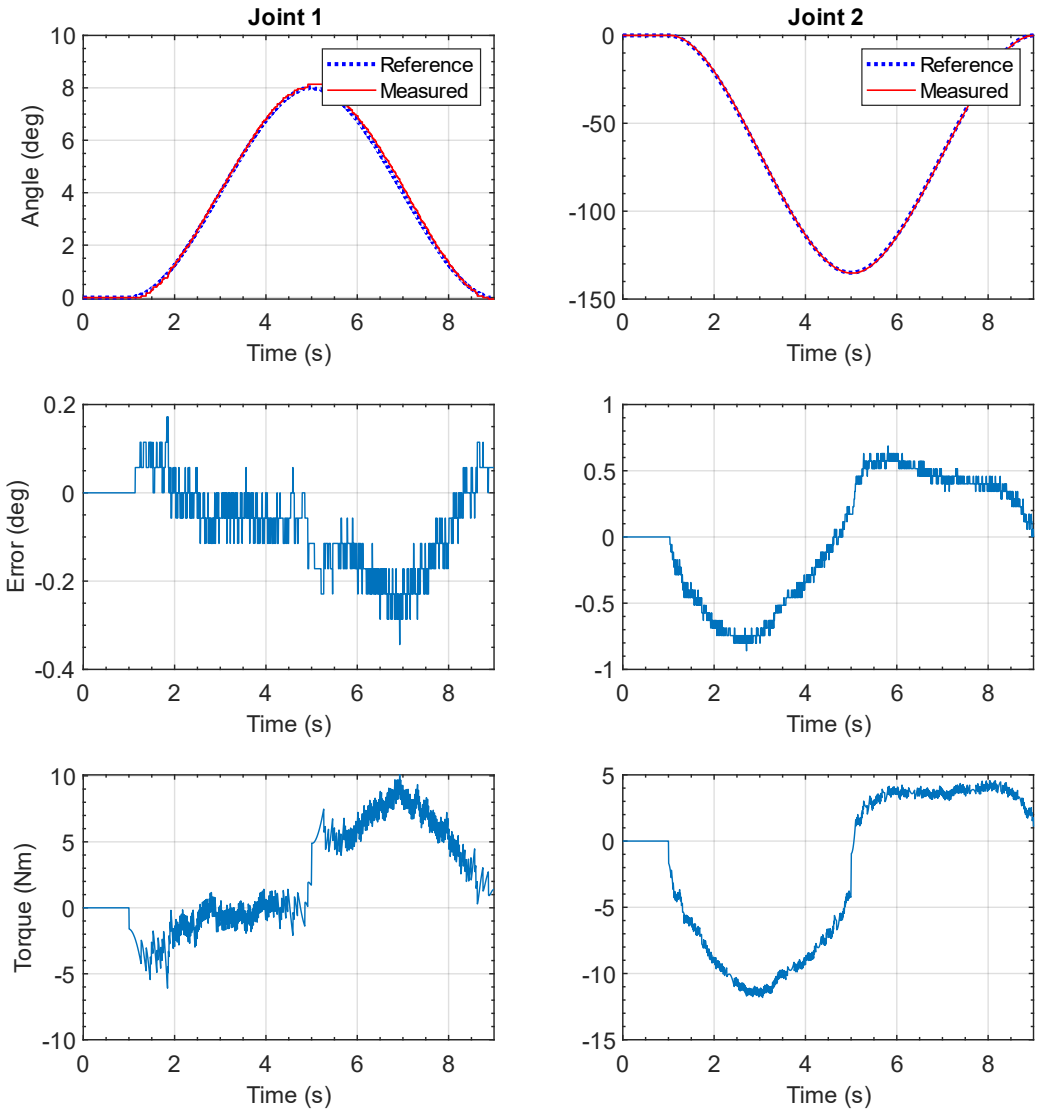

Figure 7.16 Position, Tracking Error, and Torque data for Diagonal Reaching motion (continuous) with PID controller.

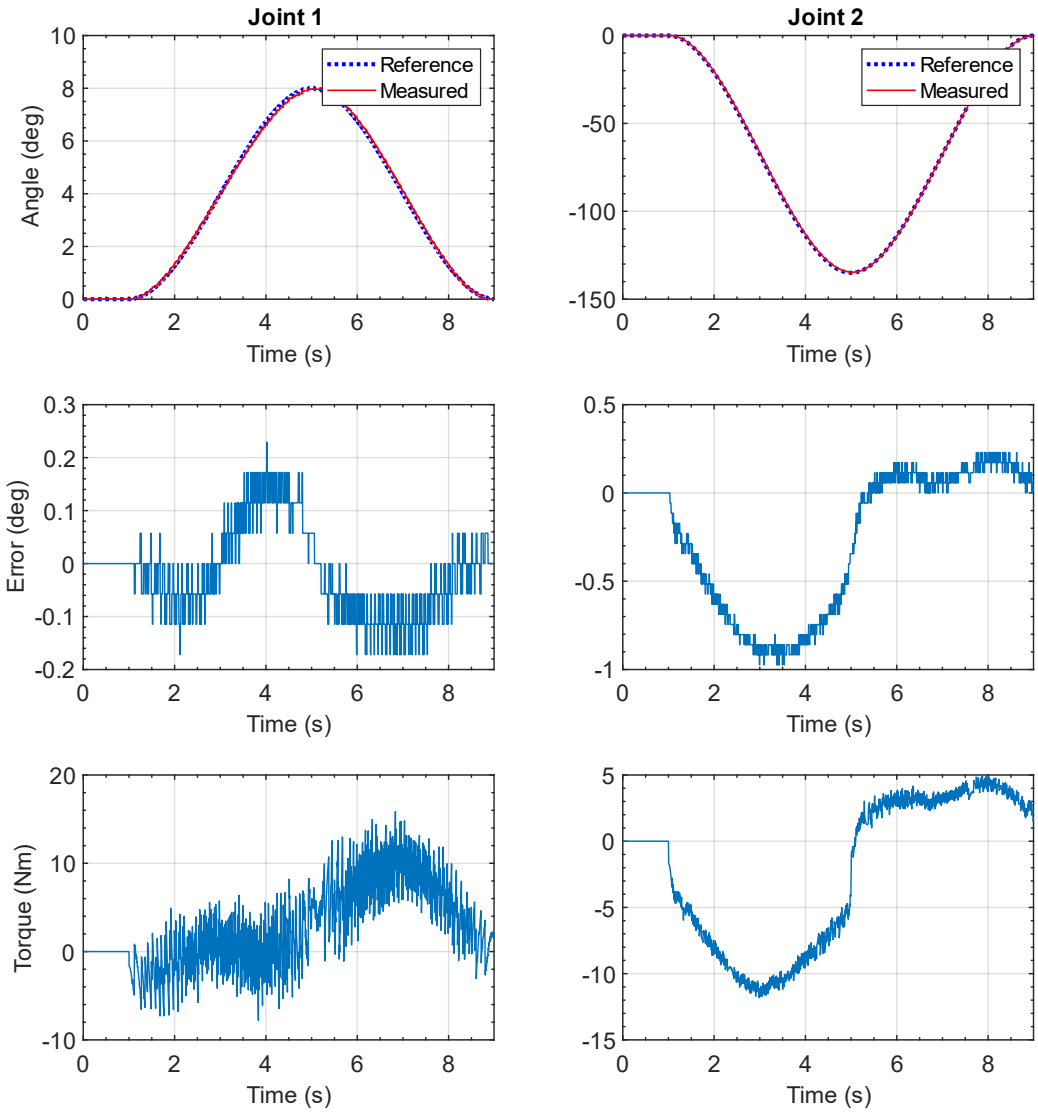

Figure 7.17 Position, Tracking Error, and Torque data for Diagonal Reaching motion (continuous) with mCTC controller.

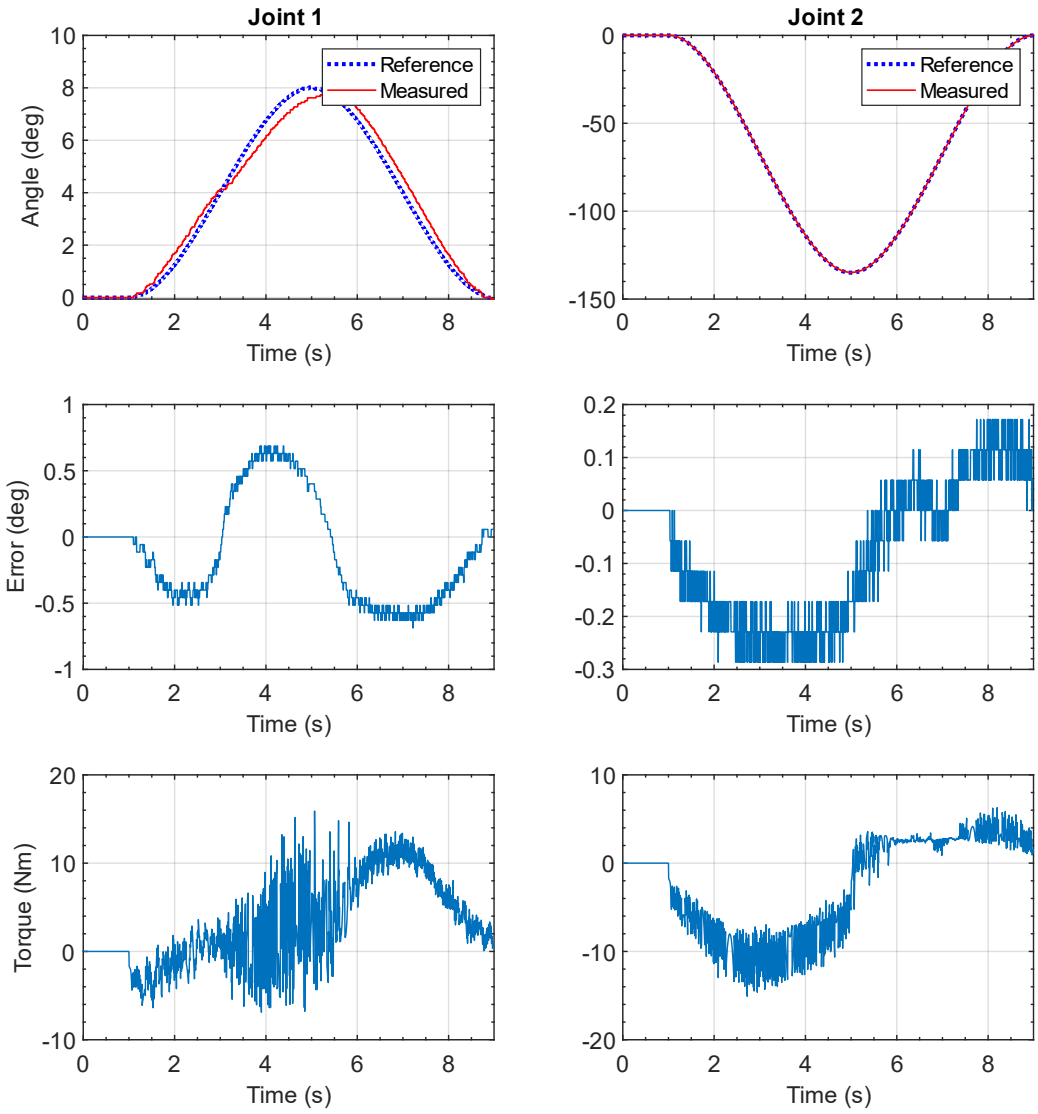

Figure 7.18 Position, Tracking Error, and Torque data for Diagonal Reaching motion (continuous) with SMiRL controller.

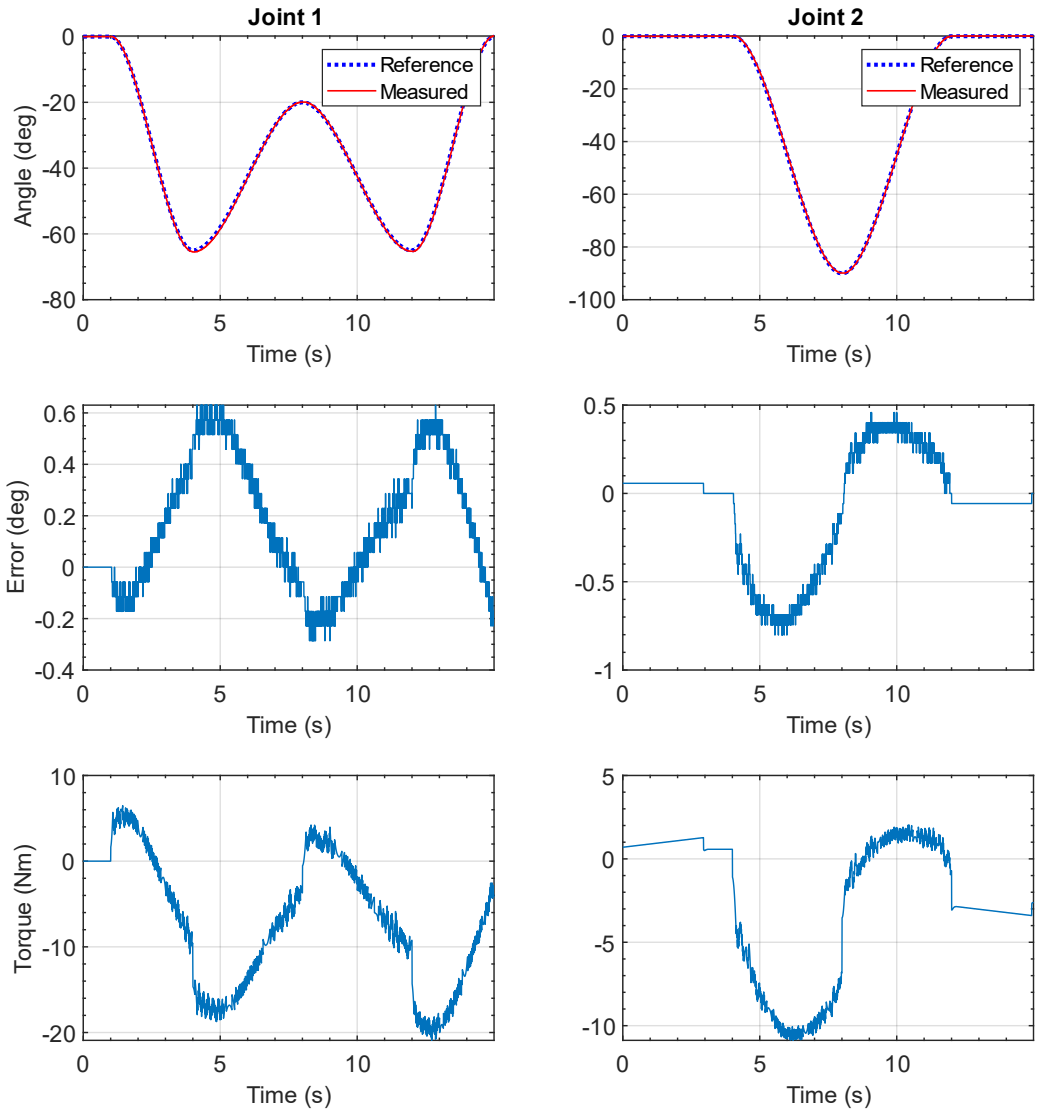

Figure 7.19 Position, Tracking Error, and Torque data observed during Shoulder Flexion-Extension motion with PID controller.

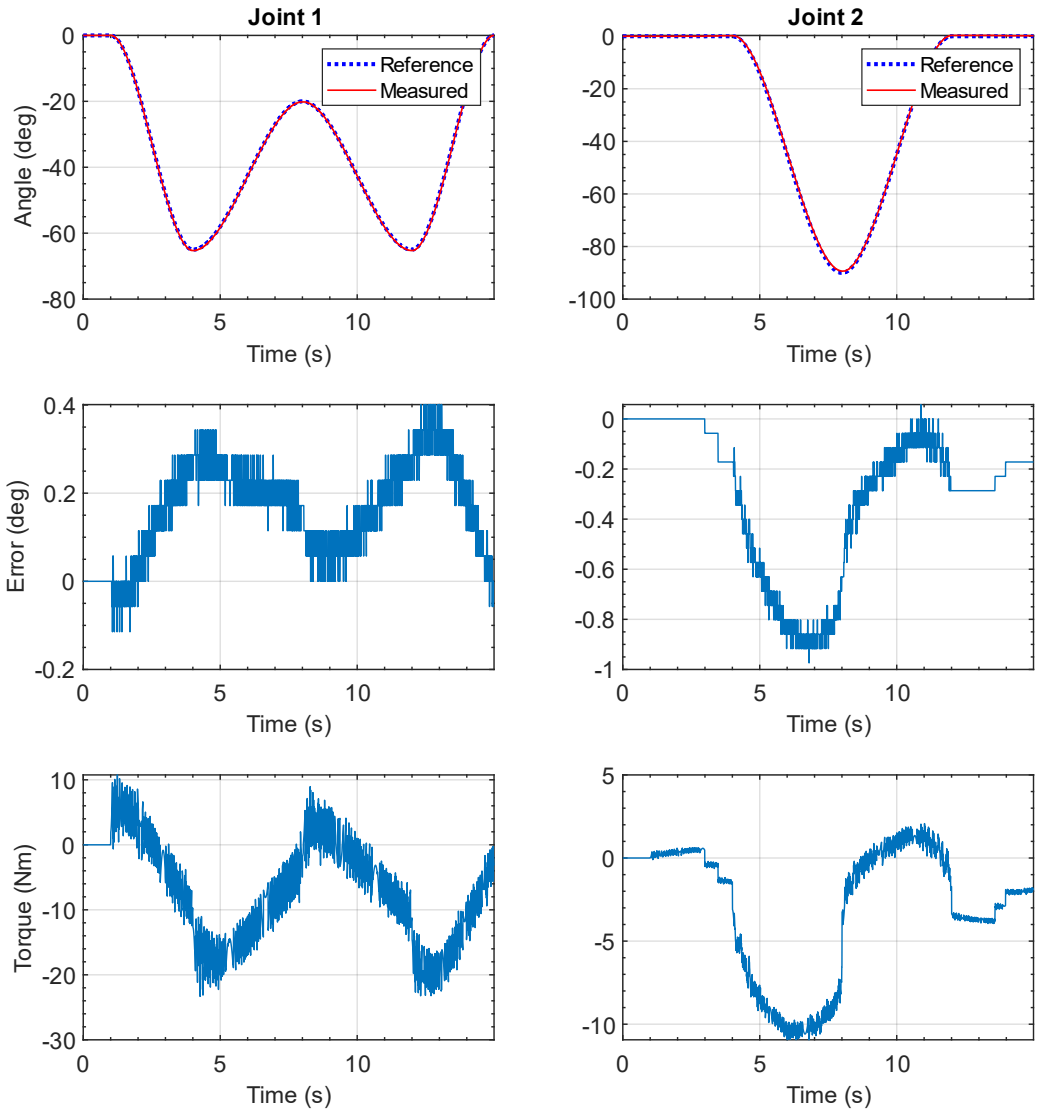

Figure 7.20 Position, Tracking Error, and Torque data observed during Shoulder Flexion-Extension motion with mCTC controller.

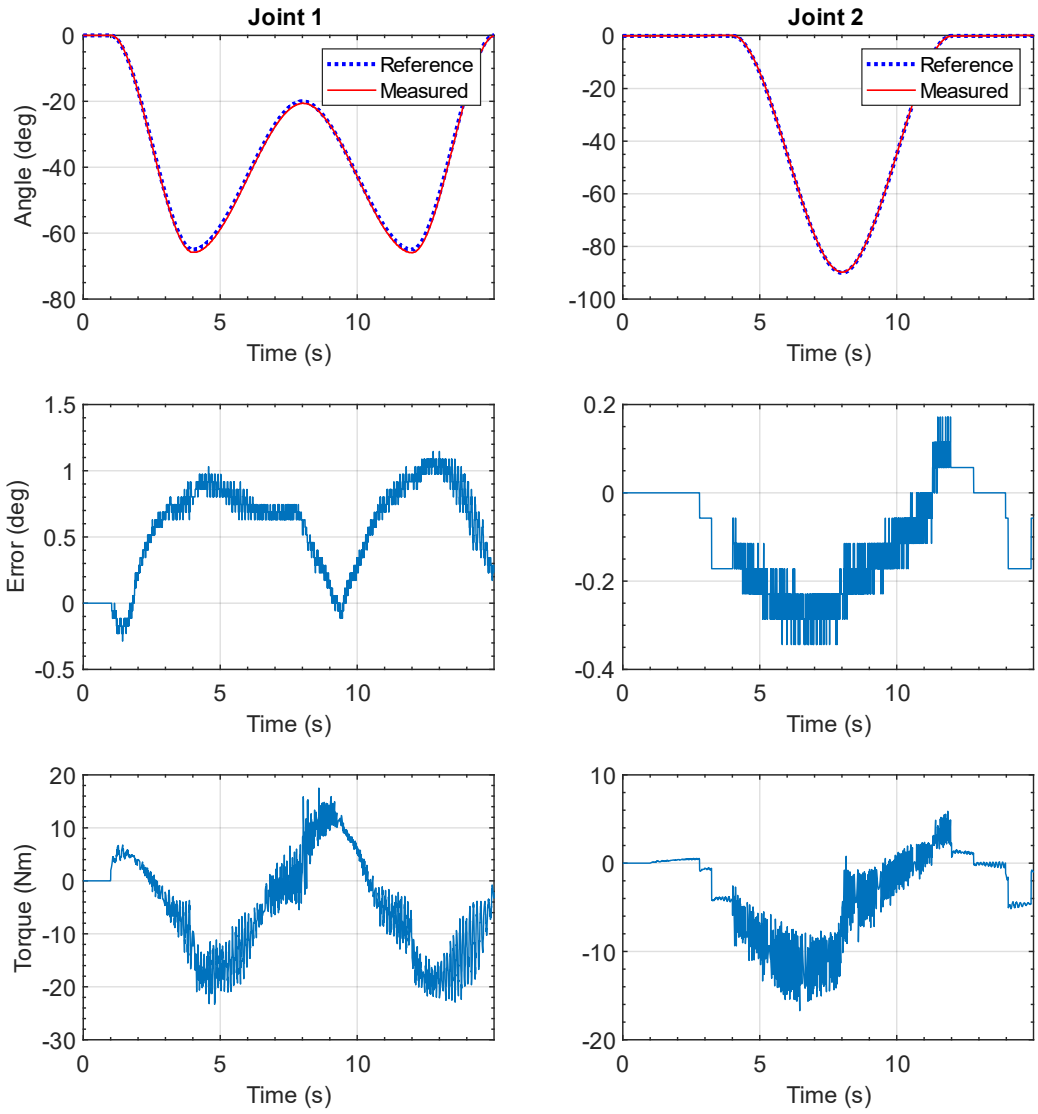

Figure 7.21 Position, Tracking Error, and Torque data observed during Shoulder Flexion-Extension motion with SMiRL controller.

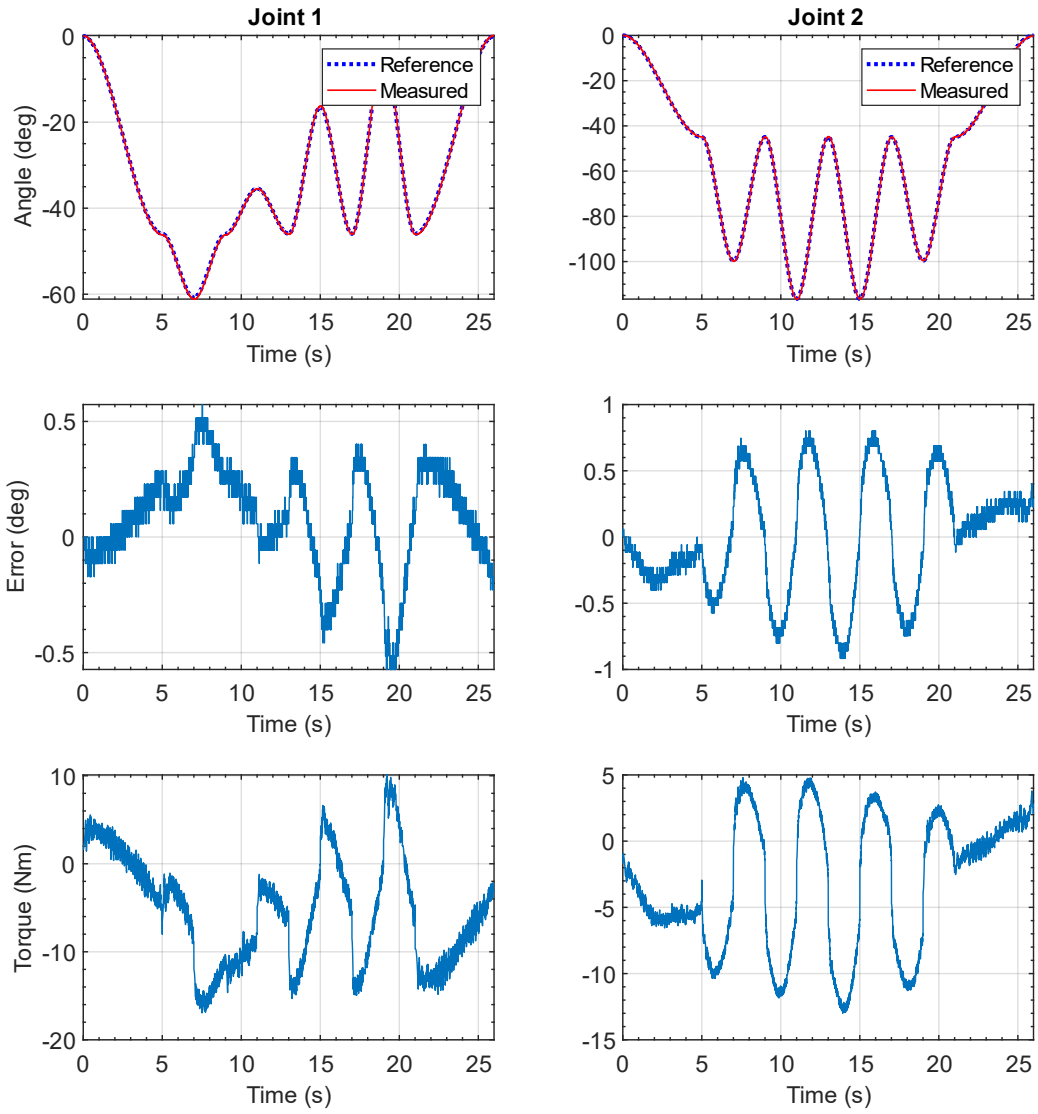

Figure 7.22 Position, Tracking Error, and Torque data for Vertical Half Star Pattern with PID controller.

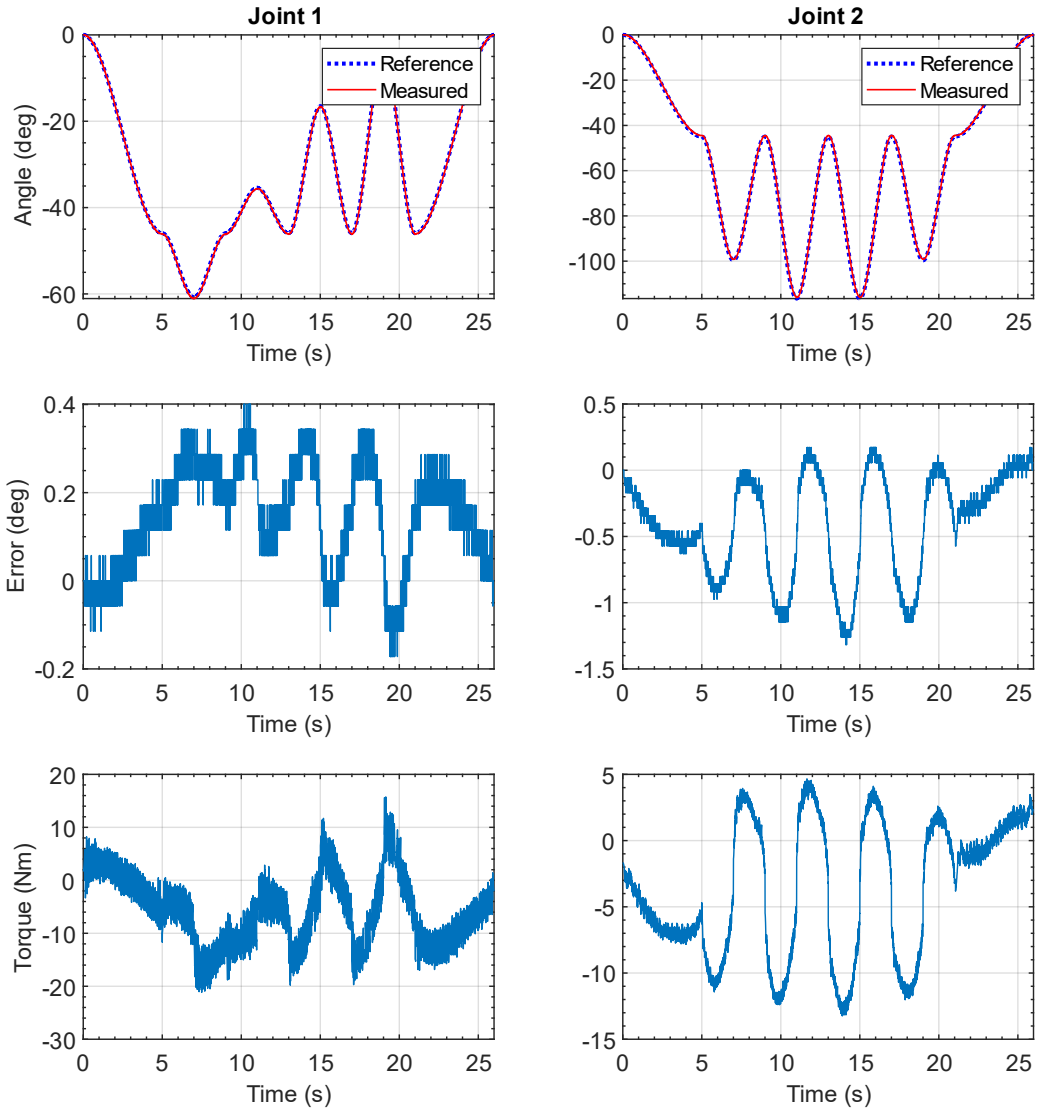

Figure 7.23 Position, Tracking Error, and Torque data for Vertical Half Star Pattern with mCTC controller.

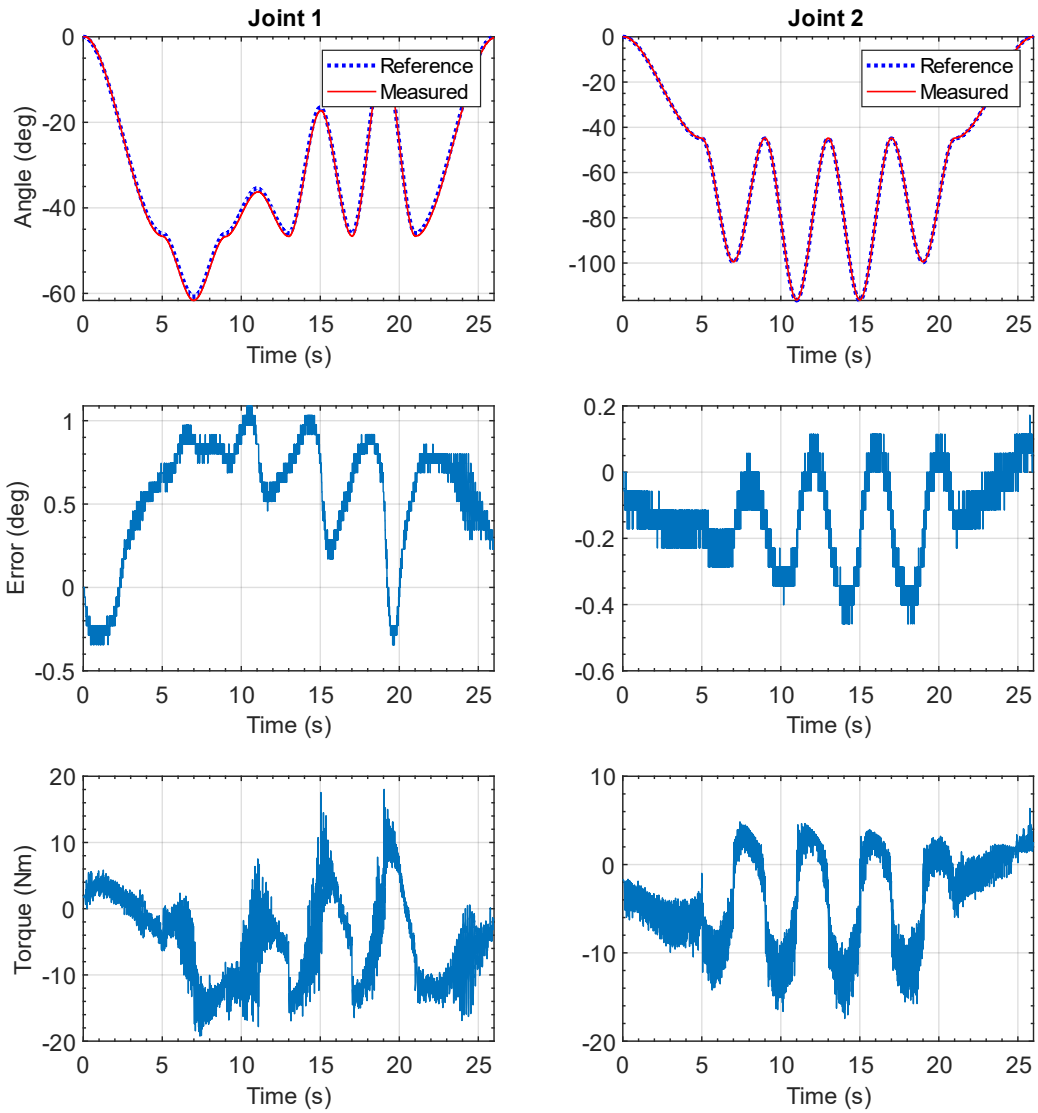

Figure 7.24 Position, Tracking Error, and Torque data for Vertical Half Star Pattern with SMiRL controller.

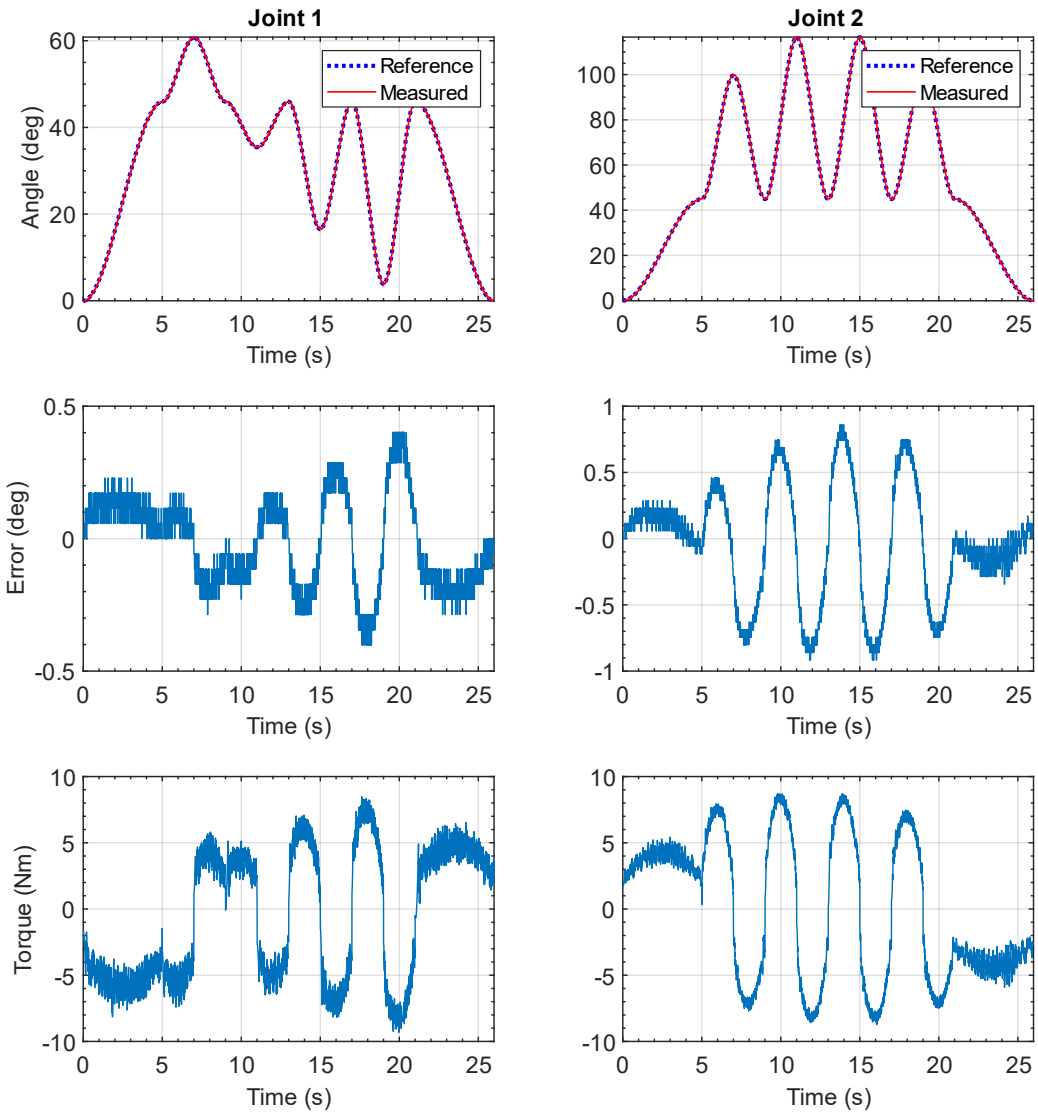

Figure 7.25 Position, Tracking Error, and Torque data for Horizontal Half Star Pattern with PID controller.

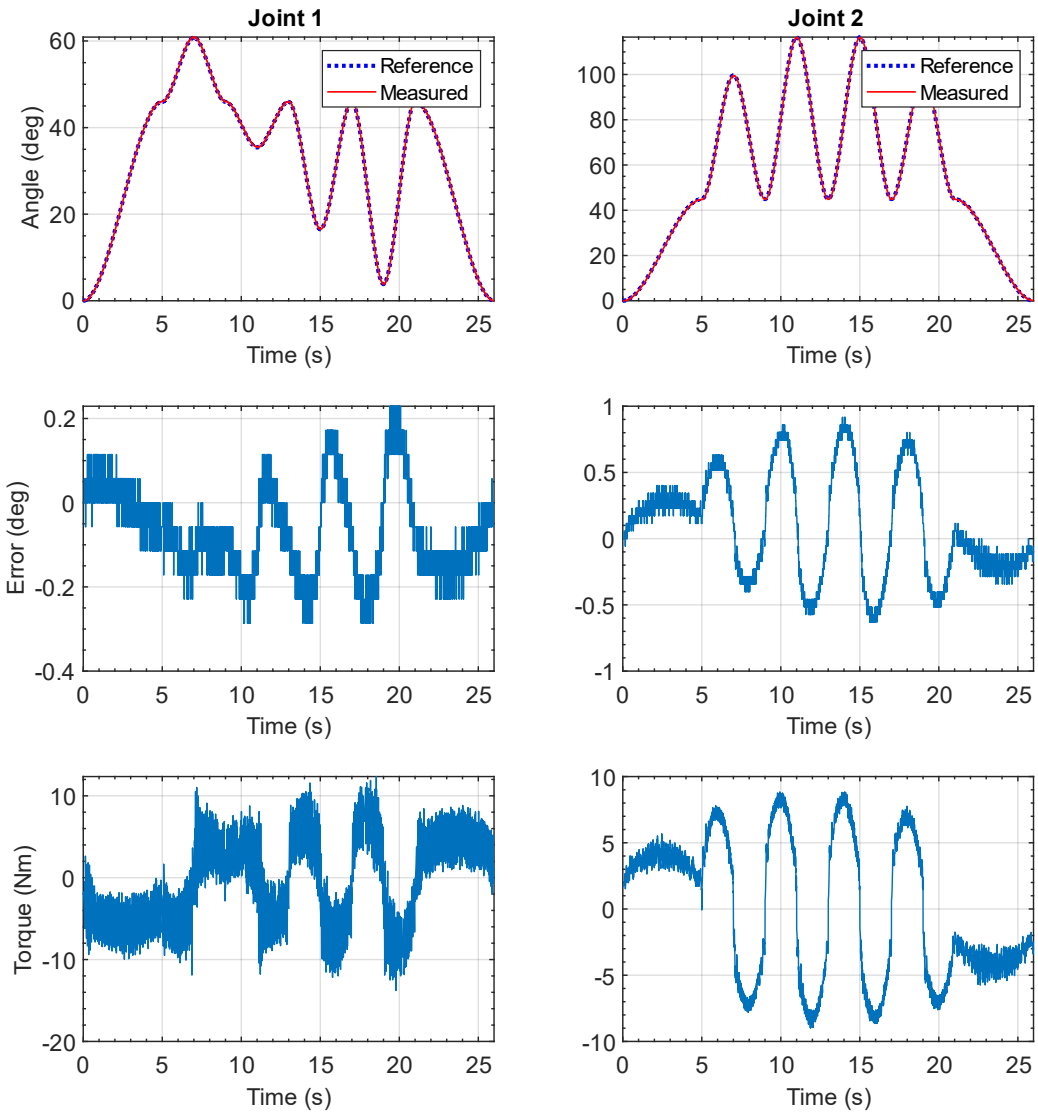

Figure 7.26 Position, Tracking Error, and Torque data for Horizontal Half Star Pattern with mCTC controller.

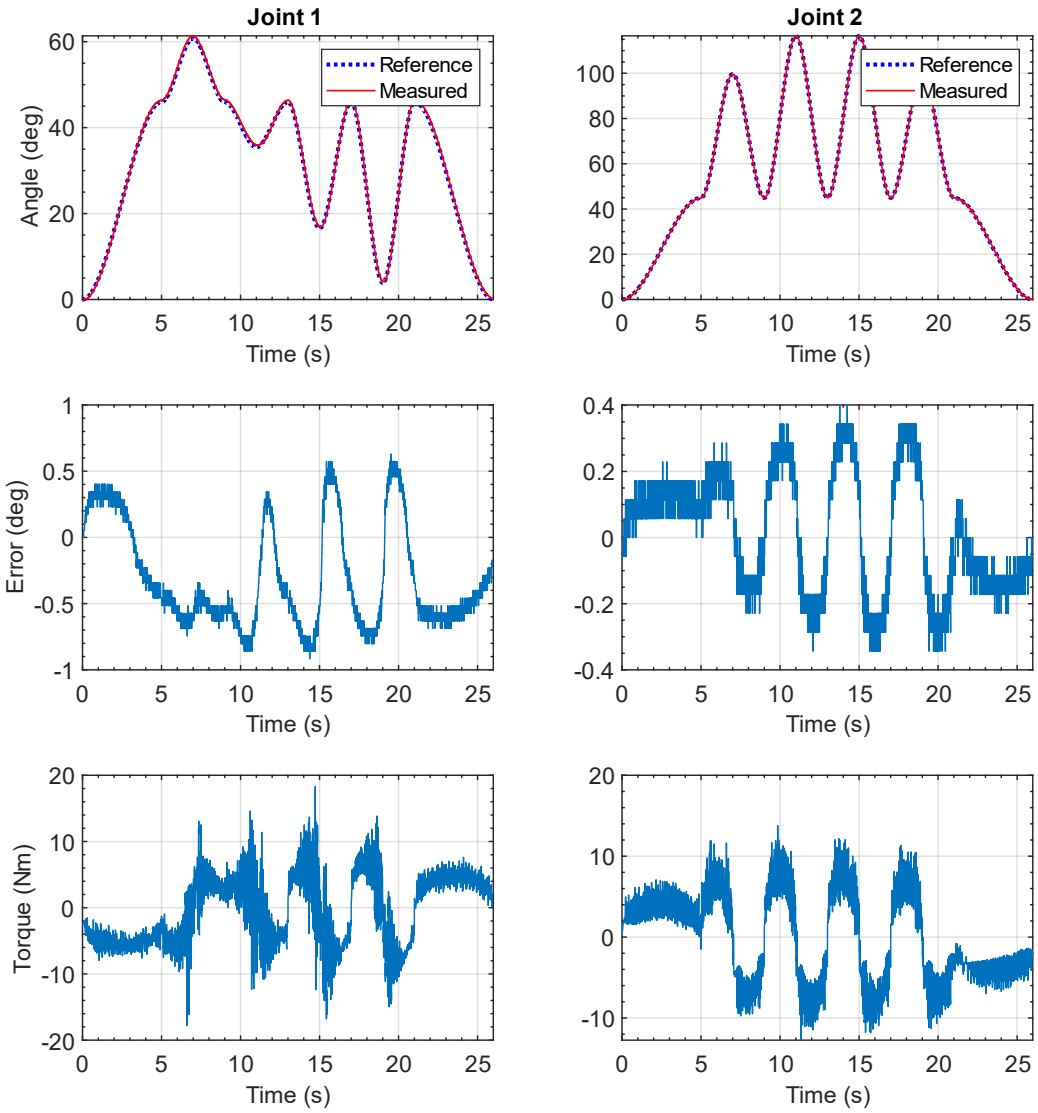

Figure 7.27 Position, Tracking Error, and Torque data for Horizontal Half Star Pattern with SMiRL controller.

From the above figures, we can see that all three controllers perform in a consistent manner for various trajectories, representing multi-joint passive rehabilitation exercises of the human upper limb.

Now, the second type of passive rehabilitation therapy demonstrated during the experimentation is record-replay type therapeutic exercise. This type of exercise is designed to enable the action-observation principle of motion rehabilitation. In the experiments with iTbot, the robot is run in a free trajectory mode with high admittance gain. In this free-run mode, the robot end-effector can be moved effortlessly with the handle connected to the force sensor. When the free trajectory is running, the user or another person can move the end-effector around to perform a rehabilitative motion task, and the motion trajectory of the robot is recorded. After the recording is done, it is possible to run the same trajectory with repetition in passive mode as a massed rehabilitation exercise.

In the experimental setup with iTbot, two different trajectory recordings have been performed by Subject-A and Subject-B. Both runs involved the first recording of a random trajectory by the users themselves with high admittance gains, resulting in very light forces required to move the robot. After the trajectory was recorded, three repetitions of the recorded trajectory were played back. During the recording, only a PID controller was used in conjunction with the admittance trajectory modifier. But during the replays, the admittance trajectory modifier was turned off to replay the repetitions in passive mode. Each replay was tested with all three (i.e., PID, CTC, and SMiRL) controllers.

Figures 7.26 and 7.27-7.29 show the recording and replay performance of the iTbot by Subject-A. Figure 7.26 shows that the desired trajectory is always zero, as in free trajectory, the robot does not have any trajectory to follow. The angle deviation is the deviation caused by the user's force input through the admittance controller. The generated torque values show that the motors are actively assisting the motion using the force sensor input from the user.

During the replay, we can see that there is a small motion added to move the joints from the endpoint of the trajectory to the starting point of the trajectory. This four-second generated trajectory is added after each loop to avoid the violent motion of the robot.

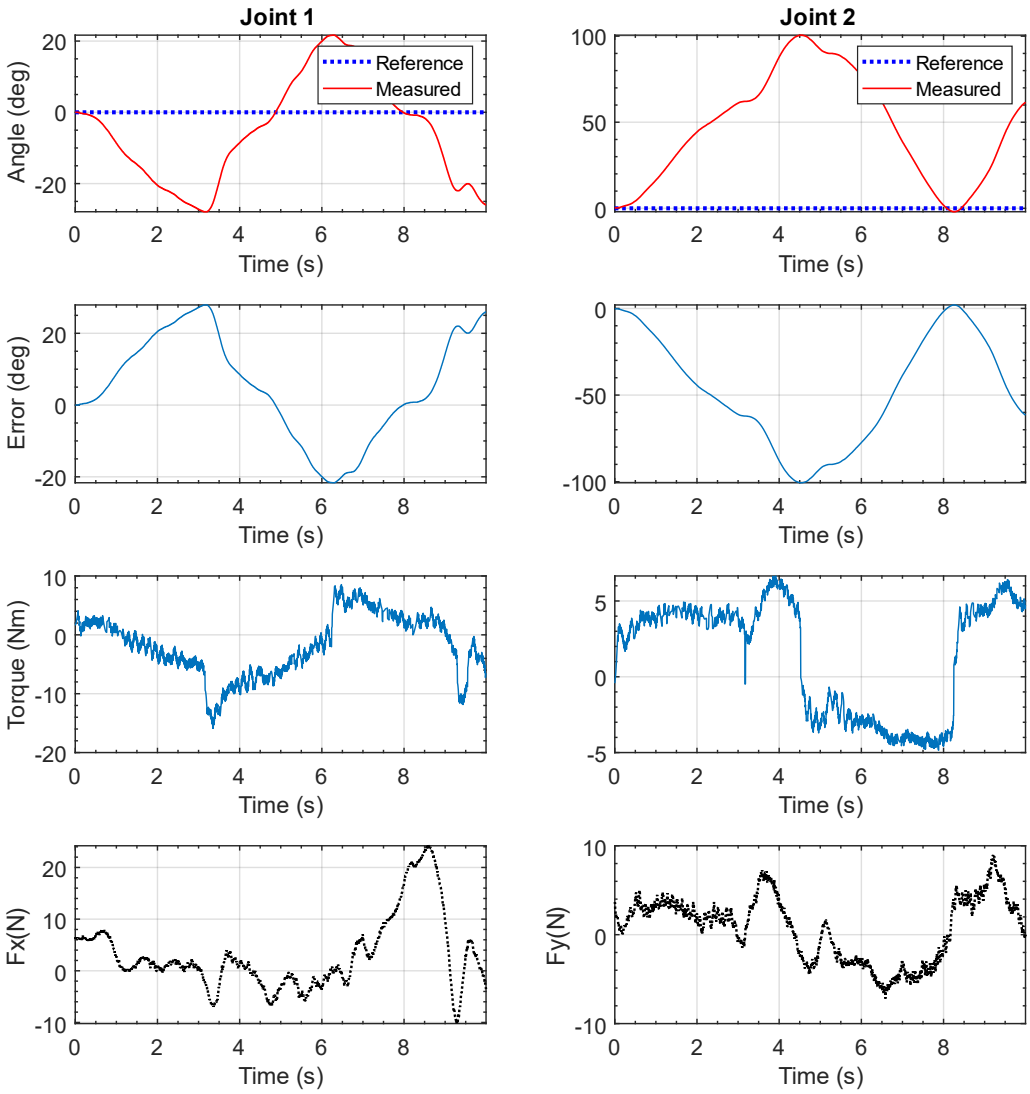

Figure 7.28 Position tracking with force sensor input when running the free trajectory with admittance

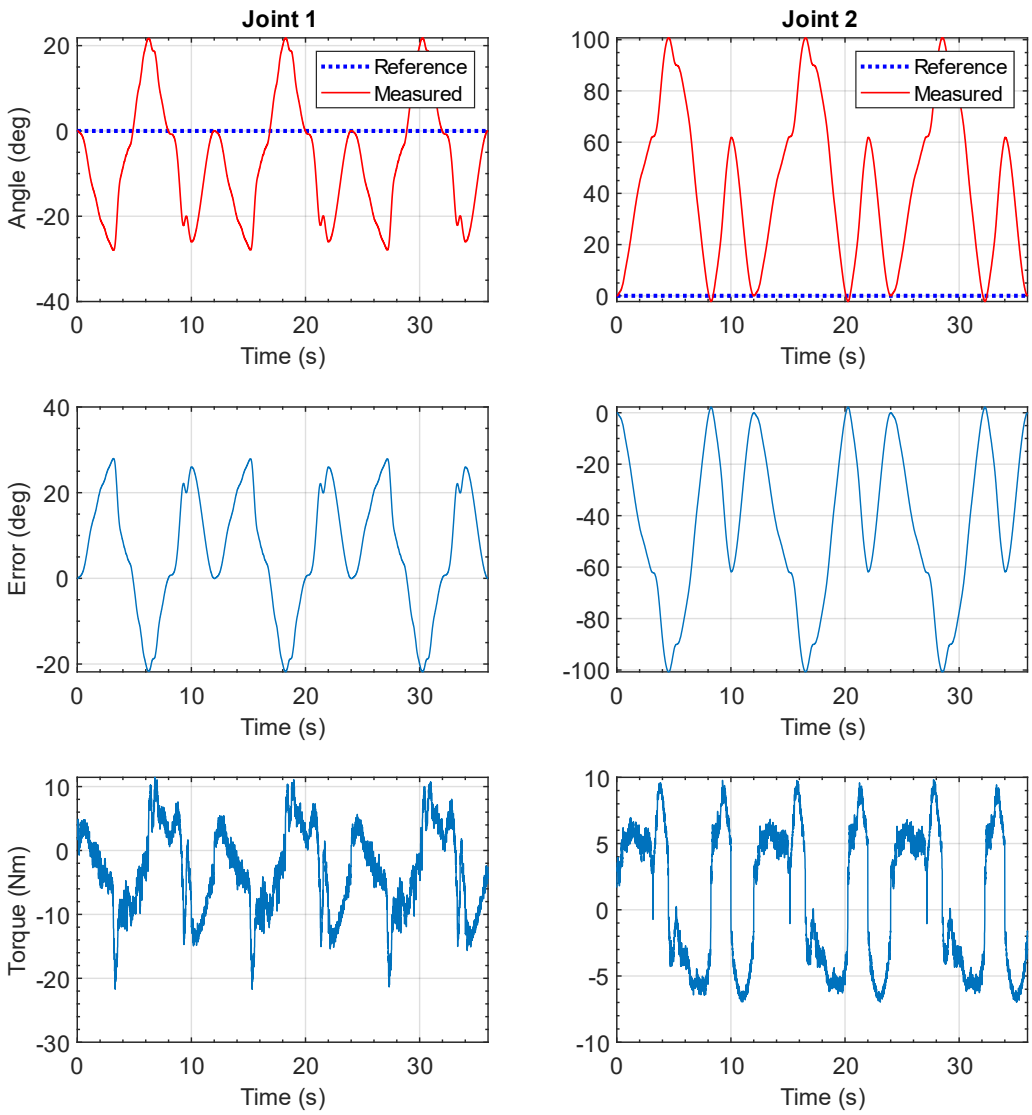

Figure 7.29 Position, Tracking Error, and Torque data for three times replay of the recorded trajectory using PID controller

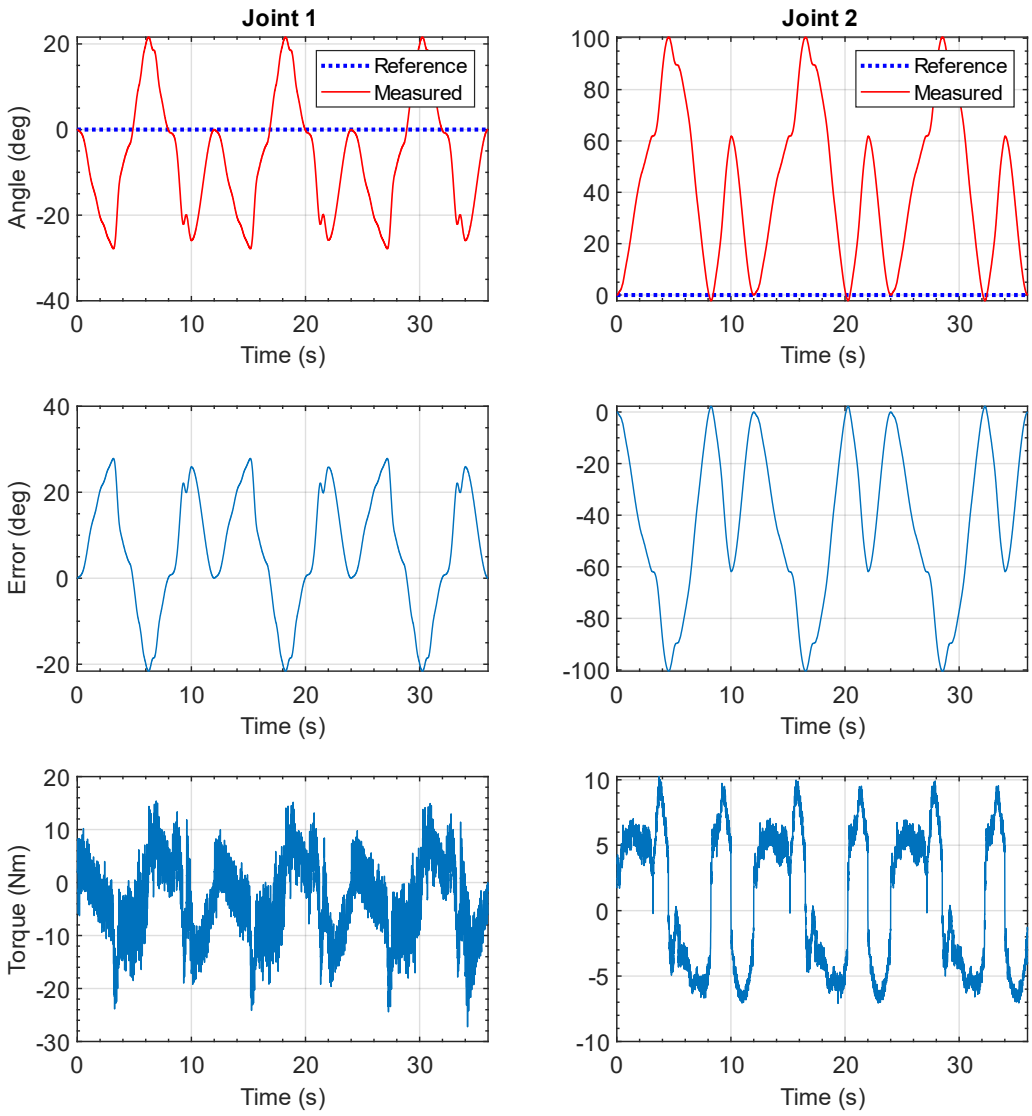

Figure 7.30 Position, Tracking Error, and Torque data for three times replay of the recorded trajectory using mCTC controller.

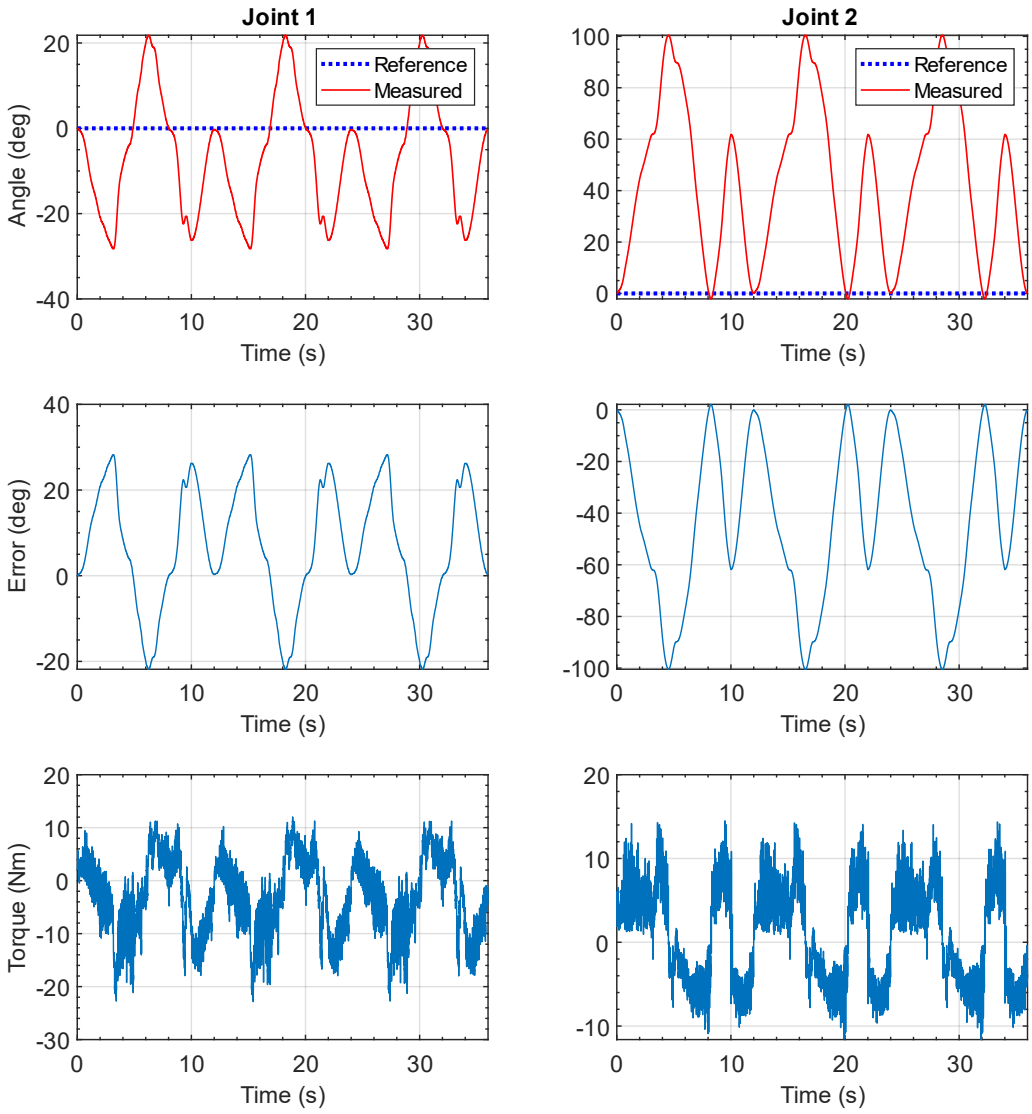

Figure 7.31 Position, Tracking Error, and Torque data for three times replay of the recorded trajectory using SMiRL controller.

7.2.2 Active Rehabilitation Exercises:

To demonstrate the active rehabilitation exercise capabilities of the iTbot, a test scenario was developed where the robot completes a predefined cartesian trajectory with the user's hand on the force sensor enabled handle of the robot, with admittance-based trajectory control activated with different amounts of admittance gains. The user's goal is to complete the trajectory with the robot without deviation, but someone with upper limb impairment receiving therapy will inadvertently apply force in incorrect directions, either due to limitation in range of motion in their arm or due to poor motor control. When these forces are applied, the robot's admittance-based trajectory control will deviate the robot out of its pre-planned trajectory. Observing these deviations can provide users implicit and explicit feedback on their rehabilitation exercises. Additionally, changing the admittance gains will make it harder or easier to deviate the robot from its planned trajectory, varying the difficulty of the exercises for the user.

A test trajectory where the robot′s end-effector moves in a square pattern in the vertical plane is used to perform experiments with the above-described scenario. In this trajectory, the iTbot's end-effector starts from a home position and moves forward 0.3m in 4 seconds, then moves upwards 0.3m in 4 seconds, then moves backward 0.3m in 4 seconds, and then moves back down 0.3m to the initial position in 4 seconds. *Figure 7.32* shows a 3D representation of this vertical square trajectory.

During experiments, first, the robot's tracking performance in this trajectory is verified in passive rehabilitation mode. PID controller with gain parameters described in Section 6.1.1 was used

throughout this experiment. The tracking performance for this trajectory in Cartesian space and joint space using the PID controller is shown in *Figure 7.33* and *Figure 7.34*.

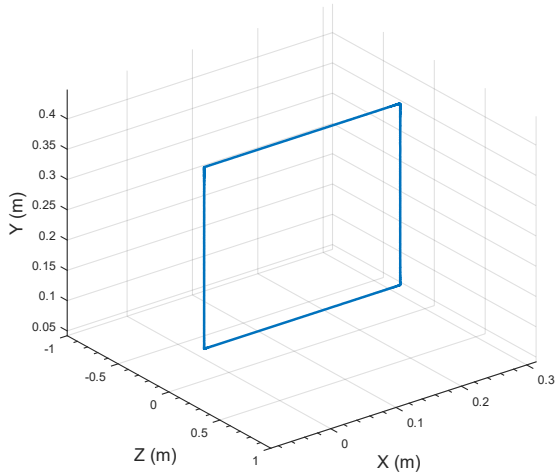

Figure 7.32 Vertical square shaped Cartesian trajectory used for demonstrating active exercise

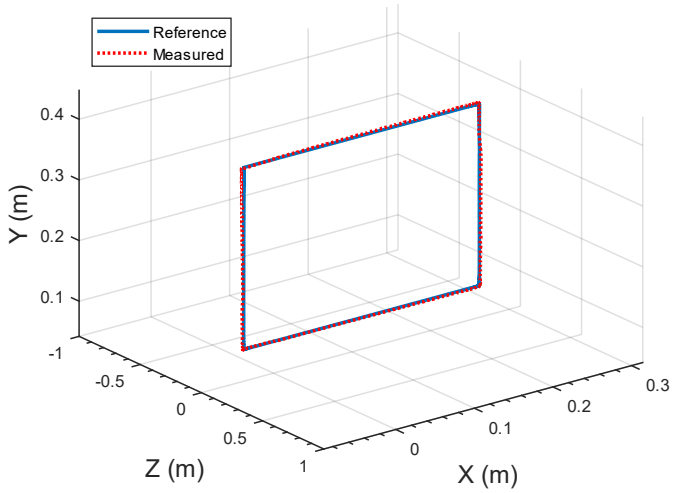

Figure 7.33 Position tracking in Cartesian space of the cartesian vertical square trajectory using PID controller

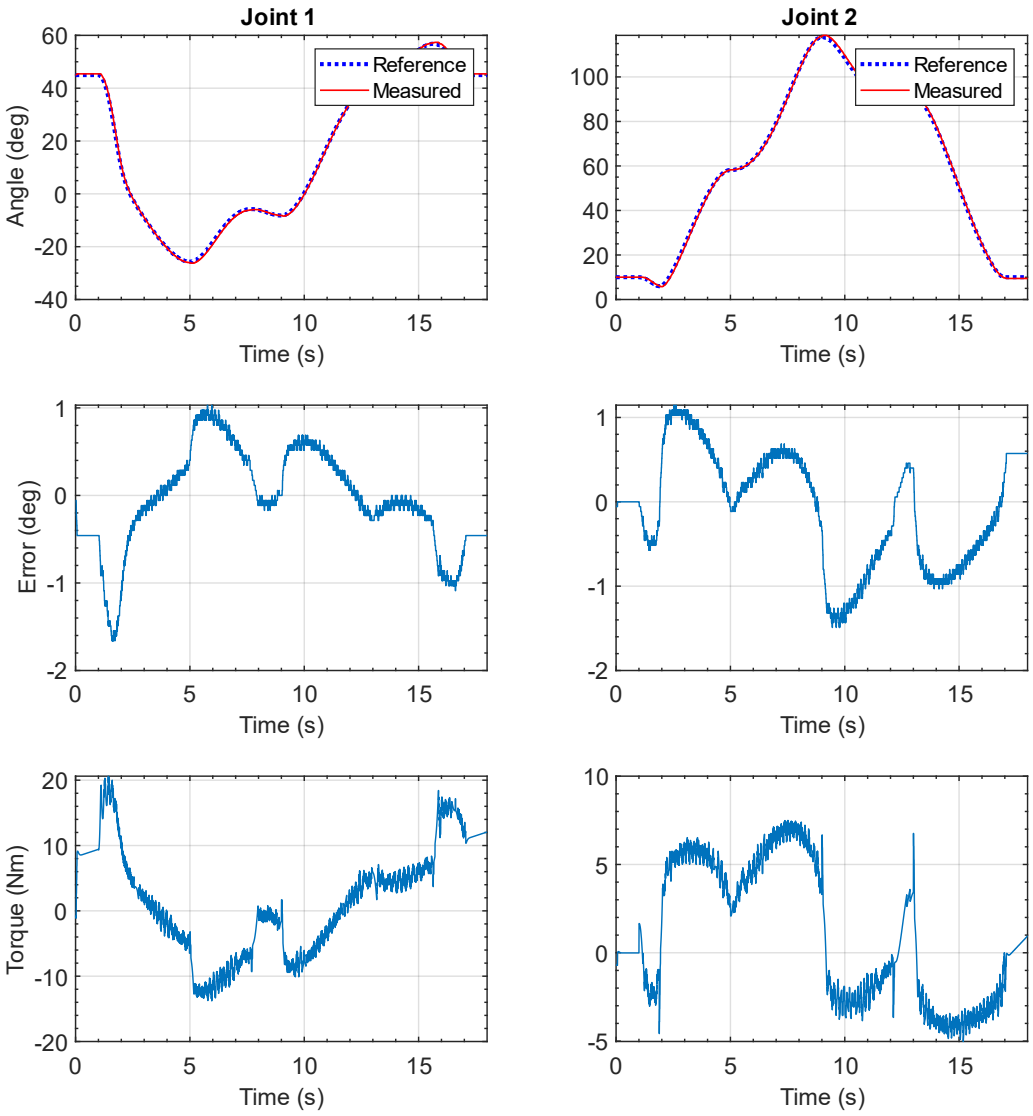

Figure 7.34 Position, Tracking Error, and Torque data in joint space for the cartesian vertical square trajectory

Then as the next step, the same trajectory was run in active mode with admittance-based trajectory control enabled, with admittance gains from (6.23) K = 0.1, 0.12, and C_s = 0,0 for Joints 1 and 2,

respectively. In these settings, the trajectory is run without any user input to the force sensor through the handle. This is done to verify the tracking performance of the iTbot without the user's active force input. *Figure 7.35* and *Figure 7.36* show the trajectory tracking along with force sensor input during this test.

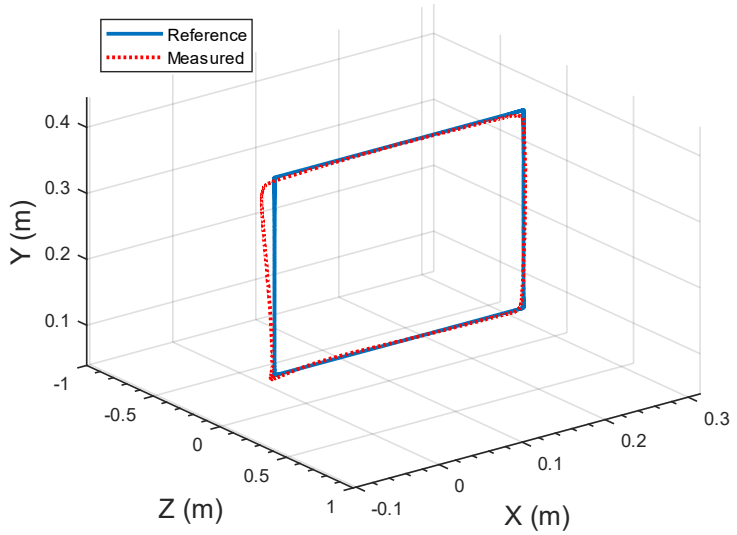

Figure 7.35 Position tracking in cartesian space of the cartesian square trajectory with admittance-based trajectory control enabled and no user input

Here, we can see some deviation in the negative *X* direction in the square's upper left end. This can be explained by the lack of gravity compensation of the force control algorithm of the iTbot. In the initial configuration explained in Chapter 5, the *X*-axis of the end-effector frame and the force sensor is oriented towards gravity. When the robot is powered on, the force sensor senses that gravity is acting on the handle in the positive *X*-direction of the end-effector frame and sets a constant bias against that value. But during the execution of the trajectory, when the end-effector frame orientation changes, the gravity stops working on the end-effector *X*-axis. Therefore, the

bias voltage creates a small error in the force sensor's input, which then affects the admittance-based trajectory modifier.

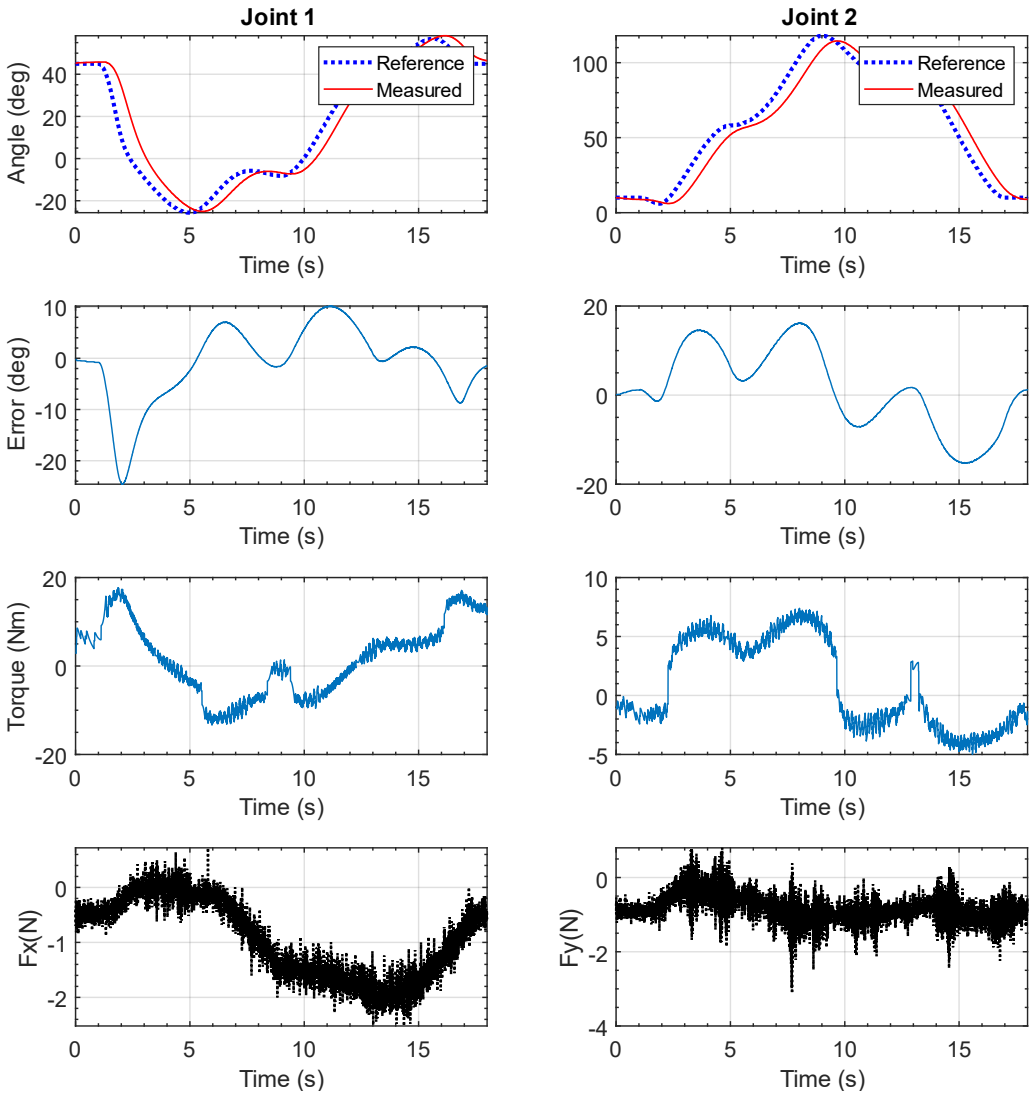

Figure 7.36 Position, Tracking Error, and Torque in joint space along with force input data of the cartesian square trajectory with admittance-based trajectory control enabled and no user input

After the test run with no user input, two separate runs of the vertical square trajectory are tested with admittance-based trajectory control enabled, with user input from Subject-A. The subject's goal was to make the robot deviate from the test trajectory by applying random forces on the force sensor using the handle. The first test run was a “low admittance” run, where the gains of the admittance-based trajectory controller set to allow low admittance, and the second test run was a “high admittance” run where the gains were adjusted to allow high admittance. During the first run, the spring constant gain from (6.23) K was set to K=0.1, 0.12 for Joints 1 and 2 respectively, and during the second run, K was set to K=0.3, 0.4 for Joints 1 and 2 respectively. The damping constant C_s was set to 0 for both joints in both cases.

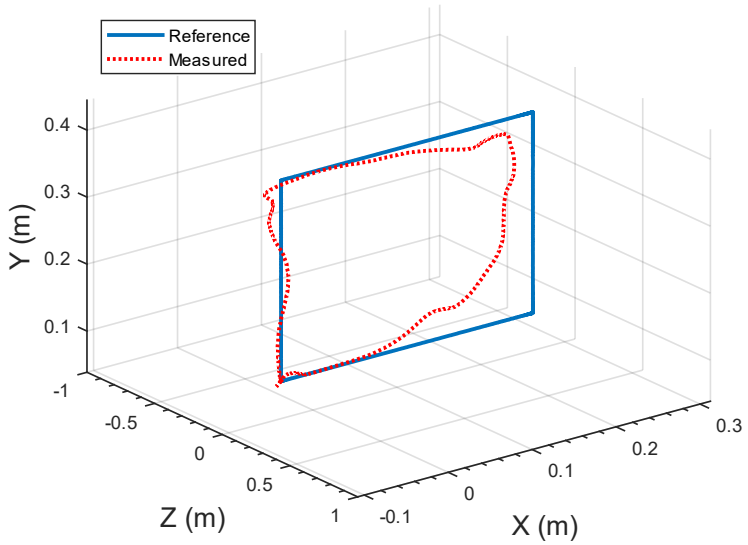

Figure 7.37 Position tracking in Cartesian space of the Cartesian square trajectory with admittance-based trajectory control enabled in “low admittance” run

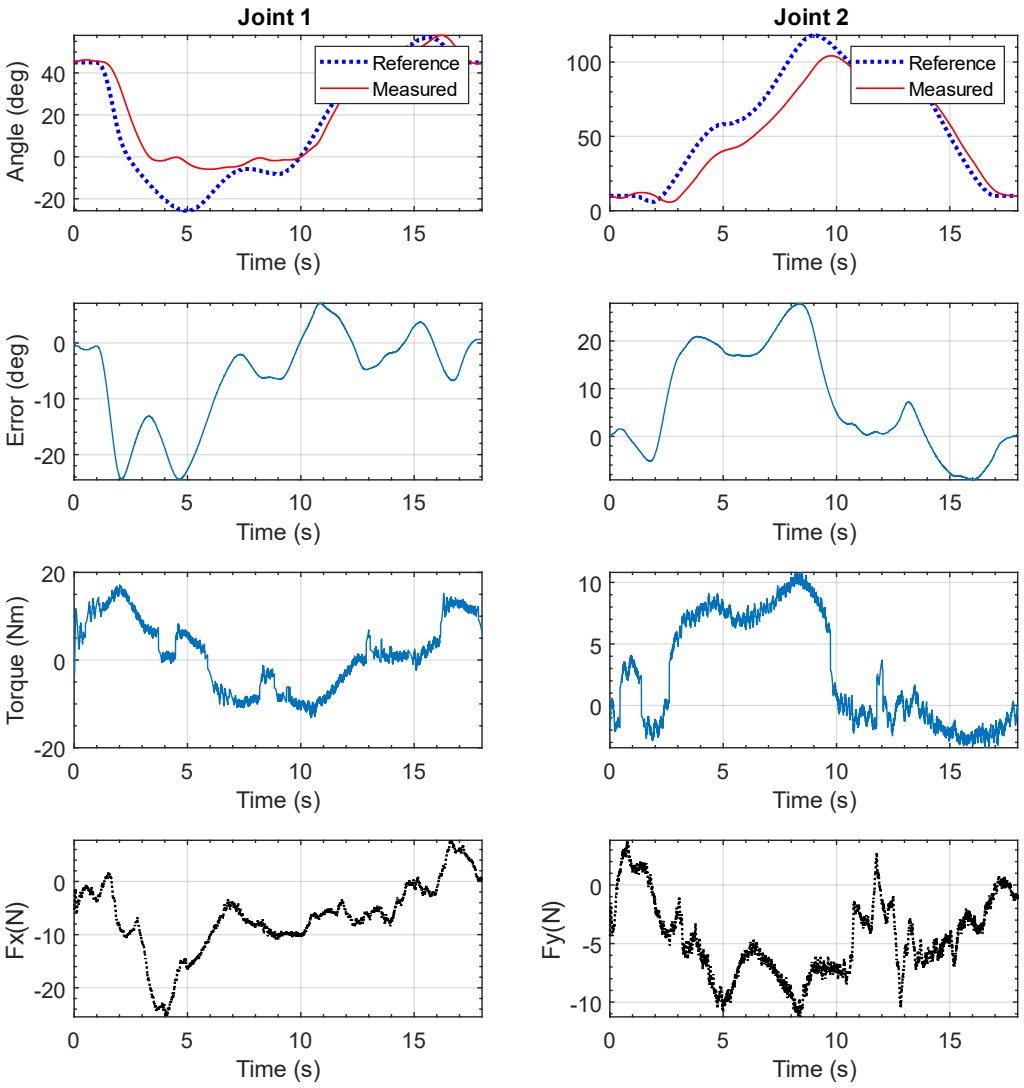

Figure 7.38 Position, Tracking Error, and Torque in joint space along with force input data of the Cartesian square trajectory with admittance-based trajectory control enabled in "low admittance" run

Figure 7.37 and *Figure 7.38* show the Cartesian position tracking; joint space position, tracking errors, joint torques; and force sensor inputs during the "low admittance run." *Figure 7.39* and *Figure 7.40* show the Cartesian position tracking, joint space position, tracking errors, joint torques, and force sensor inputs during the "high admittance run."

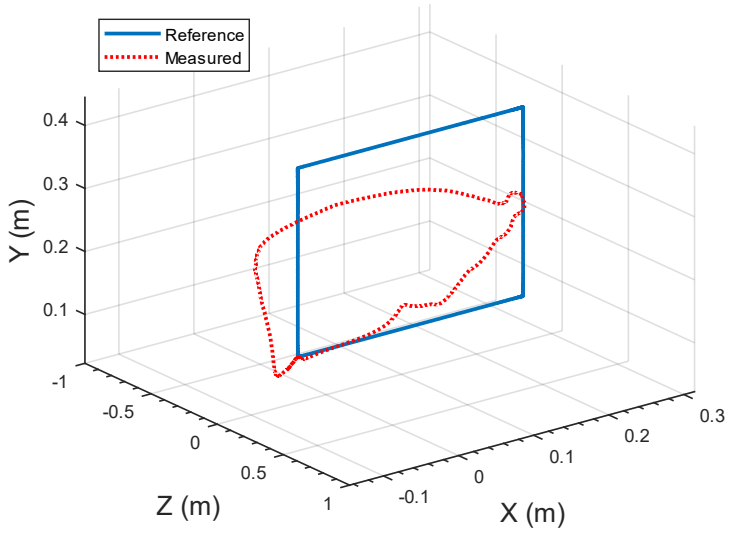

Figure 7.39 Position tracking in cartesian space of the cartesian square trajectory with admittance-based trajectory control enabled in "high admittance" run

From the data seen on these two test runs, it is evident that in the "low admittance" run, a higher amount of force input (Fx = -50N to 100N, Fy = -40N to 10N range) is used to cause less deviation (Joint-1 up to ± 20° range, Joint-2 up to ±20° range), whereas in "high admittance" run, less amount of force input (Fx = -40N to 20N, Fy = -30N to 10N range) is used to cause similar or higher deviation (Joint-1 up to ± 20° range, Joint-2 up to +40° range). This confirms the use of iTbot in admittance-based trajectory control mode in active rehabilitation therapy in different difficulty

modes. Additionally, the tracking data was shown on-line during the experiment in a video game interface (*Figure 7.41*) to provide implicit and explicit feedback during the experiment.

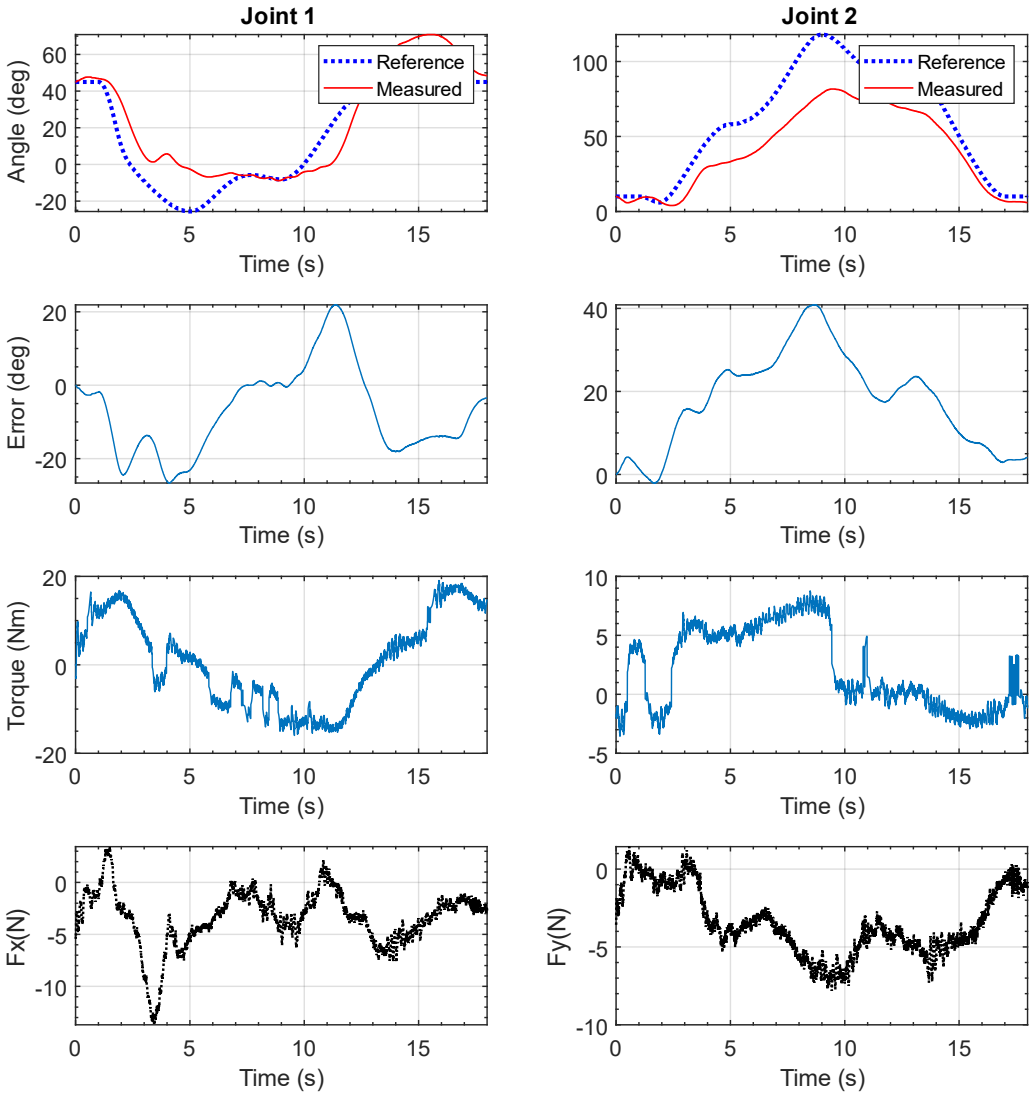

Figure 7.40 Position, Tracking Error, and Torque in joint space along with force input data of the Cartesian square trajectory with admittance-based trajectory control enabled in "high admittance" run

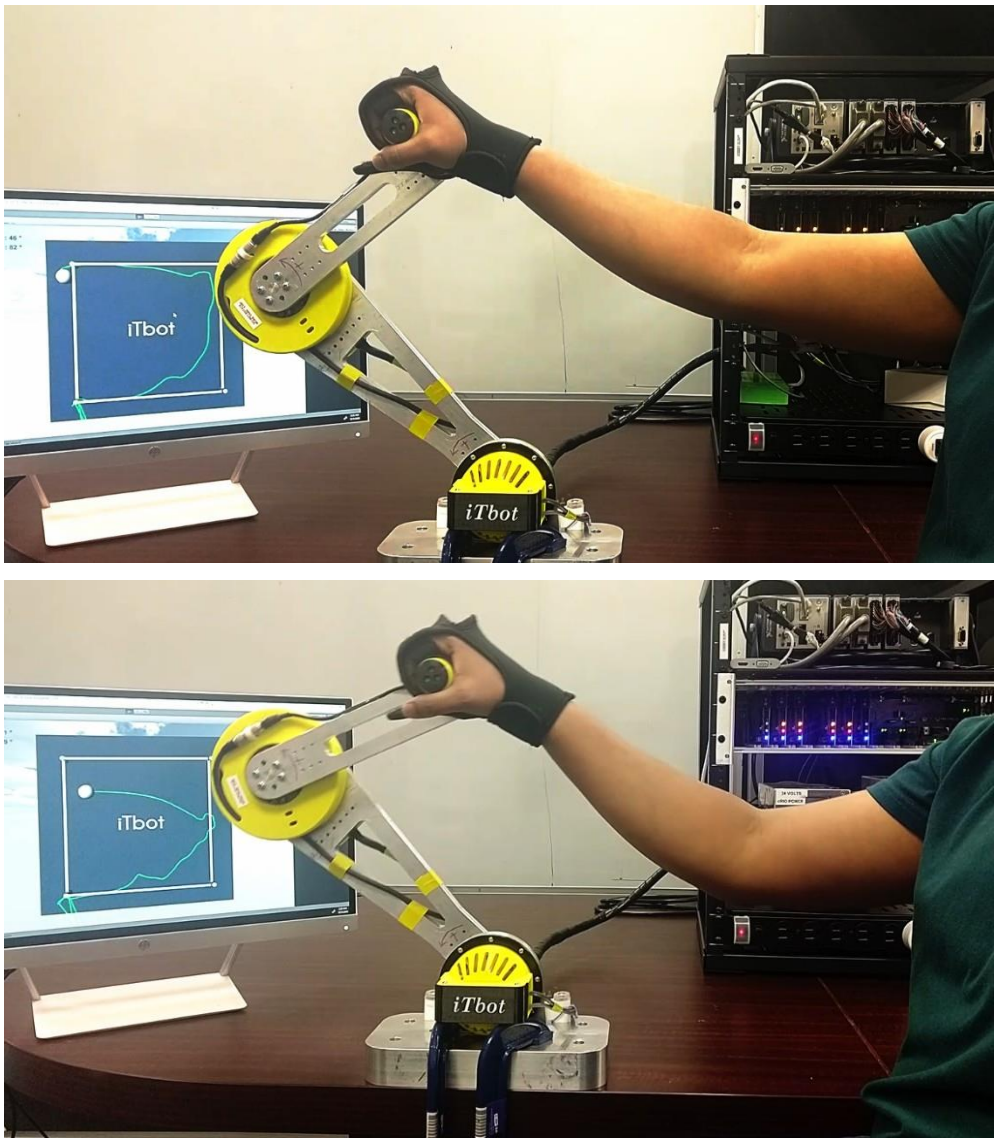

Figure 7.41 Video game based visual feedback during cartesian square trajectory with admittance-based trajectory control enabled in "low admittance" run (top) and "high admittance" run (bottom)

7.2.3 Active-assisted Rehabilitation Exercises:

As the last stage of evaluating the iTbot as a suitable device for robot-aided rehabilitation devices, an active-assisted mode of rehabilitation exercise was formulated. In this exercise, the robot was set in a free run mode where there is no specified trajectory, and the robot uses its current position as the trajectory to try to stay at the same spot. With admittance-based trajectory control enabled, the user can put force on the force sensor through the handle to move the robot around with a varying amount of force based on different admittance gain settings. Additionally, visual feedback provided through a video game interface provides implicit and explicit feedback to the user during the exercise.

In our experimental setup, the iTbot was run in free trajectory mode three times with three different admittance gain settings for testing this scenario. Each time, one test subject, Subject-A, moved around the robot, holding the handle, randomly. The trajectory, motor torque, and force sensor data were recorded during these three runs, along with the subject's upper arm's EMG data. The three test runs can be referred to as "low admittance run," "medium admittance run," and "high admittance run." During the "low admittance run," the admittance gain K was set to K=0.05, 0.02 for Joints 1 and 2 respectively; for the "medium admittance run," the admittance gain K was set to K=0.1, 0.12 for Joints 1 and 2 respectively, and for the "high admittance run" K was set to K=0.3, 0.4 for Joints 1 and 2 respectively. The damping constant C_s was set to 0 for both joints in all cases. The robot was operated with the PID controller for all these runs.

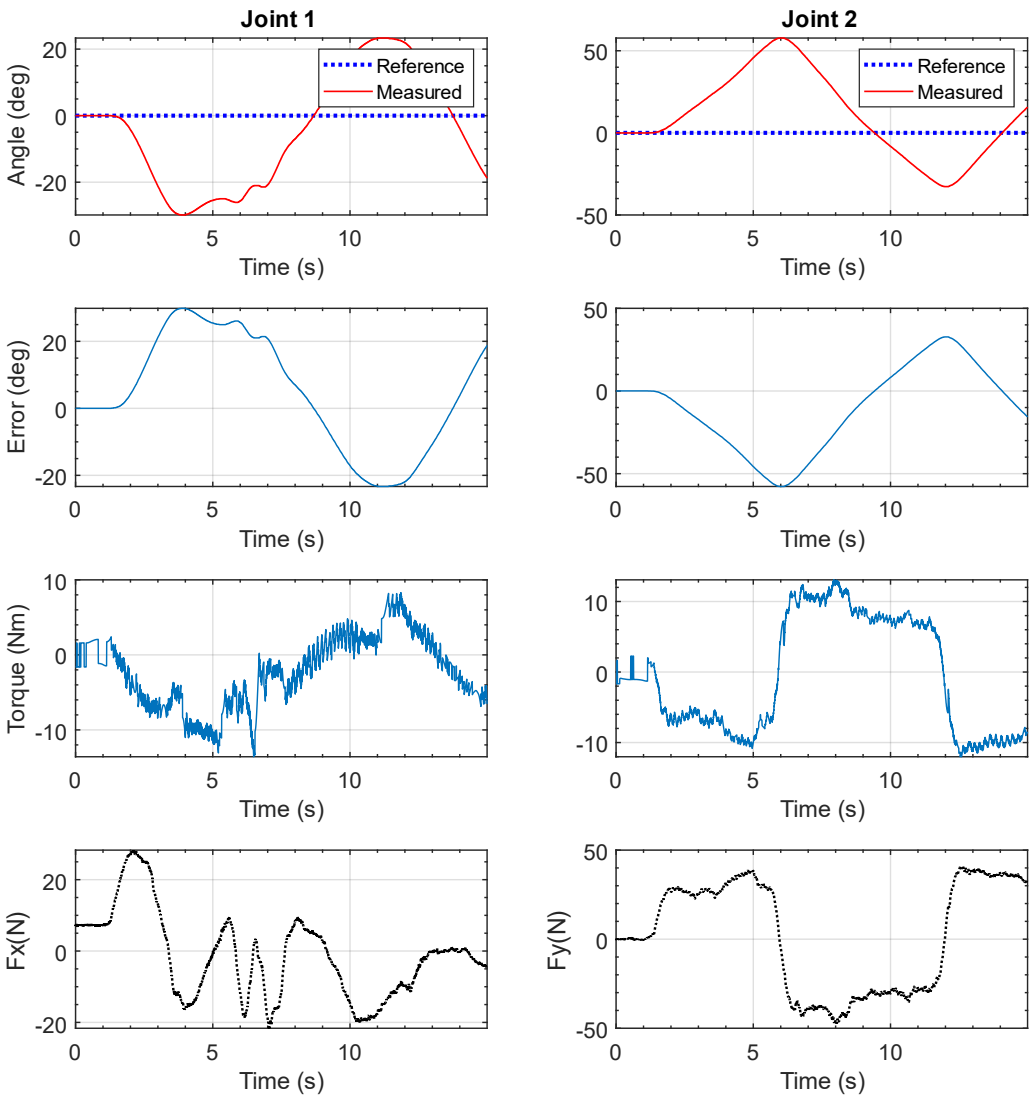

Figure 7.42 Position, Tracking Error, and Torque in joint space along with user's force input data running admittance-based free trajectory in "low admittance" run

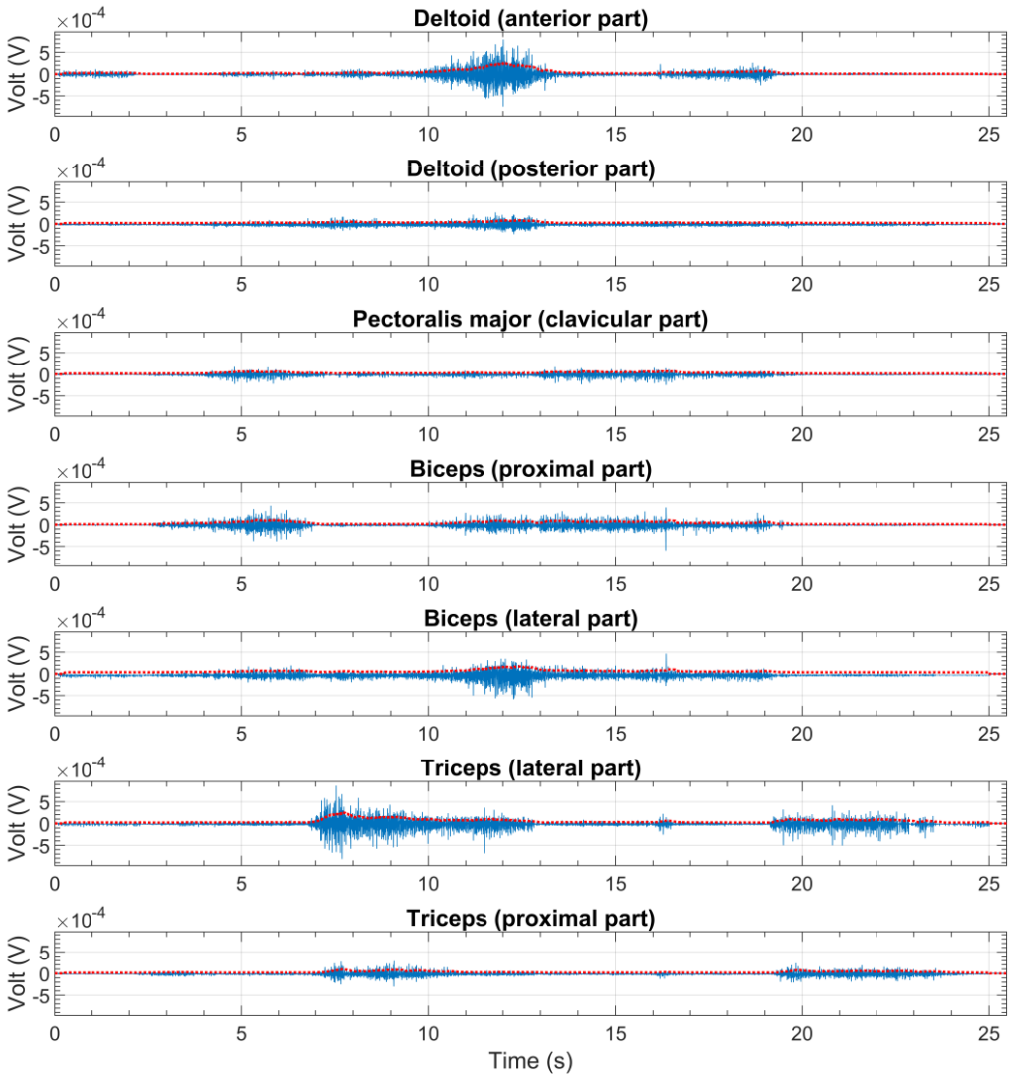

Figure 7.43 User's upper arm muscle activation EMG data during admittance-based free trajectory in "low admittance" run

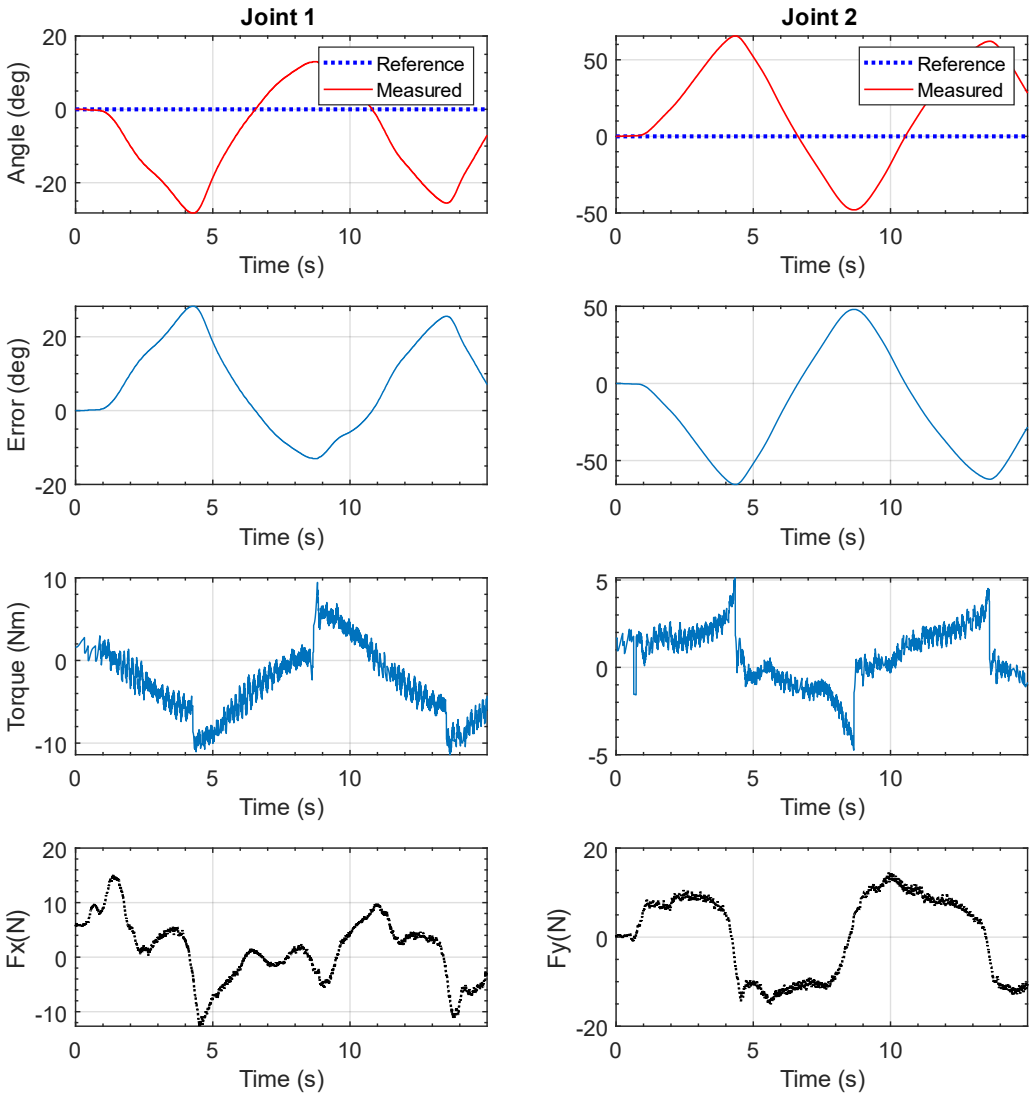

Figure 7.44 Position, Tracking Error, and Torque in joint space along with user's force input data running admittance-based free trajectory in "medium admittance" run

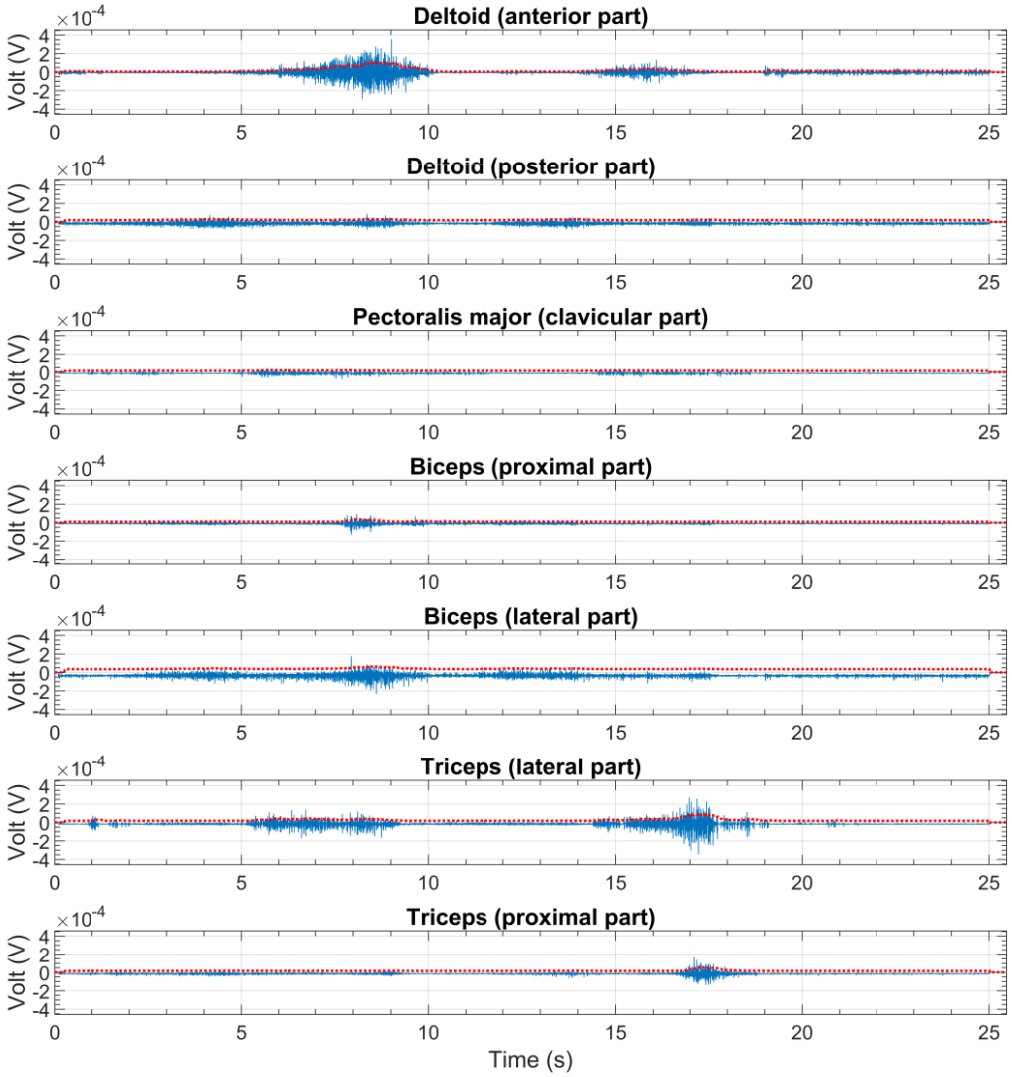

Figure 7.45 User's upper arm muscle activation EMG data during admittance-based free trajectory in "medium admittance" run

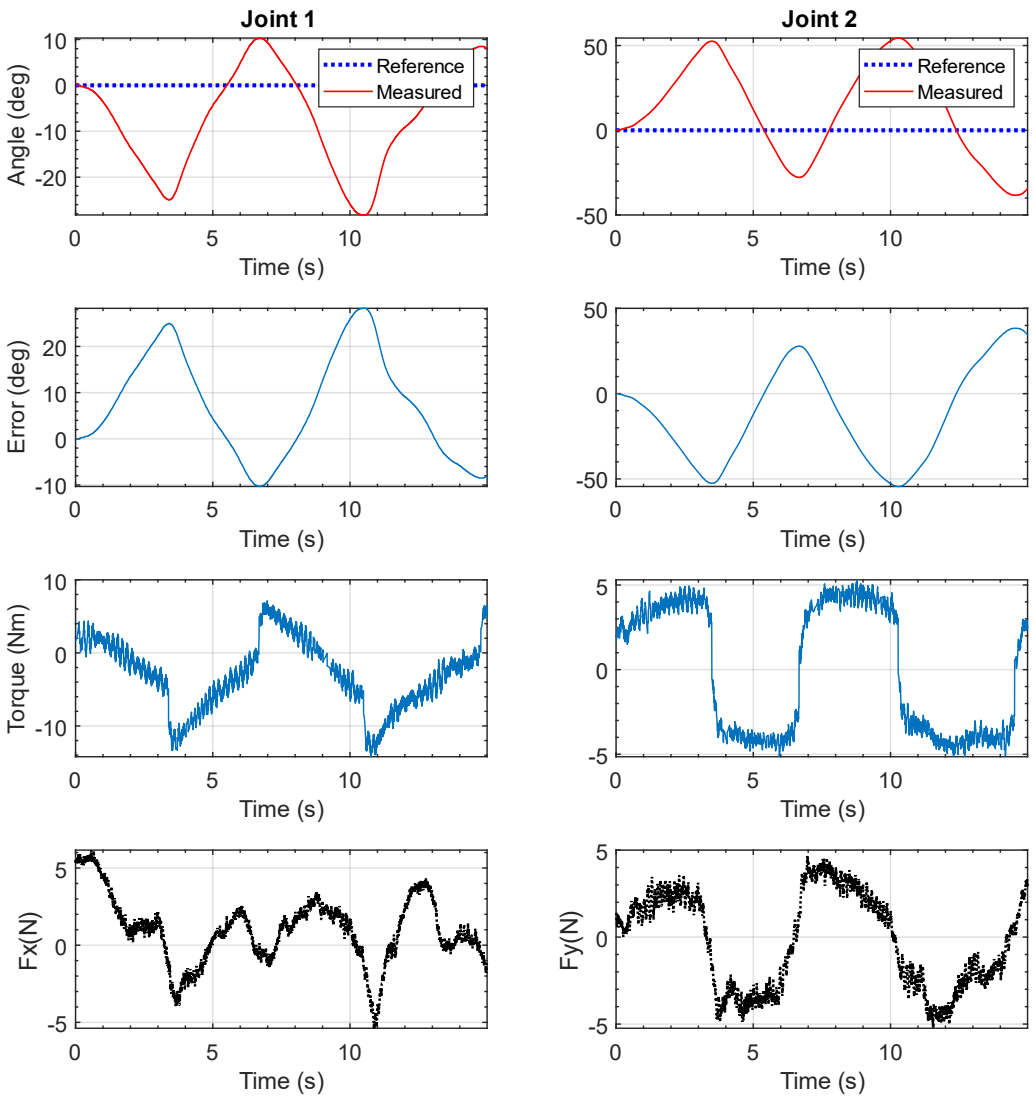

Figure 7.46 Position, Tracking Error, and Torque in joint space along with user's force input data running admittance-based free trajectory in "high admittance" run

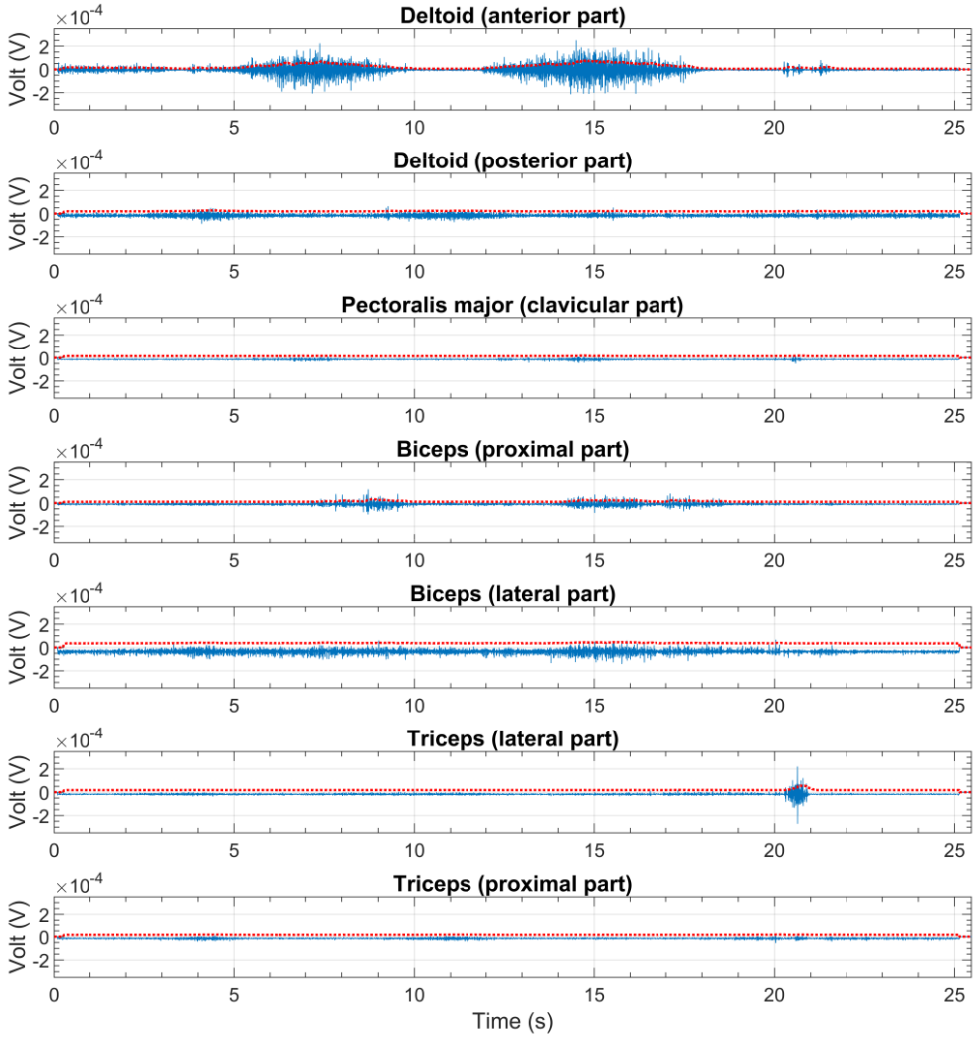

Figure 7.47 User's upper arm muscle activation EMG data during admittance-based free trajectory in "high admittance" run

Observing these results from the three test runs, it is evident that, when admittance is set for low admittance, a higher amount of force is required (±50N) with a higher amount of muscle activation (±500 microvolts range in EMG channels), compared to medium admittance (±20N Force and ±400 microvolts EMG signal) and high admittance (±5N force and ±200 microvolts EMG signal).

The EMG data complements the force sensor data confirming that the higher force readings during low admittance are directly related to the force applied by the user's muscle activation, not force feedback generated from the robot's motion in the force sensor. This concludes the fact that iTbot in active-assisted mode can provide rehabilitation exercises of variable difficulty. Pairing this with exercises designed to require the user to perform specific motions with varying amounts of force would enable robot-aided rehabilitation therapy using multiple principles of motor rehabilitation.

A new scenario was prepared to test goal-based active-assisted therapy with explicit visual feedback as a final test of active-assisted rehabilitation therapy. For this test, the test subject (Subject-A) was now tasked with following a square trajectory based on visual feedback from a video game interface. This test is again run in three different admittance gain settings for low, medium, and high admittance runs. Same admittance gain parameters from the last test were used again for the three different settings.

Figure 7.48 shows snapshots of the experiments being conducted with explicit visual feedback from the video game interface. During the experiment, it is observed that coinciding with the previous test results, in low admittance settings user needs to provide higher physical force, but they can follow the trajectory more accurately. On the other hand, in high admittance mode, they require less effort but tend to drift out of the trajectory easily. *Figure 7.49* shows the user's actual motion in a cartesian space, which confirms that in low admittance mode, the path drawn by the user is more square-shaped than the other two runs. This observation helps conclude that with the change of admittance settings, it is possible to vary both the exercise's physical and neuromotor difficulty. *Figure 7.50, Figure 7.51,* and *Figure 7.52* show the robot controller performance along with the force sensor input for these three test runs.

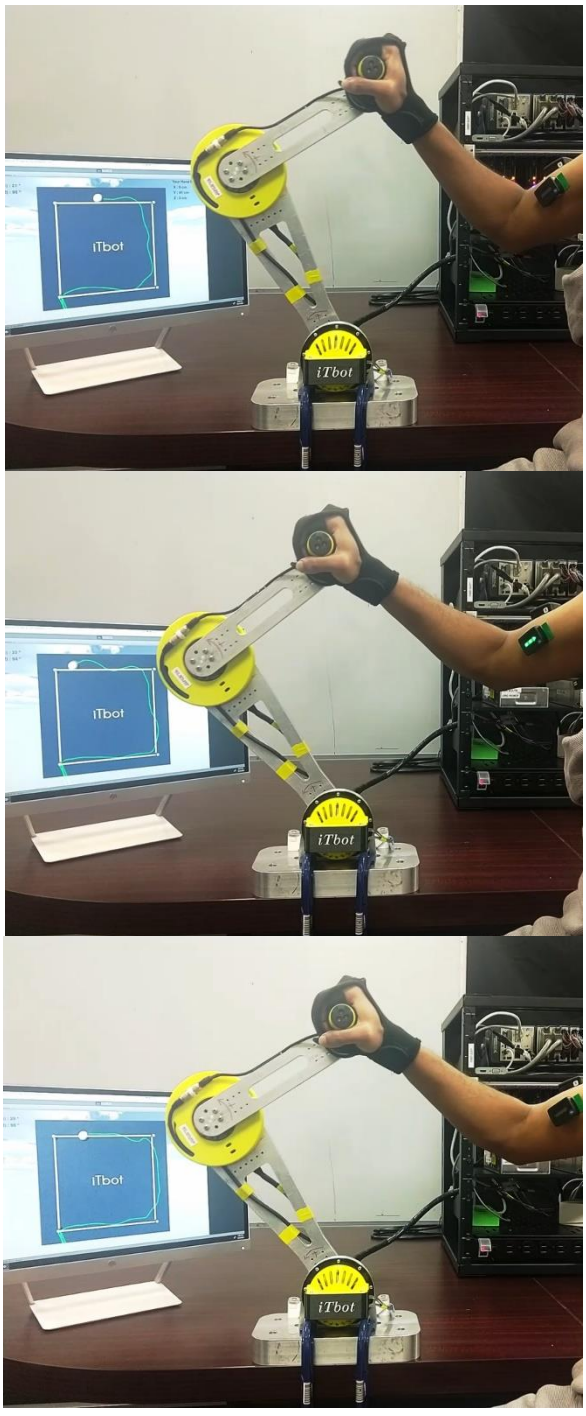

Figure 7.48 Goal based active-assisted exercise with explicit visual feedback during admittance-based free trajectory in "low admittance" run (top), "medium admittance" run (middle) and "high admittance" run (bottom)

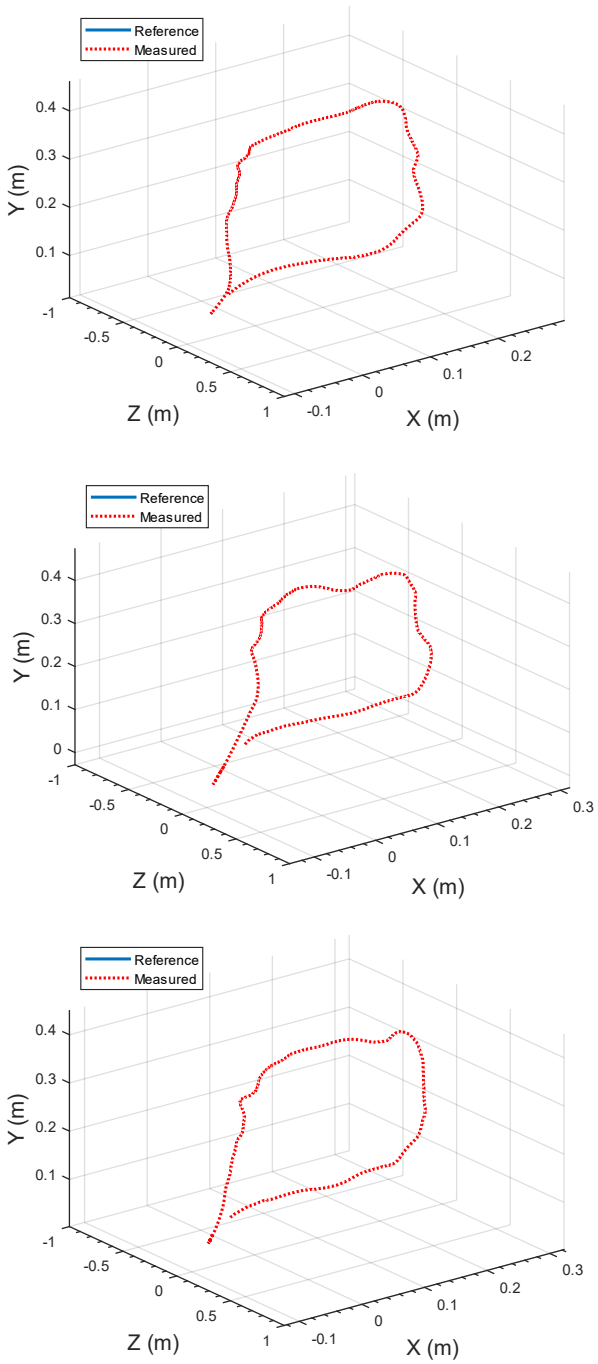

Figure 7.49 Goal based active-assisted exercise with user performance data cartesian representation for admittance-based free trajectory in "low admittance" run (top), "medium admittance" run (middle) and "high admittance" run (bottom)

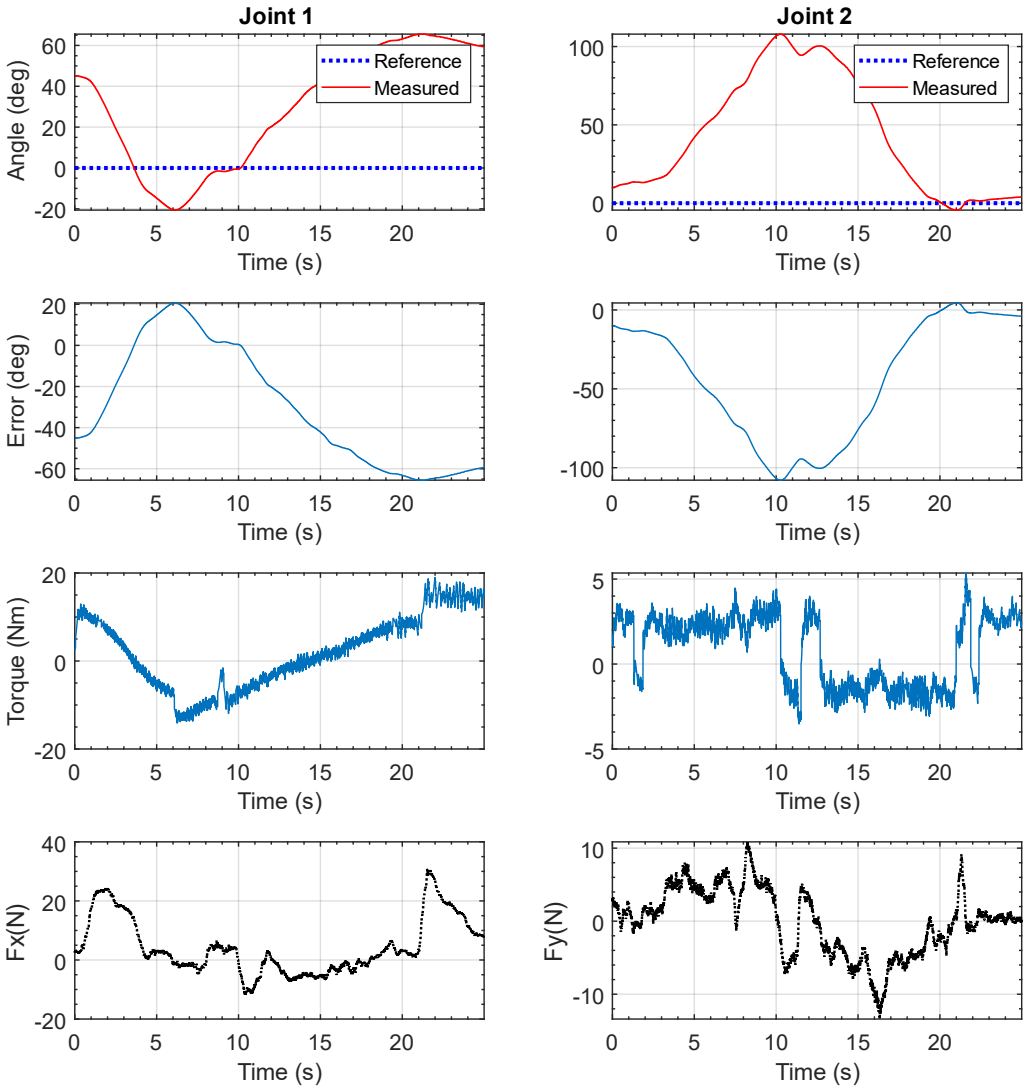

Figure 7.50 Position, Tracking Error, and Torque in joint space along with user's force input data running goal based active-assisted exercise in "low admittance" run

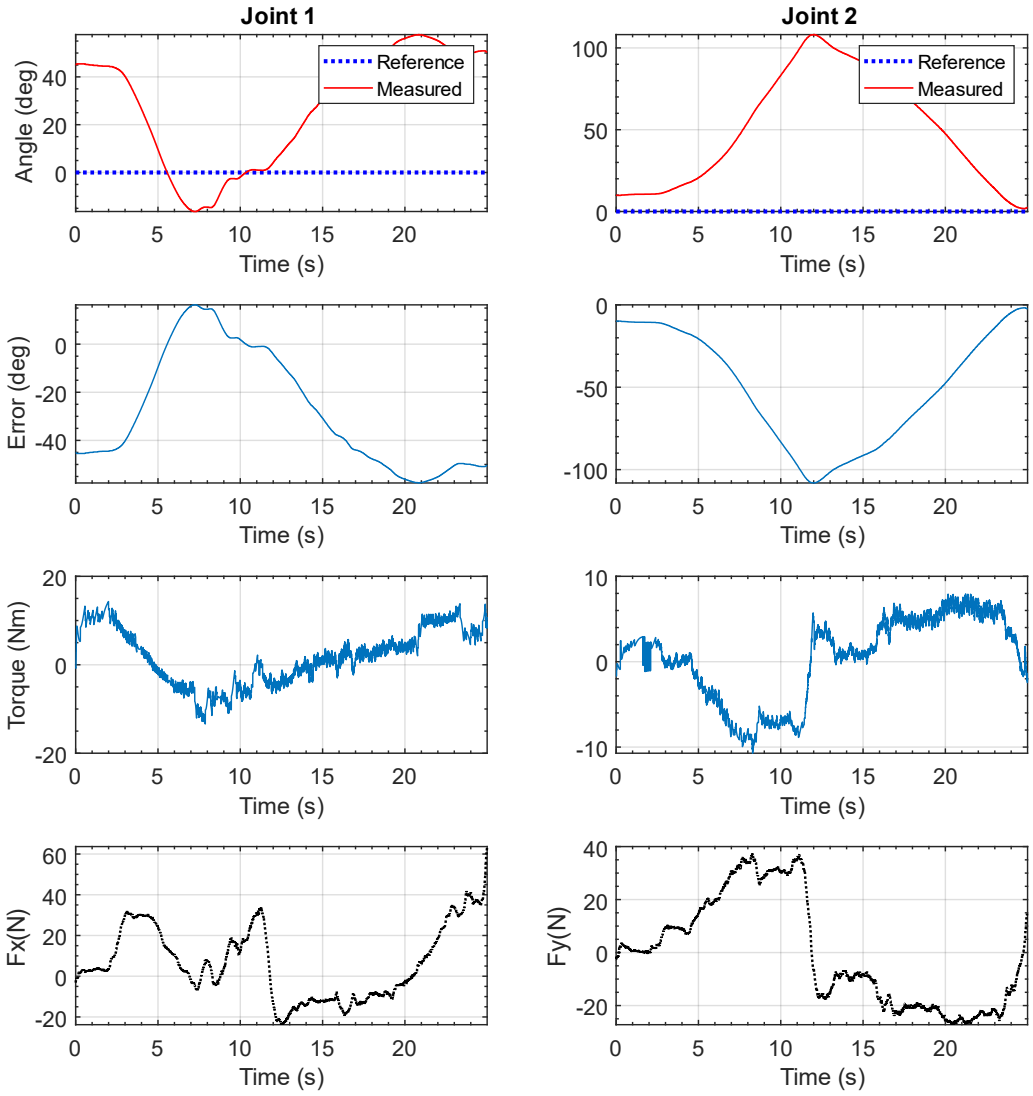

Figure 7.51 Position, Tracking Error, and Torque in joint space along with user's force input data running goal based active-assisted exercise in "medium admittance" run

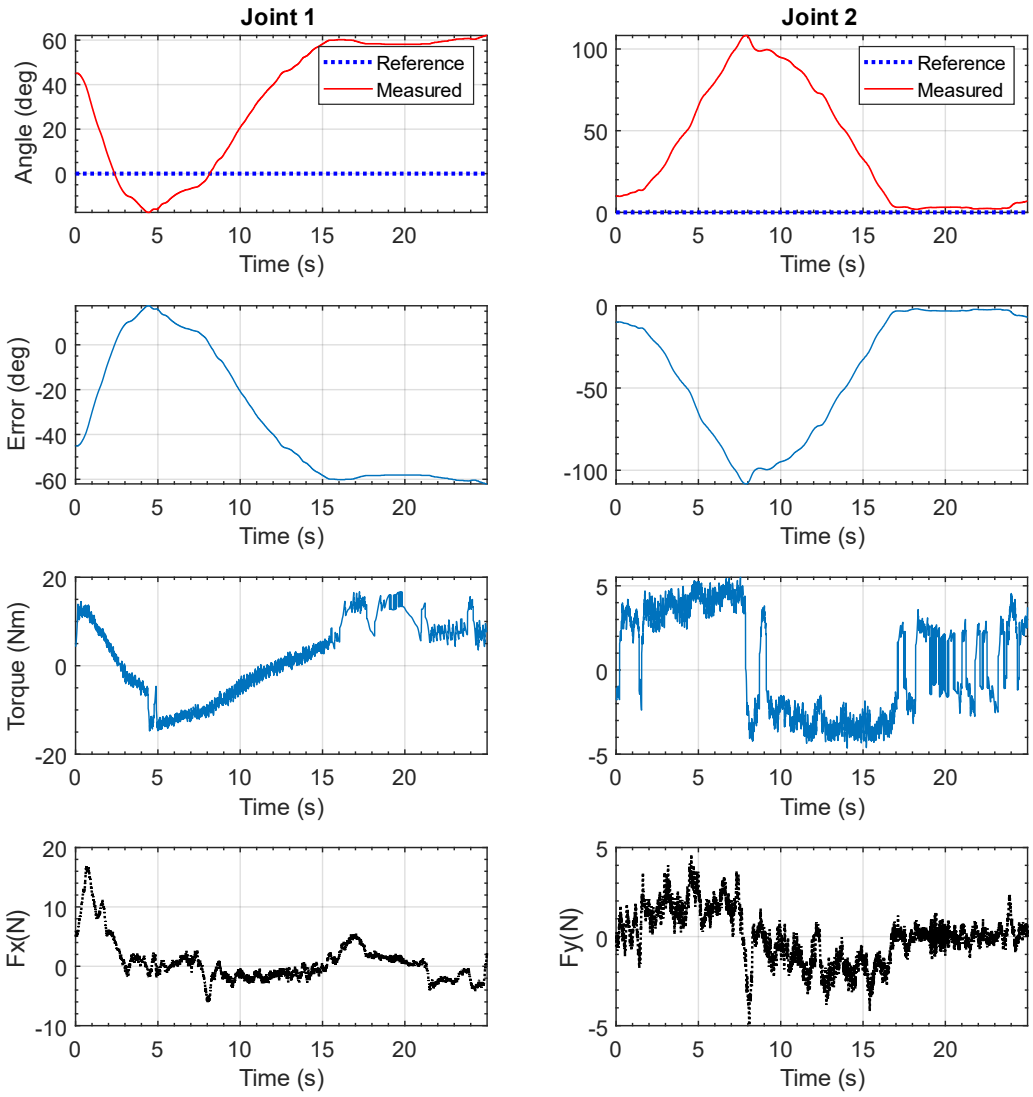

Figure 7.52 Position, Tracking Error, and Torque in joint space along with user's force input data running goal based active-assisted exercise in "high admittance" run

The experimental results in this chapter thus revealed that the developed iTbot and the proposed controllers can effectively provide multi-joint upper limb exercises, including passive, active, active-assistive, and resistive exercises.

CHAPTER 8

CONCLUSIONS AND FUTURE WORK

8.1 Conclusions

In this research, a simplistic 2 DoF robotic rehabilitation device was designed and developed to provide passive, active, and active-assistive rehabilitation exercise to individuals with upper limb impairment. To enable the rehabilitation exercise with this robot, the robot's forward and inverse kinematic model was developed using geometric methods, and the dynamic model was computed iteratively using Newton's and Euler's equations. The robot was configured to operate using non-model-driven control algorithms like PID, as well as model-driven control algorithms (i.e., Modified Computed Torque Control and newly developed Sliding Mode control with Innovative Reaching Law). An admittance-based trajectory modifier was implemented in the robot's control scheme to enable active and active assistive modes of operations. To allow action observation-based rehabilitation, the robot was configured with record and replay mode where admittance-based control can be used to effortlessly move the robot and record the exercise trajectory to be executed later. To provide implicit and explicit feedback during exercise, a video game interface was developed to show the user's performance and goals on screen. In the end, the robot's capabilities to provide robot-aided rehabilitation therapy following the principles of motor rehabilitation was evaluated by designing and completing various passive, active, and active assistive rehabilitation exercises by two healthy individuals acting as test subjects.

8.2 Future work

To further develop the possibility of robot-aided rehabilitation using simple robotic devices like iTbot, following future research works can be performed,

- Fine-tuning the model-based control algorithms to provide a smoother and more comfortable motion of the robot
- Developing low-cost components to replace the robot's gear reducer units to make such a robot more affordable to the users
- Using more 3D printed or rapid prototyped parts in the robot's design to make it more affordable and accessible to people around the world
- Introducing AI-based rehabilitation programs in the robot's software facilitates long-term rehabilitation therapy with less effort from healthcare professionals.

REFERENCES

[1] V. M. Parker, D. T. Wade and R. L. Hewer, "Loss of arm function after stroke: measurement, frequency, and recovery," *Int Rehabil Med,* vol. 8, no. 2, p. 69–73, 1986.

[2] J. Mackay and G. Mensah, "Atlas of Heart Disease and Stroke.," UK: World Health Organization, Brighton, 2004.

[3] P. A. Heidenreich, J. G. Trogdon, O. A. Khavjou, J. Butler, K. Dracup, M. D. Ezekowitz, E. A. Finkelstein, Y. Hong, S. C. Johnston, A. Khera, D. M. Lloyd-jones, S. A. Nelson, G. Nichol, D. Orenstein, P. W. F. Wilson and Y. J. Woo, "Forecasting the Future of Cardiovascular Disease in the United States," *Circulation,* 2011.

[4] C. C. Dodson and F. A. Cordasco, "Anterior glenohumeral joint dislocations," *Orthop Clin North Am,* vol. 39, no. vii, pp. 507-518, 2008.

[5] J. Marty, B. Porcher and R. Autissier, "Hand injuries and occupational accidents. Statistics and prevention.," *Ann Chir Main,* vol. 2, no. 4, p. 368–70, 198.

[6] S. M. Hatem, G. Saussez, F. M. Della, V. Prist, X. Zhang, D. Dispa and Y. Bleyenheuft, "Rehabilitation of Motor Function after Stroke: A Multiple Systematic Review Focused on Techniques to Stimulate Upper Extremity Recovery," *Front Hum Neurosci,* vol. 10, p. 442, 2016.

[7] V. S. Huang, R. Shadmehr and J. Diedrichsen, "Active Learning: Learning a Motor Skill Without a Coach," *Journal of Neurophysiology,* 2008.

[8] C. J. Winstein, A. S. Merians and K. J. Sullivan, "Motor learning after unilateral brain damage," *Neuropsychologia,* vol. 37, pp. 975-987, 1999.

[9] C. J. Winstein, J. P. Miller, S. Blanton, E. Taub, G. Uswatte, D. Morris, D. Nichols and a. S. Wolf, "Methods for a multisite randomized trial to investigate the effect of constraint-induced movement therapy in improving upper extremity function among adults recovering from a cerebrovascular stroke.," *Neurorehabil Neural Repair,* pp. 137-152, 2003.

[10] M. Rahman, K. Kiguchi, M. M. Rahman and M. Sasaki, "Robotic Exoskeleton for Rehabilitation and Motion Assist," in *First International Conference on Industrial and Information Systems,* 2006.

[11] M. H. Rahman, M. J. Rahman, O. L. Cristobal, M. Saad, J. P. Kenné and P. S. Archambault, "Development of a whole arm wearable robotic exoskeleton for rehabilitation and to assist upper limb movements," *Robotica,* 2014.

[12] T. Nef, M. Guidali and R. Riener, "ARMin III ; Arm Therapy Exoskeleton with an Ergonomic Shoulder Actuation," *Applied Bionics and Biomechanics,* 2009.

[13] H. M. Kim, T. K. Hong and G. S. Kim, "Design of a wrist rotation rehabilitation robot," in *International Conference on Cyber Technology in Automation, Control and Intelligent*, Hong Kong, 2014.

[14] H. I. Krebs, B. T. Volpe, D. Williams, J. Celestino, S. K. Charles, D. Lynch and N. Hogan, "Robot-Aided Neurorehabilitation: A Robot for Wrist Rehabilitation," *IEEE Transactions on Neural Systems and Rehabilitation Engineering,* vol. 15, pp. 327-335, 2007.

[15] G. C. Burgar, P. Lum, M. A Scremin, S. Garber, M. Van Der Loos, D. Kenney and P. C Shor, "Robot-assisted upper-limb therapy in acute rehabilitation setting following stroke: Department of Veterans Affairs multisite clinical trial.," *J Rehabil Res Dev,* vol. 48, pp. 445-458, 2011.

[16] S. Hesse, G. Schulte-tigges, M. Konrad, A. Bardeleben and C. Werner, "Robot-assisted arm trainer for the passive and active practice of bilateral forearm and wrist movements in hemiparetic subjects," *Arch Phys Med Rehabil,* 2003.

[17] T. Nef, M. Guidali, V. Klamroth-marganska and R. Riener, "ARMin - Exoskeleton Robot for Stroke Rehabilitation," in *World Congress on Medical Physics and Biomedical Engineering*, 2009.

[18] B. Kim and A. D. Deshpande, "An upper-body rehabilitation exoskeleton Harmony with an anatomical shoulder mechanism: Design, modeling, control, and performance evaluation.," *The International Journal of Robotics Research,* vol. 36, 2017.

[19] T. Nef, M. Mihelj, G. Kiefer, C. Perndl, R. Muller and R. Riener, "ARMin - Exoskeleton for Arm Therapy in Stroke Patients.," in *IEEE 10th International Conference on Rehabilitation Robotics*, 2007.

[20] T. Madani, B. Daachi and K. Djouani, "Modular-Controller-Design-Based Fast Terminal Sliding Mode for Articulated Exoskeleton Systems," *IEEE Transactions on Control Systems Technology,* vol. 25, pp. 1133-1140, 2017.

[21] M. K. Sharma and R. Ordonez, "Design and fabrication of an intention based upper-limb exo-skeleton," in *IEEE International Symposium on Intelligent Control (ISIC)*, 2016.

[22] M. H. Rahman, T. K. Ouimet, M. Saad, J. P. Kenné and P. S. Archambault, "Development and control of a wearable robot for rehabilitation of elbow and shoulder joint movements," in *IECON 2010 - 36th Annual Conference on IEEE Industrial Electronics Society*, 2010.

[23] S. Balasubramanian, W. Ruihua, M. S. B. Perez, E. Koeneman, J. Koeneman and H. Jiping, "RUPERT: An exoskeleton robot for assisting rehabilitation of arm functions," in *Virtual Rehabilitation*, 2008.

[24] T. G. Sugar, J. He, E. J. Koeneman, J. B. Koeneman, R. Herman, H. Huang, R. S. Schultz, D. E. Herring, J. Wanberg, S. Balasubramanian, P. Swenson and J. A. Ward, "Design and Control of RUPERT: A Device for Robotic Upper Extremity Repetitive Therapy.," *IEEE Transactions on Neural Systems and Rehabilitation Engineering*, vol. 15, pp. 336-346, 2007.

[25] J. Garrido, W. Yu and X. Li, "Modular design and control of an upper limb exoskeleton," *Journal of Mechanical Science and Technology*, vol. 30, pp. 2265-2271, 2016.

[26] Z. Li, Z. Huang, W. He and C. Y. Su, "Adaptive Impedance Control for an Upper Limb Robotic Exoskeleton Using Biological Signals," *IEEE Transactions on Industrial Electronics*, vol. 64, pp. 1664-1674, 2017.

[27] K. D. Fitle, A. U. Pehlivan and M. K. O. Malley, "A robotic exoskeleton for rehabilitation and assessment of the upper limb following incomplete spinal cord injury," in *IEEE International Conference on Robotics and Automation (ICRA)*, 2015.

[28] J. A. French, C. G. Rose and M. K. O'malley, "System Characterization of MAHI Exo-II: A Robotic Exoskeleton for Upper Extremity Rehabilitation," in *Dynamic Systems and Control Conference*, 2014.

[29] M. Gunasekara and R. &. J. S. Gopura, "6-REXOS: Upper Limb Exoskeleton Robot with Improved pHRI.," *International Journal of Advanced Robotic Systems*, vol. 12, p. 47, 2015.

[30] A. Frisoli, F. Salsedo, M. Bergamasco, B. Rossi and M. C. Carboncini, "A Force-Feedback Exoskeleton for Upper-Limb Rehabilitation in Virtual Reality.," *Applied Bionics and Biomechanics*, vol. 6, 2009.

[31] G. R. Johnson, D. A. Carus, G. Parrini, S. Marchese and R. Valeggi, "The design of a five-degree-of-freedom powered orthosis for the upper limb.," *Proceedings of the Institution of Mechanical Engineers, Part H: Journal of Engineering in Medicine,* vol. 215, pp. 275-284, 2001.

[32] M. H. Rahman, T. K. Ouimet, M. Saad, J. P. Kenné and P. S. Archambault, "Development and Control of a Robotic Exoskeleton for Shoulder, Elbow and Forearm Movement Assistance.," *Applied Bionics and Biomechanics,* vol. 9, 2012.

[33] C. Carignan, J. Tang, S. Roderick and M. A. Naylor, "Configuration-Space Approach to Controlling a Rehabilitation Arm Exoskeleton," in *IEEE 10th International Conference on Rehabilitation Robotics*, 2007.

[34] R. Sanchez, D. Reinkensmeyer, P. Shah, J. Liu, S. Rao, R. Smith, S. Cramer, T. Rahman and J. Bobrow, "Monitoring functional arm movement for home-based therapy after stroke.," in *The 26th Annual International Conference of the IEEE Engineering in Medicine and Biology Society*, 2004.

[35] S. Balasubramanian and J. He, "Adaptive Control of a Wearable Exoskeleton for Upper-Extremity Neurorehabilitation," in *Applied Bionics and Biomechanics*, 2012.

[36] A. Gupta and M. K. O. Malley, "Design of a haptic arm exoskeleton for training and rehabilitation.," *IEEE/ASME Transactions on Mechatronics,* vol. 11, pp. 280-289, 2006.

[37] B. O. Mushage, J. C. Chedjou and K. Kyamakya, "Fuzzy neural network and observer-based fault-tolerant adaptive nonlinear control of uncertain 5-DOF upper-limb exoskeleton robot for passive rehabilitation," *Nonlinear Dynamics,* vol. 87, pp. 2021-2037, 2017.

[38] H. B. Kang and J. H. Wang, "Adaptive robust control of 5 DOF Upper-limb exoskeleton robot," *International Journal of Control, Automation and Systems,* vol. 13, pp. 733-741, 2015.

[39] L. Pignolo, G. Dolce, G. Basta, L. F. Lucca, S. Serra and W. G. Sannita, "Upper limb rehabilitation after stroke: ARAMIS a “robo-mechatronic” innovative approach and prototype," in *4th IEEE RAS & EMBS International Conference on Biomedical Robotics and Biomechatronics (BioRob)*, 2012.

[40] M. Guidali, A. Duschau-wicke, S. Broggi, V. Klamroth-marganska, T. Nef and R. Riener, "A robotic system to train activities of daily living in a virtual environment.," *Medical & Biological Engineering & Computing,* vol. 49, p. 1213, 2011.

[41] Y. Chen, J. Fan, Y. Zhu, J. Zhao and H. Cai, "A passively safe cable driven upper limb rehabilitation exoskeleton," *Technology and Health Care,* vol. 23, 2015.

[42] F. Xiao, Y. Gao, Y. Wang, Y. Zhu and J. Zhao, "Design of a wearable cable-driven upper limb exoskeleton based on epicyclic gear trains structure.," *Technol Health Care,* vol. 25, pp. 3-11, 2017.

[43] J. C. Perry, J. Rosen and S. Burns, "Upper-Limb Powered Exoskeleton Design.," *IEEE/ASME Transactions on Mechatronics,* vol. 12, pp. 408-417, 2007.

[44] N. G. Tsagarakis and D. G. Caldwell, "Development and Control of a 'Soft-Actuated' Exoskeleton for Use in Physiotherapy and Training.," *Autonomous Robots,* vol. 15, pp. 21-33, 2003.

[45] R. A. R. C. Gopura, K. Kiguchi and Y. Li, "SUEFUL-7: A 7DOF upper-limb exoskeleton robot with muscle-model-oriented EMG-based control.," in *IEEE/RSJ International Conference on Intelligent Robots and Systems*, 2009.

[46] L. Liu, Y. Y. Shi and L. Xie, "A novel multi-dof exoskeleton robot for upper limb rehabilitation.," *Journal of Mechanics in Medicine and Biology,* vol. 16, 2016.

[47] X. Cui, W. Chen, X. Jin and S. K. Agrawal, "Design of a 7-DOF Cable-Driven Arm Exoskeleton (CAREX-7) and a Controller for Dexterous Motion Training or Assistance.," *IEEE/ASME Transactions on Mechatronics,* vol. 22, pp. 161-172, 2017.

[48] H. &. K. J. Kim, "Control of the seven-degree-of-freedom upper limb exoskeleton for an improved human-robot interface.," *Journal of the Korean Physical Society,* vol. 70, pp. 726-734, 2017.

[49] N. Hogan, H. I. Krebs, J. Charnnarong, P. Srikrishna and A. Sharon, "MIT-MANUS: a workstation for manual therapy and training.," in *Proceedings IEEE International Workshop on Robot and Human Communication*, 1992.

[50] F. J. Badesa, R. Morales, N. Garcia-aracil, J. M. Sabater, A. Casals and L. Zollo, "Auto-adaptive robot-aided therapy using machine learning techniques.," *Computer Methods and Programs in Biomedicine,* vol. 116, pp. 123-130, 2014.

[51] J. J. Chang, W. L. Tung, W. L. Wu, M. H. Huang and F. C. Su, "Effects of Robot-Aided Bilateral Force-Induced Isokinetic Arm Training Combined With Conventional Rehabilitation on Arm Motor Function in Patients With Chronic Stroke.," *Archives of Physical Medicine and Rehabilitation,* vol. 88, pp. 1332-1338, 2007.

[52] D. Campolo, P. Tommasino, K. Gamage, J. Klein, C. M. L. Hughes and L. Masia, "H-Man: A planar, H-shape cabled differential robotic manipulandum for experiments on human motor control," *Journal of Neuroscience Methods,* vol. 235, pp. 285-297, 2014.

[53] A. Hussain, A. Budhota, C. M. L. Hughes, W. D. Dailey, D. A. Vishwanath, C. W. K. Kuah, L. H. L. Yam, Y. J. Loh, L. Xiang, K. S. G. Chua, E. Burdet and D. Campolo, "Self-Paced Reaching after Stroke: A Quantitative Assessment of Longitudinal and Directional Sensitivity Using the H-Man Planar Robot for Upper Limb Neurorehabilitation.," *Frontiers In Neuroscience,* vol. 10, 2016.

[54] A. Hussain, W. Dailey, C. Hughes, A. Budhota, W. G. K. C. Gamage, D. A. Vishwanath, C. Kuah, K. Chua, E. Burdet and D. Campolo, "Quantitative motor assessment of upperlimb after unilateral stroke: A preliminary feasibility study with H-Man, a planar robot.," in *2015 IEEE International Conference on Rehabilitation Robotics (ICORR),* 2015.

[55] R. Colombo, F. Pisano, S. Micera, A. Mazzone, C. Delconte, M. C. Carrozza, P. Dario and G. Minuco, "Assessing Mechanisms of Recovery During Robot-Aided Neurorehabilitation of the Upper Limb.," *Neurorehabilitation and Neural Repair,* vol. 22, pp. 50-63, 2007.

[56] X. L. Hu, K. Y. Tong, R. Song, X. J. Zheng, K. H. Lui, W. W. F. Leung, S. Ng and S. S. Y. Au-yeung, "Quantitative evaluation of motor functional recovery process in chronic stroke patients during robot-assisted wrist training.," *Journal of Electromyography and Kinesiology,* vol. 19, pp. 639-650, 2009.

[57] C. T. Freeman, A. M. Hughes, J. H. Burridge, P. H. Chappell, P. L. Lewin and E. Rogers, "A robotic workstation for stroke rehabilitation of the upper extremity using FES.," *Medical Engineering and Physics,* vol. 31, pp. 364-373, 2009.

[58] D. J Reinkensmeyer, L. E Kahn, M. Averbuch, A. N. Mckenna-cole, B. Schmit and W. Rymer, "Understanding and treating arm movement impairment after chronic brain injury: Progress with the ARM Guide.," *The Journal of Rehabilitation Research and Development,* vol. 37, pp. 653-662, 2000.

[59] G. Rosati, P. Gallina and S. Masiero, "Design, Implementation and Clinical Tests of a Wire-Based Robot for Neurorehabilitation.," *IEEE Transactions on Neural Systems and Rehabilitation Engineering,* vol. 15, pp. 560-569, 2007.

[60] M. Stefano, P. Patrizia, A. Mario, G. Ferlini, R. Rizzello and G. Rosati, "Robotic Upper Limb Rehabilitation after Acute Stroke by NeReBot: Evaluation of Treatment Costs.," *BioMed Research International,* 2014.

[61] M. Takaiwa and T. Noritsugu, "Development of wrist rehabilitation equipment using pneumatic parallel manipulator -Acquisition of P.T.'s motion and its execution for patient.," in *2009 IEEE International Conference on Rehabilitation Robotics*, 2009.

[62] M. Takaiwa and T. Noritsugu, "Wrist rehabilitaion equipment using pneumatic parallel manipulator.," in *2010 World Automation Congress*, 2010.

[63] P. Lum, C. G Burgar, M. Van Der Loos, P. C Shor, M. Majmundar and R. Yap, "MIME robotic device for upper-limb neurorehabilitation in subacute stroke subjects: A follow-up study," *J Rehabil Res Dev,* 2006.

[64] P. S. Lum, C. G. Burgar, P. C. Shor, M. Majmundar and M. Van Der Loos, "Robot-assisted movement training compared with conventional therapy techniques for the rehabilitation of upper-limb motor function after stroke.," *Archives of Physical Medicine and Rehabilitation,* vol. 83, pp. 952-959, 2002.

[65] F. Amirabdollahian, R. Loureiro, E. Gradwell, C. Collin, W. Harwin and G. Johnson, "Multivariate analysis of the Fugl-Meyer outcome measures assessing the effectiveness of GENTLE/S robot-mediated stroke therapy.," *Journal of NeuroEngineering and Rehabilitation,* vol. 4, 2007.

[66] S. Coote, B. Murphy, W. Harwin and E. Stokes, "The effect of the GENTLE/s robot-mediated therapy system on arm function after stroke.," *Clinical Rehabilitation,* vol. 22, pp. 395-405, 2008.

[67] A. Umemura, Y. Saito and K. Fujisaki, "A study on power-assisted rehabilitation robot arms operated by patient with upper limb disabilities.," in *2009 IEEE International Conference on Rehabilitation Robotics,* 2009.

[68] A. Toth, G. Fazekas, G. Arz, M. Jurak and M. Horvath, "Passive robotic movement therapy of the spastic hemiparetic arm with REHAROB: report of the first clinical test and the follow-up system improvement.," in *9th International Conference on Rehabilitation Robotics, 2005 (ICORR 2005)*, 2005.

[69] J. Karges and S. Smallfield, "A description of the outcomes, frequency, duration, and intensity of occupational, physical, and speech therapy in inpatient stroke rehabilitation," *Journal of allied health,* vol. 38, no. 1, pp. E1-10, 2009.

[70] J.-A. Mills, E. Marks, T. Reynolds and A. Cieza., "Chapter 15 Rehabilitation: Essential along the Continuum of Care," in *Disease Control Priorities: Improving Health and Reducing Poverty. 3rd edition.,* 2018.

[71] P. Voss, M. E. Thomas, J. M. Cisneros-Franco and É. de Villers-Sidani, "Dynamic Brains and the Changing Rules of Neuroplasticity: Implications for Learning and Recovery.," *Frontiers in Psychology*, 2017.

[72] J. A. Kleim and T. A. Jones, "Principles of experience-dependent neural plasticity: Implications for rehabilitation after brain damage," *Journal of Speech, Language, and Hearing Research*, 2008.

[73] M. Maier, B. R. Ballester and P. F. M. J. Verschure, "Principles of neurorehabilitation after stroke based on motor learning and brain plasticity mechanisms," *Frontiers in Systems Neuroscience*, 2019.

[74] R. A. Schmidt, T. D. Lee, J. W. Carolee, W. Gabriele and N. Z. Howard, Motor Control and Learning: A Behavioral Emphasis, Champaign, IL: Human Kinetics, 2019.

[75] G. Kwakkel, J. M. Veerbeek, E. E. H. Van Wegen and S. L. Wolf, "Constraint-induced movement therapy after stroke," *The Lancet. Neurology*, vol. 14, pp. 224-234, 2015.

[76] P. Poli, G. Morone, G. Rosati and S. Masiero, "Robotic technologies and rehabilitation: new tools for stroke patients' therapy," *BioMed Research International*, 2013.

[77] N. J. Cepeda, H. Pashler, E. Vul, J. T. Wixted and D. Rohrer, "Distributed practice in verbal recall tasks: A review and quantitative synthesis," *Psychological Bulletin*, vol. 132, pp. 354-380, 2006.

[78] T. Savion-lemieux and V. B. Penhune, "The effects of practice and delay on motor skill learning and retention," *Experimental Brain Research*, 2005.

[79] G. Kwakkel, "Intensity of practice after stroke: More is better.," *Schweizer Archiv fur Neurologie und Psychiatrie*, 2009.

[80] G. Kwakkel, R. v. Peppen, R. C. Wagenaar, S. W. Dauphinee, C. Richards, A. Ashburn, K. Miller, N. Lincoln, C. Partridge, I. Wellwood and P. Langhorne, "Effects of Augmented Exercise Therapy Time After Stroke," *Stroke* , 2004.

[81] R. A. Schmidt and T. D. and Lee, Motor Control and Learning: A Behavioral Emphasis, Champaign, IL: Human Kinetics, 2011.

[82] S. Gauggel and S. and Fischer, " The effect of goal setting on motor performance and motor learning in brain-damaged patients," *Neuropsychol. Rehabil*, 2001.

[83] C. H. Shea and R. M. Kohl, "Composition of Practice: Influence on the Retention of Motor Skills," *Research Quarterly for Exercise and Sport,* 1990.

[84] J. B. Shea and R. L. Morgan, "Contextual interference effects on the acquisition, retention, and transfer of a motor skill.," *Journal of Experimental Psychology: Human Learning and Memory,* 1979.

[85] T. Mulder and J. Hochstenbach, "Adaptability and flexibility of the human motor system: implications for neurological rehabilitation," *Neural Plast,* 2001.

[86] C. D. Wickens, S. Hutchins, T. Carolan and J. Cumming, " Effectiveness of part-task training and increasing-difficulty training strategies: a meta-analysis approach.," *Human Factors,* 2013.

[87] D. C. Knill and A. Pouget, "The Bayesian brain: the role of uncertainty in neural coding and computation.," *Trends in Neurosciences,* 2004.

[88] C. Nombela, L. E. Hughes, A. M. Owen and J. A. Grahn, "Into the groove: can rhythm influence Parkinson's disease?," *Neuroscience & Biobehavioral Reviews,* 2013.

[89] A. W. Salmoni, R. A. Schmidt and C. B. Walter, "Knowledge of results and motor learning: A review and critical reappraisal.," *Psychological Bulletin,* vol. 95, no. 3, pp. 355-386, 1984.

[90] J. A. Taylor, J. W. Krakauer and R. B. Ivry, "Explicit and implicit contributions to learning in a sensorimotor adaptation task," *J. Neurosci,* 2014.

[91] E. Taub, G. Uswatte, V. W. Mark and D. M. M. Morris, "The learned nonuse phenomenon: implications for rehabilitation," *Eura Medicophys,* 2006.

[92] K. Andrews and J. and Stewart, "Stroke recovery: he can but does he?," *Rheumatology,* 1979.

[93] A. A. G. Mattar and P. L. and Gribble, "Motor learning by observing," *Neuron ,* vol. 46, pp. 153-160, 2005.

[94] W. J. Harmsen, J. B. J. Bussmann, R. W. Selles, H. L. P. Hurkmans and G. M. Ribbers, "A mirror therapy-based action observation protocol to improve motor learning after stroke," *Neurorehabilitation and Neural Repair,* 2015.

[95] D. R. Franck, D. Ursula, D. Sébastien, S. Elodie, D. Claude, D. Julien, C. Christian and G. Aymeric, "Online and Offline Performance Gains Following Motor Imagery Practice: A

Comprehensive Review of Behavioral and Neuroimaging Studies," *Frontiers in Human Neuroscience* , vol. 10, p. 315, 2016.

[96] G. Wulf, S. Chiviacowsky and R. Lewthwaite, "Altering mindset can enhance motor learning in older adults," *Psychology and Aging,* 2012.

[97] T. Ahmed, A. A. Z. Swapnil, M. R. Islam, I. Wang and M. Rahman, "An Exoskeleton Based Robotic Device for Providing Rehabilitative Therapies to Human Forearm and Wrist Joints (UWM-FWRR)," *Archives of Physical Medicine and Rehabilitation,* pp. 101-112, 2020.

[98] A. R. Tilley and H. Dreyfuss , The Measure of Man and Woman: Human Factors in Design, New York: Wiley, 2001.

[99] J. Denavit and R. S. Hartenberg, "A Kinematic Notation for Lower-Pair Mechanisms Based on Matrices," *Trans ASME J. Appl. Mech.* , vol. 23, pp. 215-221, 1955.

[100] J. J. Craig, Introduction to Robotics : Mechanics and Control, NJ: Pearson, 2014.

[101] R. S. Hartenberg and J. Denavit, in *Kinematic Synthesis of Linkages*, New York, McGraw-Hill, 1965, p. 435.

[102] J. Y. S. Luh, M. W. Walker and R. P. C. Paul, "On-line computational scheme for mechanical manipulators," *ASME J. of Dynamic Systems, Measurement, and Control,* vol. 102, no. 2, pp. 69-76, 1980.

[103] V. Utkin, J. Guldner and J. Shi, Sliding Mode Control in Electro-Mechanical Systems, London: Boca Raton, 2009.

[104] W. Gao and J. Hung, "Variable structure control of nonlinear systems: A new approach," *IEEE transactions on Industrial Electronics,* 1993.

[105] C. J. Fallaha, M. Saad, H. Y. Kanaan and K. Al-Haddad, "Sliding-mode robot control with exponential reaching law," *IEEE Transactions on Industrial Electronics,* 2011.

[106] C. O. Luna, M. H. Rahman and M. Saad, "Admittance-based Upper Limb Robotic Active and Active-assistive Movements," *International Journal of Advanced Robotic Systems,* 2015.

[107] Q.Meng and M. Lee, "Design issues for assistive robotics for the elderly," *Advanced Engineering Informatics,* vol. 20, no. 2, pp. 171-186, 2006.

[108] CrossFit, "MOVEMENT ABOUT JOINTS, PART 3: THE WRIST," 14 3 2019. [Online]. Available: https://www.crossfit.com/essentials/movement-about-joints-part-3-wrist. [Accessed 16 1 2020].

[109] H. J. team, "Pronation and supination," [Online]. Available: https://healthjade.com/pronation-and-supination/. [Accessed 16 1 2020].

[110] "Military Disability Made Easy," 2013, [Online]. Available: http://www.militarydisabilitymadeeasy.com/thewrist.html. [Accessed 16 1 2020].

[111] N. Hamilton, M. Manisali and I. Gunal, in *Kinesiology: Scientific basis of human motion*, 11 ed., Boston, McGraw-Hill Higher Education, XV, 2008, p. 627.

[112] M. H. Rahman, T. K. Ouimet, M. Saad, J. P. Kenne and P. S. Archambault, "Dynamic and Evaluation of a Robotic Exoskeleton for Upper-Limb Rehabilitation," *International Journal of Information Acquisition,* vol. 8, no. 1, pp. 83-102, 2011.

[113] M. H. Rahman, M. Saad, J. P. Kenne and P. S. Archambault, "Robot assisted rehabilitation for elbow and forearm movements," *Int. J. Biomechatronics and Biomedical Robotics,* vol. 1, no. 4, pp. 206-281, 2011.

[114] "Physical Therapy Standards," Department of Rehabilitation Services, Brigham and Women's Hospital, [Online]. Available: https://www.brighamandwomens.org/patients-and-families/rehabilitation-services/physical-therapy-standards. [Accessed 25 10 2019].

[115] Zion Market Research, "Global Disabled and Elderly Assistive Technology Market Set For Rapid Growth, To Reach Value Around USD 30.82 Billion By 2024," Zion Market Research, August 2018. [Online]. Available: https://www.zionmarketresearch.com/news/disabled-elderly-assistiv. [Accessed 25 February 2019].

[116] "Extremities (Shoulder and Small Joint Implants) Market Analysis, By Product Type (Upper Extremity Devices, Lower Extremity Devices), By Material (Ceramics, Metallic, Polymeric), By End Use (Hospitals, Ambulatory Surgical Centres, Orthopedic Clinics)," Reports and data, May 2019. [Online]. Available: https://www.reportsanddata.com/report-detail/extremities-shoulder-and-small-joint-implants-market. [Accessed 22 August 2019].

[117] Grand View Research, "Rehabilitation Devices/Equipment Market Analysis By Product Type, (Daily Living Aids, Mobility Equipment, Exercise Equipment, Body Support Devices), By Application, By End-use, By Region, And Segment Forecasts, 2018 – 2025," Grand View Research, September 2017. [Online]. Available:

https://www.grandviewresearch.com/industry-analysis/rehabilitation-products-market . [Accessed 15 Fabruary 2019].

[118] Z. AU, R. Islam and M. H. Rahman, "Customer Discovery: Powered Hand Rehab Glove. Vol. $2400. (Milwaukee I-Corps Site: NSF: I Corps #1450386)," Milwaukee, 2018.

[119] H. &. S. Foundation, "Tracking Heart Disease and Stroke in Canada," 2009. [Online]. Available: http://www.heartandstroke.com. [Accessed 14 February 2019].

[120] D. C. A, "Human and economic burden of stroke.," 15 Januaey 2009. [Online]. Available: http://heartandstroke.com. [Accessed 16 February 2019].

[121] D. J. Reinkensmeyer, J. Emken and S. Cramer, "Robotics, motor learning, and neurologic recovery," *Annual Review of Biomedical Engineering*, vol. 6, pp. 497-525, 2004.

[122] N. F. Gordon, M. Gulanick, F. Costa, G. Fletcher and B. A. Franklin, "Physical activity and exercise recommendations for stroke survivors: an American Heart Association scientific statement from the Council on Clinical Cardiology, Subcommittee on Excercise, Cardiac Rehabilitation, and Prevention," *Stroke,* vol. 35, no. 5, pp. 1230-1240, 2004.

[123] F. R. Sarlegna and R. L. Sainburg, "The effect of target modality on visual and proprioceptive contributions to the control of movement distance," *Experimental Brain Research,* vol. 176, no. 2, pp. 267-280, 2007.

[124] J. D. Sanjuan, I. Rulik and T. Ahmed, *Smart Shoulder Rehab,* Milwaukee: NSF: Milwaukee I-Corps Program (#AAH5514), 2019.

[125] L. Sutton, H. Moein, A. Rafiee, J. D. W. Madden and C. Menon, "Design of an assistive wrist orthosis using conductive nylon actuators," in *6th IEEE International Conference on Biomedical Robotics and Biomechatronics (BioRob)*, Singapore, 2016.

[126] N. Omarkulov, K. Telegenov, M. Zeinullin, I. Tursynbek and A. Shintemirov, "Preliminary mechanical design of NU-Wrist: A 3-DOF self-aligning Wrist rehabilitation robot," in *6th IEEE International Conference on Biomedical Robotics and Biomechatronics (BioRob),*, Singapore, 2016.

[127] E. Pezent, C. G. Rose, A. D. Deshpande and M. K. O'Malley, "Design and characterization of the OpenWrist: A robotic wrist exoskeleton for coordinated hand-wrist rehabilitation," in *International Conference on Rehabilitation Robotics (ICORR)*, London, 2017.

[128] A. Pehlivan, S. Fabrizio, E. Andrew, N. Yozbatiran, G. Francisco and M. O'Malley, "Design and validation of the RiceWrist-S exoskeleton for robotic rehabilitation after incomplete spinal cord injury," *Robotica*, 2014.

[129] H. Bian, Z. Chen, H. Wang and T. Zhao, "Mechanical design of EFW Exo II: A hybrid exoskeleton for elbow-forearm-wrist rehabilitation," in *International Conference on Rehabilitation Robotics (ICORR)*, London, 2017.

[130] M. Atlihan, A. Erhan and M. Arslan, "Development of a Therapeutic Exercise Robot for Wrist and Forearm Rehabilitation," in *19th International Conference on Methods and Models in Automation and Robotics*, Poland, 2014.

[131] H. Al-Fahaam, S. Davis and S. Nefti-Meziani, "Wrist rehabilitation exoskeleton robot based on pneumatic soft actuators," in *International Conference for Students on Applied Engineering (ICSAE)*, Newcastle upon Tyne, 2016.

[132] D. Buongiorno, E. Sotgiu, D. Leonardis, S. Marcheschi, M. Solazzi and A. Frisoli, "WRES: A Novel 3 DoF WRist ExoSkeleton With Tendon-Driven Differential Transmission for Neuro-Rehabilitation and Teleoperation," *IEEE Robotics and Automation Letters*, vol. 3, no. 3, pp. 2152-2159, 2018.

[133] Y. Su, Y. Yu and C. Lin, "A compact wrist rehabilitation robot with accurate force/stiffness control and misalignment adaptation," *International Journal of Intelligent Robotics and Applications*, vol. 3, no. 1, pp. 45-58, 2019.

[138] N. Kato, D. Shujiro, T. Akagi, T. Morimoto and Y. Soga, "Development of Wearable Wrist Rehabilitation Device Using Flexible Pneumatic Cylinders," in *MATEC Web of Conferences*, 2016.

[139] D. . A. Winter, "ANTHROPOMETRY," in *Biomechanics and Motor Control of Human Movement*, Newyork, Wiley, 2009, p. 86.

[140] T. Nef and R. Riener, "Shoulder actuation mechanisms for arm rehabilitation exoskeletons," in *2nd IEEE RAS & EMBS International Conference on Biomedical Robotics and Biomechatronics*, 2008.

[141] R. Shadmehr, M. A. Smith and J. W. Krakauer, "Error Correction, Sensory Prediction, and Adaptation in Motor Control," *Annual Review of Neuroscience*, 2010.

APPENDIX – A

Mass and Inertia Properties of iTbot (Link-1)

```
Mass = 1.79031390 kilograms

Volume = 0.00056893 cubic meters

Surface area = 0.23836799 square meters

Center of mass: ( meters )
       X = 0.26851156
       Y = -0.00001008
       Z = -0.00781626

Principal axes of inertia and principal moments of inertia: ( kilograms * square meters )
Taken at the center of mass.
        Ix = ( 0.99997597, 0.00001276, -0.00693282)         Px = 0.00132227
        Iy = (-0.00001560, 0.99999992, -0.00041030)         Py = 0.01658514
        Iz = ( 0.00693281, 0.00041039, 0.99997588)  Pz = 0.01715484

Moments of inertia: ( kilograms * square meters )
Taken at the center of mass and aligned with the output coordinate system.
       Lxx = 0.00132303      Lxy = 0.00000019      Lxz = -0.00010976
       Lyx = 0.00000019      Lyy = 0.01658514      Lyz = -0.00000024
       Lzx = -0.00010976     Lzy = -0.00000024     Lzz = 0.01715408

Moments of inertia: ( kilograms * square meters )
Taken at the output coordinate system.
       Ixx = 0.00143241      Ixy = -0.00000465     Ixz = -0.00386720
       Iyx = -0.00000465     Iyy = 0.14577339      Iyz = -0.00000009
       Izx = -0.00386720     Izy = -0.00000009     Izz = 0.14623294

One or more components have overridden mass properties:
       CSF-17-XXX-2UH.stp<1><Default>
       200142_EC45fl_30W_B<Default>
-----------------------------------------------
```

Mass and Inertia Properties of iTbot (Link-2)

```
Mass = 0.64960702 kilograms

Volume = 0.00033051 cubic meters

Surface area = 0.14786344 square meters

Center of mass: ( meters )
       X = 0.14999885
       Y = 0.00008190
       Z = 0.02330440

Principal axes of inertia and principal moments of inertia: ( kilograms * square meters )
Taken at the center of mass.
        Ix = ( 0.98036257, -0.00036263, 0.19720321)        Px = 0.00091151
        Iy = ( 0.19720279, -0.00095733, -0.98036225)       Py = 0.00584865
        Iz = ( 0.00054430, 0.99999948, -0.00086702)        Pz = 0.00637504

Moments of inertia: ( kilograms * square meters )
Taken at the center of mass and aligned with the output coordinate system.
       Lxx = 0.00110351      Lxy = -0.00000204     Lxz = 0.00095450
       Lyx = -0.00000204     Lyy = 0.00637504      Lyz = 0.00000010
       Lzx = 0.00095450      Lzy = 0.00000010      Lzz = 0.00565665

Moments of inertia: ( kilograms * square meters )
Taken at the output coordinate system.
       Ixx = 0.00145631      Ixy = 0.00000594      Ixz = 0.00322529
       Iyx = 0.00000594      Iyy = 0.02134377      Iyz = 0.00000134
       Izx = 0.00322529      Izy = 0.00000134      Izz = 0.02027258
-----------------------------------------------
```

APPENDIX – B

Motor Specifications, Maxon EC45 30W

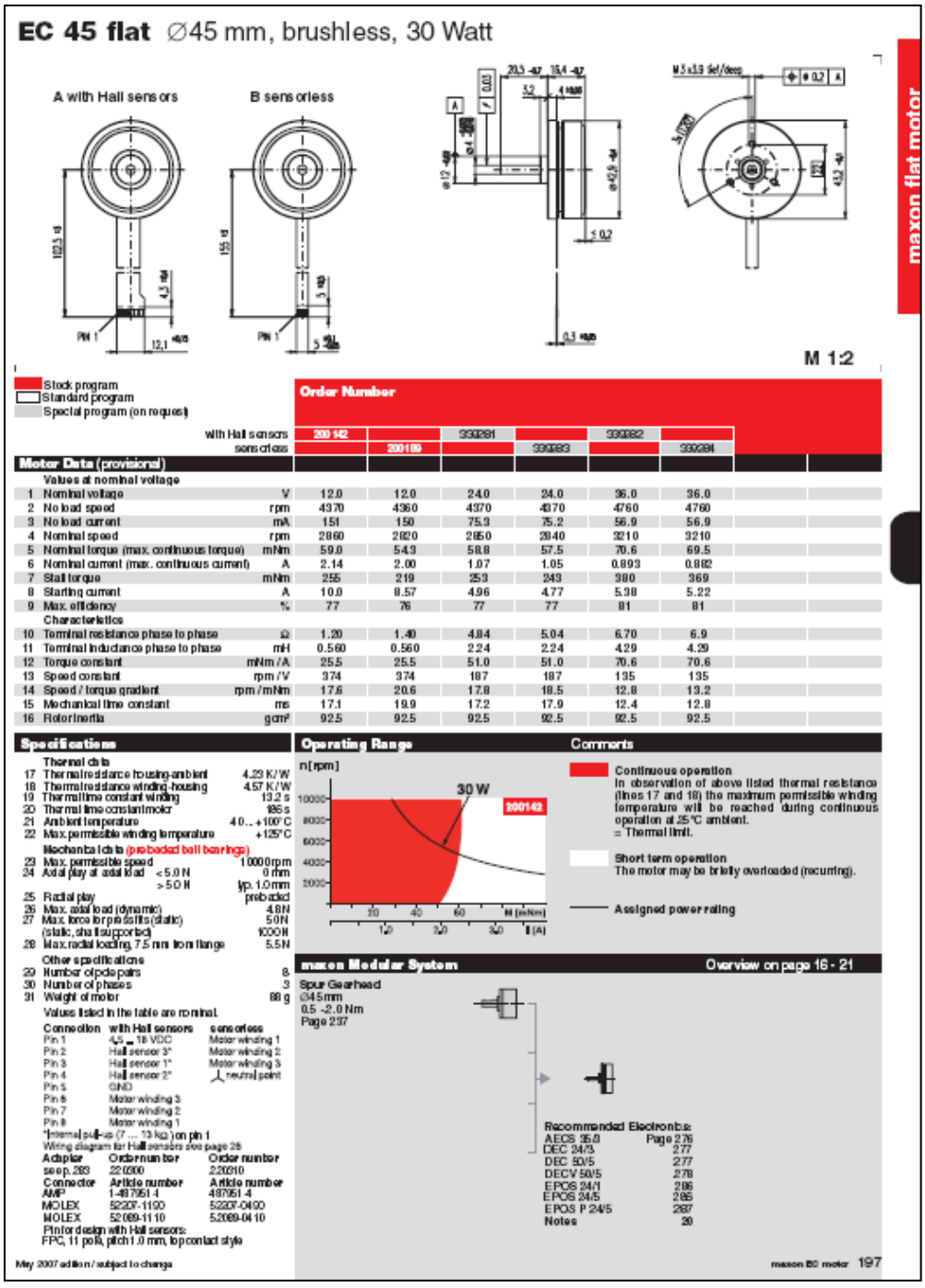

EC 45 flat ∅45 mm, brushless, 30 Watt

maxon flat motor

A with Hall sensors

B sensorless

M 1:2

Stock program
Standard program
Special program (on request)

			Order Number							
		with Hall sensors	200142		339281		339282			
		sensorless		200189		339283		339284		
	Motor Data (provisional)									
	Values at nominal voltage									
1	Nominal voltage	V	12.0	12.0	24.0	24.0	36.0	36.0		
2	No load speed	rpm	4370	4360	4370	4370	4760	4760		
3	No load current	mA	151	150	75.3	75.2	56.9	56.9		
4	Nominal speed	rpm	2860	2820	2850	2840	3210	3210		
5	Nominal torque (max. continuous torque)	mNm	59.0	54.3	58.8	57.5	70.6	69.5		
6	Nominal current (max. continuous current)	A	2.14	2.00	1.07	1.05	0.893	0.882		
7	Stall torque	mNm	255	219	253	243	380	369		
8	Starting current	A	10.0	8.57	4.96	4.77	5.38	5.22		
9	Max. efficiency	%	77	76	77	77	81	81		
	Characteristics									
10	Terminal resistance phase to phase	Ω	1.20	1.40	4.84	5.04	6.70	6.9		
11	Terminal inductance phase to phase	mH	0.560	0.560	2.24	2.24	4.29	4.29		
12	Torque constant	mNm / A	25.5	25.5	51.0	51.0	70.6	70.6		
13	Speed constant	rpm / V	374	374	187	187	135	135		
14	Speed / torque gradient	rpm / mNm	17.6	20.6	17.8	18.5	12.8	13.2		
15	Mechanical time constant	ms	17.1	19.9	17.2	17.9	12.4	12.8		
16	Rotor inertia	gcm²	92.5	92.5	92.5	92.5	92.5	92.5		

Specifications

Thermal data

17	Thermal resistance housing-ambient	4.23 K / W
18	Thermal resistance winding-housing	4.57 K / W
19	Thermal time constant winding	13.2 s
20	Thermal time constant motor	185 s
21	Ambient temperature	-40...+100°C
22	Max. permissible winding temperature	+125°C

Mechanical data (prebacked ball bearings)

23	Max. permissible speed	10000 rpm
24	Axial play at axial load < 5.0 N	0 mm
	> 5.0 N	typ. 1.0 mm
		prebacked
25	Radial play	4.8 N
26	Max. axial load (dynamic)	5.0 N
27	Max. force for press fits (static)	1000 N
	(static, shaft supported)	5.5 N
28	Max. radial loading, 7.5 mm from flange	

Other specifications

29	Number of pole pairs	8
30	Number of phases	3
31	Weight of motor	88 g

Values listed in the table are nominal.

Connection	with Hall sensors	sensorless
Pin 1	4.5 ... 18 VDC	Motor winding 1
Pin 2	Hall sensor 3*	Motor winding 2
Pin 3	Hall sensor 1*	Motor winding 3
Pin 4	Hall sensor 2*	neutral point
Pin 5	GND	
Pin 6	Motor winding 3	
Pin 7	Motor winding 2	
Pin 8	Motor winding 1	

*Internal pull-up (7 ... 13 kΩ) on pin 1

Wiring diagram for Hall sensors see page 25

Adapter	Order number	Order number
see p. 283	220300	220310
Connector	Article number	Article number
AMP	1-487951-4	487951-4
MOLEX	52207-1190	52207-0490
MOLEX	52089-1110	52089-0410

Pin for design with Hall sensors:
FPC, 11 pole, pitch 1.0 mm, top contact style

Operating Range

Comments

Continuous operation
In observation of above listed thermal resistance (lines 17 and 18) the maximum permissible winding temperature will be reached during continuous operation at 25°C ambient.
= Thermal limit.

Short term operation
The motor may be briefly overloaded (recurring).

Assigned power rating

maxon Modular System Overview on page 16 - 21

Spur Gearhead
∅45 mm
0.5 -2.0 Nm
Page 237

Recommended Electronics:

AECS 35/8	Page 276
DEC 24/3	277
DEC 50/5	277
DECV 50/5	278
EPOS 24/1	286
EPOS 24/5	285
EPOS P 24/5	287
Notes	20

May 2007 edition / subject to change

maxon EC motor 197

maxon flat motor

EC 45 flat ∅42.8 mm, brushless, 70 Watt

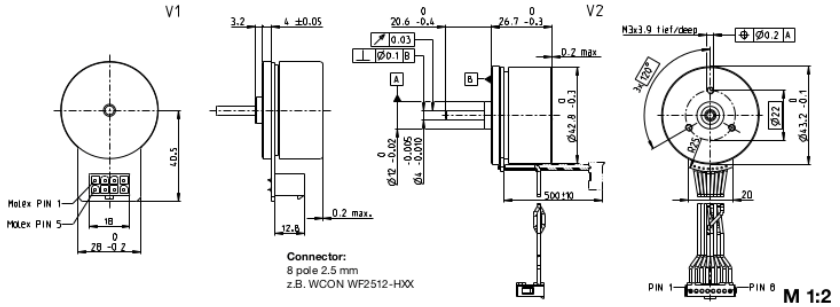

Connector:
8 pole 2.5 mm
z.B. WCON WF2512-HXX

Stock program
Standard program
Special program (on request)

	Part Numbers			
V1 with Hall sensors	397172	402685	402686	402687
V2 with Hall sensors and cables	411812	411814	411815	411816

Motor Data (provisional)						
Values at nominal voltage						
1 Nominal voltage	V	24	30	36	48	
2 No load speed	rpm	6110	6230	6330	3440	
3 No load current	mA	234	194	166	48.1	
4 Nominal speed	rpm	4860	4990	5080	2540	
5 Nominal torque (max. continuous torque)	mNm	128	112	108	134	
6 Nominal current (max. continuous current)	A	3.21	2.36	1.93	0.936	
7 Stall torque[1]	mNm	1460	1170	1100	915	
8 Stall current	A	39.5	25.8	20.7	6.97	
9 Max. efficiency	%	85	84	83	84	
Characteristics						
10 Terminal resistance phase to phase	Ω	0.608	1.16	1.74	6.89	
11 Terminal inductance phase to phase	mH	0.463	0.691	0.966	5.85	
12 Torque constant	mNm / A	36.9	45.1	53.3	131	
13 Speed constant	rpm / V	259	212	179	72.7	
14 Speed / torque gradient	rpm / mNm	4.26	5.44	5.85	3.82	
15 Mechanical time constant	ms	8.07	10.3	11.1	7.24	
16 Rotor inertia	gcm²	181	181	181	181	

Specifications

Thermal data

17	Thermal resistance housing-ambient	3.56 K/W
18	Thermal resistance winding-housing	4.1 K/W
19	Thermal time constant winding	29.6 s
20	Thermal time constant motor	178 s
21	Ambient temperature	-40 ... +100°C
22	Max. winding temperature	+125°C

Mechanical data (preloaded ball bearings)

23	Max. speed	10 000 rpm
24	Axial play at axial load < 4.0 N	0 mm
	> 4.0 N	0.14 mm
25	Radial play	preloaded
26	Max. axial load (dynamic)	3.8 N
27	Max. force for press fits (static)	50 N
	(static, shaft supported)	1000 N
28	Max. radial load, 5 mm from flange	21 N

Other specifications

29	Number of pole pairs	8
30	Number of phases	3
31	Weight of motor	141 g

Values listed in the table are nominal.

Connection	**V1**	**V2** (AWG 24)
Pin 1	Hall sensor 1*	Motor winding 1
Pin 2	Hall sensor 2*	Motor winding 2
Pin 3	V_{Hall} 4.5 ... 18 VDC	Motor winding 3
Pin 4	Motor winding 3	V_{Hall} 4.5 ... 18 VDC
Pin 5	Hall sensor 3*	GND
Pin 6	GND	Hall sensor 1*
Pin 7	Motor winding 1	Hall sensor 2*
Pin 8	Motor winding 2	Hall sensor 3*

*Internal pull-up (7 ... 13 kΩ) on V_{Hall}
Wiring diagram for Hall sensors see p. 47

Cable for V1

Connection cable Universal, L = 500 mm	**339380**
Connection cable to EPOS, L = 500 mm	**354045**

V2

21	Ambient temperature	-20 ... +100°C

[1]Calculation does not include saturation effect (p. 57/162)

Operating Range Comments

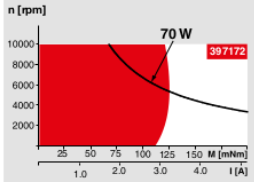

Continuous operation
In observation of above listed thermal resistance (lines 17 and 18) the maximum permissible winding temperature will be reached during continuous operation at 25°C ambient.
= Thermal limit.

Short term operation
The motor may be briefly overloaded (recurring).

Assigned power rating

maxon Modular System Details on catalog page 36

Planetary Gearhead
∅42 mm
3 - 15 Nm
Page 363

Spur Gearhead
∅45 mm
0.5 - 2.0 Nm
Page 365

Encoder MILE
256 - 2048 CPT,
2 channels
Page 412

Recommended Electronics:

Notes	Page **36**
ESCON 36/3 EC	455
ESCON Mod. 50/4 EC-S	455
ESCON Module 50/5	455
ESCON 50/5	457
DEC Module 50/5	459
EPOS4 50/5	463
EPOS4 Mod./Comp. 50/5	463
EPOS2 P 24/5	470
MAXPOS 50/5	473

April 2019 edition / subject to change

APPENDIX – C

Harmonic Drive Specifications, CSF-17-100-2UH

Rating table

■ CSF Series

Table 127-1

Size	Ratio	Rated Torque at 2000rpm		Limit for Repeated Peak Torque		Limit for Average Torque		Limit for Momentary Peak Torque		Maximum Input Speed (rpm)		Limit for Average Input Speed (rpm)		Moment of Inertia	
		Nm	kgfm	Nm	kgfm	Nm	kgfm	Nm	kgfm	Oil lubricant	Grease lubricant	Oil lubricant	Grease lubricant	I ×10⁻⁴kgm²	J ×10⁻³kgfms²
14	30	4.0	0.41	9.0	0.92	6.8	0.69	17	1.7	14000	8500	6500	3500	0.033	0.034
	50	5.4	0.55	18	1.8	6.9	0.70	35	3.6						
	80	7.8	0.80	23	2.4	11	1.1	47	4.8						
	100	7.8	0.80	28	2.9	11	1.1	54	5.5						
17	30	8.8	0.90	16	1.6	12	1.2	30	3.1	10000	7300	6500	3500	0.079	0.081
	50	16	1.6	34	3.5	26	2.6	70	7.1						
	80	22	2.2	43	4.4	27	2.7	87	8.9						
	100	24	2.4	54	5.5	39	4.0	108	11						
	120	24	2.4	54	5.5	39	4.0	86	8.8						
20	30	15	1.5	27	2.8	20	2.0	50	5.1	10000	6500	6500	3500	0.193	0.197
	50	25	2.5	56	5.7	34	3.5	98	10						
	80	34	3.5	74	7.5	47	4.8	127	13						
	100	40	4.1	82	8.4	49	5.0	147	15						
	120	40	4.1	87	8.9	49	5.0	147	15						
	160	40	4.1	92	9.4	49	5.0	147	15						

Harmonic Drive CSF-17-100-2UH series output bearing specification

■ Output bearing specifications

The specifications of the cross roller are shown in Table 136-1.

Specifications CSG Series/CSF Series

Table 136-1

Size	Pitch circle dia. of a roller	Offset	Basic rated load				Allowable moment load		Moment stiffness	
	dp	R	Basic dynamic rated load C		Basic static rated load Co		Mc		×10⁴ Nm/rad	kgfm/arc min
	m	m	×10³N	kgf	×10³N	kgf	Nm	kgfm		
14	0.035	0.0095	47	480	60.7	620	41	4.2	4.38	1.3
17	0.0425	0.0095	52.9	540	75.5	770	64	6.5	7.75	2.3
20	0.050	0.0095	57.8	590	90.0	920	91	9.3	12.8	3.8
25	0.062	0.0115	96.0	980	151	1540	156	16	24.2	7.2
32	0.080	0.013	150	1530	250	2550	313	32	53.9	16
40	0.096	0.0145	213	2170	365	3720	450	46	91.0	27
45	0.111	0.0155	230	2350	426	4340	686	70	141	42
50	0.119	0.018	348	3550	602	6140	759	77	171	51
58	0.141	0.0205	518	5290	904	9230	1180	120	283	84
65	0.160	0.0225	556	5670	1030	10500	1860	190	404	120

APPENDIX – D

Force/Torque Sensor Specifications, RFT60-HA01

SENSOR SPECIFICATIONS

Sensor Figure	Dimension		Weight	Data Rate	Load Capacity			Resolution		
	ø	H	Except Cable	Maximum	Fx, Fy	Fz	Tx, Ty, Tz	Fx, Fy	Fz	Tx, Ty, Tz
	mm	mm	g	Hz	N	N	Nm	mN	mN	mNm
RFT40-SA01	40	18.5	60	200	100	150	2.5	200	200	8
RFT44-SB01	44	20	70	200	100	150	2.5	200	200	8
RFT60-HA01	60	18.5	120	1,000	150	200	4	100	150	5
RFT64-SB01	64	20	140	1,000	150	200	4	100	150	5
RFT76-HA01	76	18.5	200	1,000	300	300	10	200	200	8
RFT82-HA02	82	23	260	1,000	400	400	20	250	250	10
RFT80-6A01	80	22	210	1,000	400	400	20	100	100	5

Resolution : The standard deviation of each six components of force and torque for 10second, the data through internal 1st-order low pass filter which has cutoff frequency 100Hz

Sensor Figure	Dimension		Hysteresis			Overload Capacity				Cross Talk		
	ø	H	Fx, Fy	Fz	Tx, Ty, Tz	Fx, Fy	Fz+	Fz-	Tx, Ty, Tz	Fx, Fy	Fz	Tx, Ty, Tz
	mm	mm	%FS			%				%FS		
RFT40-SA01	40	18.5	2	0.5	1	150	150	300	150	3	3	3
RFT44-SB01	44	20	2.5	1	3	150	150	300	150	3	3	3
RFT60-HA01	60	18.5	2.5	1	1	150	150	300	150	3	3	3
RFT64-SB01	64	20	3	2	2	150	150	300	150	3	3	3
RFT76-HA01	76	18.5	2.5	1	1	150	150	300	150	3	3	3
RFT82-HA02	82	23	2.5	1	1	150	200	400	200	3	3	3
RFT80-6A01	80	22	2.5	1	1	150	200	400	200	3	3	3

Fz+ : Tensile force, Fz- : Compressive force . The capacity of compressive force is more capacity than the capacity of tensile force